摘　要

进行高能重离子对撞实验的目的之一就是来研究核核碰撞中产生的热密核物质的相结构。这个相结构可以由量子色动力学 (QCD) 相图来表示，其中横坐标是热力学温度 (T)，纵坐标是重子化学势 (μ_B)。格点 QCD 的计算表明在高重子化学势和低温情况下，核物质从强子相到夸克饺子等离子相的转变是一个一阶相变。而在低重子化学势和高温区域，这个转变是一个平滑的穿越。那么在这个一阶相变边界和平滑穿越区之间必然有一个终点，这个点被称作 QCD 临界点。实验室上对于临界点的寻找是一个非常重要的课题，位于美国布鲁克海文国家实验室 (BNL) 的相对论重离子对撞机 (RHIC) 上提出的能量扫描计划 (BES) 的核心任务之一就是寻找 QCD 临界点。

守恒量的涨落，比如净重子数 (B)，净电荷数 (Q)，和净奇异数 (S)，被认为同 QCD 相变和 QCD 临界点非常的敏感。实验上，我们可以通过重离子对撞逐事件地测量各种末态粒子多重数的各阶矩 (方差 (σ^2)，偏度 (S)，峰度 (κ))。这些矩与对撞中产生的热密物质系统的关联长度非常敏感，同时它们也与格点 QCD 和强子共振气体模型中计算的热力学磁化率有着关联。

比如，这些守恒量的涨落的方差，偏度，和峰度已经被证明同系统的各阶关联长度 $\xi^2, \xi^{4.5}$ 和 ξ^7 成正比。同时，系统的 n 阶磁化率同守恒量 (B, Q, S) 涨落的各阶累积量有着直接的关系，$\chi^{(n)} = C_n/VT^3$。其中 V, T 是碰撞系统的体积和温度，C_n 是多重数分布的 n 阶累积量。实验上，碰撞系统的体积非常难以确定, 为了同理论计算结果做比较，我们取各阶累积量的比值 ($S\sigma = C_3/C_2, \kappa\sigma^2 = C_4/C_2$) 来消除系统体积的影响。因此这些累积量的比值可以直接同理论计算的各阶磁化率的比值联系起来，$\kappa\sigma^2$=$\chi_B^{(4)}/\chi_B^{(2)}$ 和 $S\sigma$=$\chi_B^{(3)}\chi_B^{(2)}$. 由于同关联长度和热力学磁化率有着非常高的敏感度，我们可以用守恒量分布的各阶矩来研究 QCD 相变和寻找 QCD 临界点。而实验上，获取净重子数 (ΔN_B) 和净奇异子数 (ΔN_S) 的分布非常难以实现，所以我们分别用净质子数 (ΔN_P) 和净 K 介子数 (ΔN_K) 的分布来代替。这已经在理论上和实验上被广泛的研究。RHIC 上的能量扫描计划开始于 2010 年，分别于 2010 年，2011 年，和 2014 年期间采集了碰撞能量从 7.7GeV 到 200GeV 之间的金金碰撞的 8 个能量点，与之相对应的重子化学势的范围从 20MeV 到 420MeV。

在这篇论文中，我研究了在金金碰撞中 STAR 探测器上净 K 介子多重数分布的各阶累积量以及他们的比值。碰撞能量包含 8 个能量点，$\sqrt{s_{NN}}$= 7.7, 11.5, 14.5, 19.6, 27, 39, 62.4, and 200 GeV。我们重点讨论了 K 介子多重数的的各阶累积量以及他们的比值的中心度依赖和能量依赖。这些结果同我们的基线计算 (泊松和

负二项式基线) 和 UrQMD 模型的计算结果也做了比较。从累积量比值的中心度依赖结果中我们可以看出，σ^2/M 的值是随着能量的增大而增大，而且边缘碰撞的结果要比中心碰撞的结果更大。对于 $\kappa\sigma^2$ 和 $S\sigma$ 的最中心碰撞的能量依赖，由于实验的误差较大，在误差范围内他们的结果是同我们的基线计算 (泊松和负二项式基线) 和 UrQMD 计算相吻合。对于边缘碰撞，泊松期望和负二项式期望的值都在实验测量值之下。对于 σ^2/M, $S\sigma$, 和 $\kappa\sigma^2$ 的值，在误差允许的范围内，除了 200GeV 的 σ^2/M 值，UrQMD 的计算结果是同实验测量的值是一致的。

这篇论文按如下结构组织。在第一章中，我们对这个分析的背景和目的作了简明扼要的介绍。第二章中，我们对 RHIC 上 STAR 探测器的结构和分析中所需要用到的子探测器给予一个大概了解。然后，我将在第三章中介绍净 K 介子多重数分布高阶矩分析所用到的方法和分析细节，从数据准备，粒子鉴别，到误差分析，修正方法等方面给出详细介绍，最后给出结果。在第四章中，我们主要研究了在超相对论量子分子动力学模型 (UrQMD) 中净质子多重数，净电荷多重数，和净 K 介子多重数分布的各阶累积量及其比值的中心度和能量依赖，并与 STAR 实验组发表的结果作了比较。第五章中，主要对事件平面探测器作一个简单介绍，它将在 BESII 中起到事件平面重建，中心度划分，和 trigger 的作用。最后一章中我们将对全文作一个概括以及对未来的一个展望。

Abstract

The main goals of the high energy nuclear collisions are to explore the phase structure of strongly interacting hot and dense nuclear matter and map the quantum chromodynamics (QCD) phase diagram which can be displayed by the temperature (T) and baryon chemical potential (μ_B)). The calculations from Lattice QCD suggest that the phase transition between the hadronic phase and Quark-Gluon Plasma (QGP) phase at large μ_B and low T is of first order. While at low μ_B and high T region, the phase transition is a smooth crossover. The point at the end of first order phase boundary towards crossover region is called QCD Critical Point (CP). Experimental discovery of the critical point is one of the central targets of the Beam Energy Scan (BES) program at the Relativistic Heavy-Ion Collider (RHIC) facility.

Fluctuations of conserved quantities, such as net-baryon (B), net-charge (Q) and net-strangeness (S), have been predicted to be sensitive to the QCD phase transition and QCD critical point. Experimentally, one can measure various order moments (Variance(σ^2), Skewness(S), Kurtosis(κ)) of the event-by-event conserved quantities distributions in heavy-ion collisions. These moments are sensitive to the correlation length (ξ) of the hot dense matter created in the heavy-ion collisions and also connected to the thermodynamic susceptibilities computed in Lattice QCD and in the Hadron Resonance Gas (HRG) model.

For instance, the variance, skewness and kurtosis have been shown to be related to the different power of the correlation length as ξ^2, $\xi^{4.5}$ and ξ^7, respectively. Theoretically, the n^{th} order susceptibilities $\chi^{(n)}$ are related to cumulant as $\chi^{(n)} = C_n/VT^3$, where V, T are the volume and temperature of the system, C_n is the n^{th} order cumulants of multiplicity distributions. In order to compare with the theoretical calculations, cumulant ratios ($S\sigma = C_3/C_2, \kappa\sigma^2 = C_4/C_2$) are constructed to cancel the volume effects. Thus, those moment products are also directly related to the ratios of various order susceptibilities as $\kappa\sigma^2$=$\chi_B^{(4)}/\chi_B^{(2)}$ and $S\sigma$=$\chi_B^{(3)}/\chi_B^{(2)}$. Due to the high sensitivity to the correlation length and the connection with the susceptibilities, one can use the moments of the conserved quantity distributions to search for the QCD critical point and the QCD phase transition. Experimentally, it is very hard to measure the net-baryon (ΔN_B) and the net-strangeness (ΔN_S) distributions, so we use net-proton (ΔN_P) and net-kaon (ΔN_K) as proxies respectively. These have been widely studied experimentally and theoretically. The first phase

of the beam energy scan program has started in the year 2010 at RHIC. It tunes the Au+Au colliding energies from 200 GeV down to 7.7 GeV, which correspond to a baryon chemical potentials range from 20 to 420 MeV.

In this thesis, we performed the first measurements by the STAR experiment for the high moments of net-kaon multiplicity distributions in Au+Au collisions at $\sqrt{s_{NN}}$ = 7.7, 11.5, 14.5, 19.6, 27, 39, 62.4, and 200 GeV.

From the energy dependence of cumulant ratios, one can see that the values of σ^2/M increase as the collision energy increases, and are larger for peripheral collisions compared with the central collisions. Within uncertainties, the values of $S\sigma$ and $\kappa\sigma^2$ are consistent with both the Poisson and NBD baselines in central collisions. For peripheral collisions, both the Poisson and NBD baselines underestimate the measured $S\sigma$ values. The UrQMD calculations for σ^2/M, $S\sigma$, and $\kappa\sigma^2$ are consistent with the measured values within uncertainties except for σ^2/M at $\sqrt{s_{\rm NN}}$ = 200 GeV.

The manuscript is organized as follows. In the chapter I, I give the brief introduction about the analysis background and the analysis motivation. In the chapter II, I show the basic structure of the STAR detector and the sub-detector which will be used in my analysis. Next, in the chapter III, I will explain the analysis method and analysis details used in the moments calculation of net kaon multiplicity distributions, including the data preparation, particle identification, error estimation, and the correction methods. I will also give the analysis results in this chapter. In the chapter IIII, we calculate the various order of cumulants and their ratios of net proton, net kaon, and net charge multiplicity distributions with UrQMD model. In chapter V, I give the overview of the Event Plane Detector, which will be installed for Beam Energy Scan phase II program. It will provide the reconstruction of event plane, centrality determination, and the trigger. Finally, I will give the summary of this thesis at chapter VI.

Keywords: phase transition, critical point, cumulant, moment products, RHIC-STAR.

Contents

List of Figures

List of Tables

Chapter 1

Introduction

1.1 Quantum Chromodynamics

In nature, there are four widely accepted fundamental interactions—gravitational, electromagnetic, strong nuclear, and weak nuclear. Each one is described mathematically as a field. Among these four interactions, the strong interaction is the mechanism responsible for the strong nuclear force which describes the interaction between the nucleus and quarks. It resists the strong electromagnetic repulsion force between the protons and keep the nucleus stable. At the same time, it also confine the quarks together to form the protons, neutrons, and other hadrons. Quantum Chromodynamics (QCD)[1, 2] is the theory of strong interaction. Similar to Quantum Electrodynamics (QED)[3], quarks carry 'color' charges in QCD theory and the interactions between quarks are mediated by a gauge boson called gluon. However contrary to the properties of photon, the force carrier in QED, gluons take on different color charges as well and can interact among themselves. This gives rise to the rich phenomena in strong interactions. Quantum Chromodynamics (QCD) predicts that quarks and gluons can exist in unconfined state, called the Quark Gluon Plasma (QGP). The QGP is a plasma in which quarks and gluons can move in an extended volume without being restricted to the hadron size. Free quarks or gluons carrying apparent color charges have never been observed because of the confinement nature of strong interactions. Relativistic heavy ion collisions are proposed to create and study such a QGP state in the laboratory[4].

1.1.1 Confinement and Asymptotic freedom

Colored charged particles like quarks and gluons cannot be observed directly. They are always confined within hadrons and this phenomena is known as the

confinement or the color confinement[5]. This does not come from QCD but is an additional constraint on the theory based on the experimental observation that only color singlet states are observed. One way to understand confinement is to examine the behaviour of QCD coupling constant as a function of as a function of energy scale μ,

$$\alpha_s(\mu) = \frac{g_s^2(\mu)}{4\pi} \approx \frac{4\pi}{\beta_0 ln(\mu^2/\Lambda_{QCD}^2)} \tag{1.1}$$

If a pair of quarks are separated away from each other, the interaction will become stronger with increasing distance. Potential energy between the quark pair will also increase, and at some point, the potential energy is large enough to create a new pair of quarks.

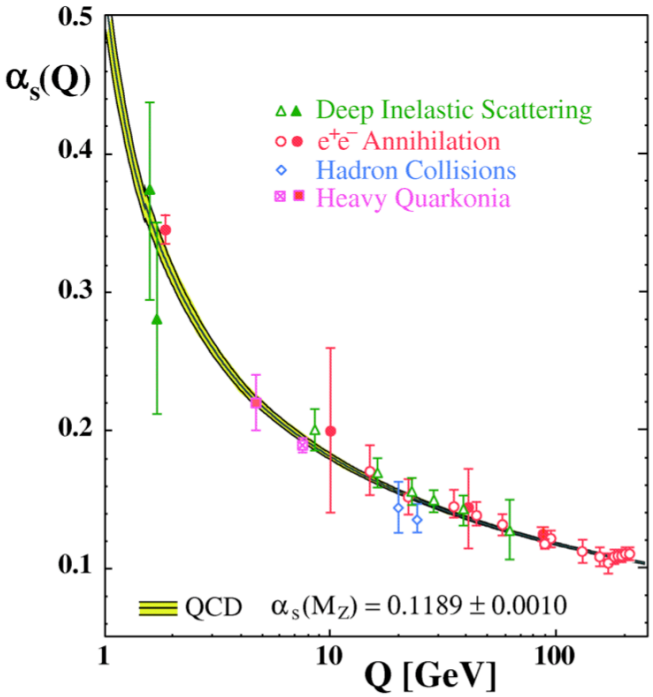

Figure 1.1: (Color online) A summary of coupling constant measurement from different experiments and theoretical calculations as a function of the energy scale Q. Figure taken from[6].

In Figure 1.1 the running coupling constant is shown as a function of the energy scale measured from different experiments. Both the theoretical and experimental

results shows asymptotic variation with the energy. For larger Q value $\alpha_s(Q)$ decreases asymptotically to zero. In this condition the coupling strength between the quarks and gluon becomes negligible and they becomes free asymptotically. This phenomena is known as the Asymptotic Freedom. This is one of the revolutionary discovery in science for which Frank Wilczek, David Gross[7] and David Politzer[8] were honored with the Nobel prize in 2004.

1.1.2 QCD Phase Diagram and Critical Point

Confinement and chiral symmetry breaking are two of the most important features of quantum chromodynamics (QCD). At high temperatures and densities, quark deconfinement occurs and hadronic matter undergoes a phase transition into a new state of matter, the quark-gluon plasma (QGP). The very first QCD phase diagram was proposed by N. Cabibbo and G. Parisi in 1975[9]. It shows in a diagram of baryonic density-temperature phases of quark matter: they have conjectured that there is a phase where quarks are confined and another phase where they are unconfined. Figure 1.2 shows the the first proposed phase diagram between baryon density (ρ_B) as a function of temperature (T). The diagram shows a boundary between the two phases of quark confinement and de-confinement.

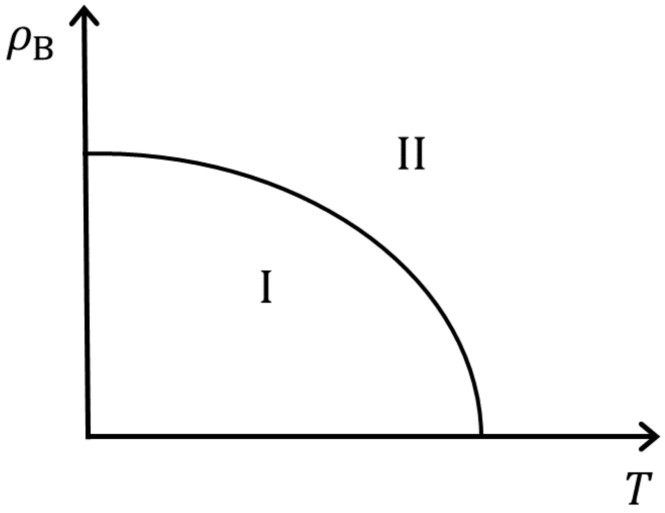

Figure 1.2: (Color online) Schematic phase diagram of hadronic matter. ρ_B is the density of baryonic number. Quarks are confined in phase I and unconfined in phase II. Figure taken from [9].

To understand the QCD phase diagram the quark masses are the most important parameters which are also called as the symmetry breaking parameters as they break the Chiral symmetry. In conjunction with the Chiral symmetry argument, Pisarski-Wilczek [10] predicted that the transition between the confined and deconfined quarks is first order at higher chemical potential (μ_B) region and at lower μ_B region its second order. The point in the first order transition line from where the second order begins is the tricritical point. The second order criticality requires that the quark masses be set to zero. It also concludes that the nuclear matter is at lower temperature region where chiral symmetry is broken [38]. Also the lattice calculation shows that at $\mu_B = 0$ the transition is a cross over[11].

Presently, even if the QCD phase diagram of quark matter is not well known, either experimentally or theoretically, based on available theoretical (lattice and model calculations) and phenomenological inputs, the overview of the structure of the QCD phase diagram can be drawn and it proves to be quite complex. In the following diagram some of the possible phases in which quarks occur are indicated. But many more have been proposed. Figure 1.3 shows a QCD phase diagram with temperature (T) as a function of baryon chemical potential (μ_B). In this figure the solid line is the first order transition line which separate the hadronic phase and the quark-gluon plasma phase. The end point of the first order transition line is the Critical Point (CP) of the second order. At negligible μ_B the transition between these two phase is a cross-over. With low temperature and very high baryon density the state of QGP matter is like Neutron stars which is a very high dense baryon plasma state.

Lattice calculation on finite size and vanishing chemical potential observe that the thermodynamic susceptibilities are very sensitive near the critical region[12, 13]. These thermodynamic susceptibilities are related with the higher moments of conserved quantities like net-baryon, net-strangeness and net-charges. In Figure 1.4 shows the fourth and sixth order susceptibilities calculated from lattice at vanishing chemical potential. The quadratic and quartic susceptibilities for net-baryon, net-strangeness and net-charges shows a rapid rise and a peak respectively at zero chemical potential in the transition region[12]. In the same study it is shown that the sixth order susceptibility of net-strangeness and net- charges changes sign near this transition region. It is also observed that after this transition region all susceptibilities match with the Stefan-Boltzmann limit of massless quarks. The ratio

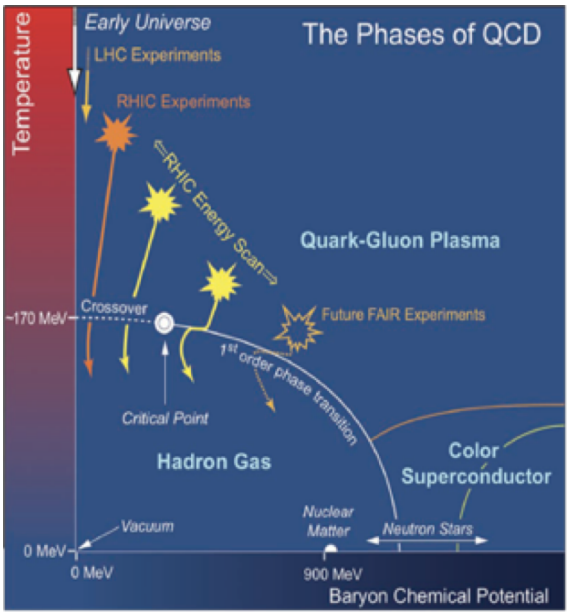

Figure 1.3: (Color online) QCD phase diagram in terms of temperature (T) as a function of baryon chemical potential (μ_B).

of the quartic and quadratic susceptibilities for net-strangeness are shown in the Figure 1.5 and compared with the HRG prediction. It is observed that the ratio have a peak at the transition temperature and falls down to the Stefan-Boltzmann limit after the transition temperature[12].

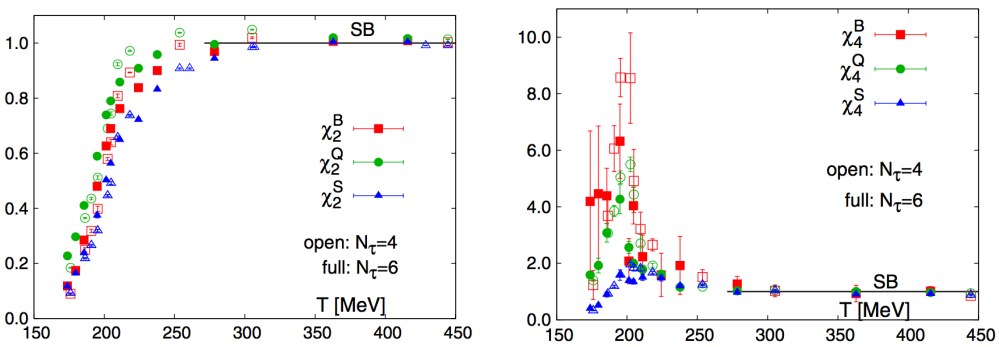

Figure 1.4: Quadratic and quartic fluctuations of baryon number, electric charge, and strangeness. Figure taken from[12]

From the experimental point of view, the location of the CEP is a major goal of several heavy ion collisions programs. At RHIC, the Beam Energy Scan (BES-I) program, ongoing since 2010, is looking for the experimental signatures of the first-order phase transition and the CEP by colliding Au ions at several energies.

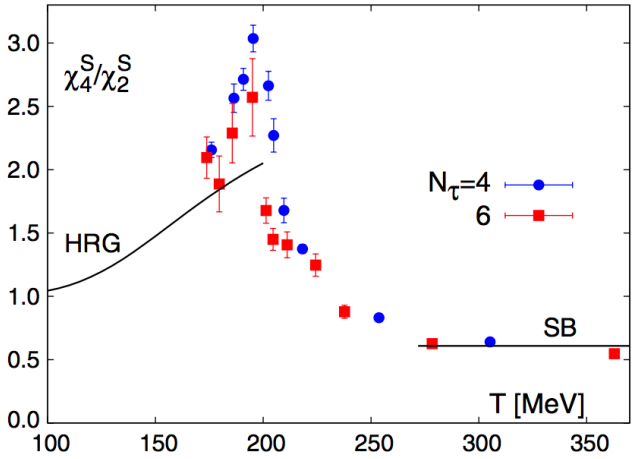

Figure 1.5: The ratio of 4th and 2nd order cumulants of strangeness fluctuations. Figure taken from[12]

Also STAR Collaboration presented their measurements on observables relevant to clarify the existence of the CEP. However, so far no definitive conclusions were possible.

1.2 Heavy Ion Collisions

Relativistic heavy-ion experiments have been carried out to create the extreme conditions in the laboratory to understand similar condition that existed in the early universe. By accelerating two heavy nuclei to ultra-relativistic speeds and then colliding them, such extreme conditions can be created inside a laboratory to look for a formation of the QGP state. It can also be used as a tool to investigate the internal structure of the nuclei at both hadronic (baryons and mesons) and partonic (quarks and gluons) levels. Relativistic heavy ion collider (RHIC) built in Brookhaven National Laboratory is the first accelerator-collider dedicated to heavy ion collisions. Just after the first a few years of operation, a strongly coupled QGP has been found in high energy Au + Au collisions.

In a relativistic heavy ion collision where the QGP is formed, the system evolves through several space-time stages as depicted in Figure 1.6 The inelastic nucleon-nucleon collision happens through parton-parton (quark or gluon) scattering. The QGP is formed within 1fm/c after the collision. The system begins to thermalize by further partonic scattering. As the scattering continues, the system expands in

both longitudinal and transverse directions. The temperature decreases as the system expands. The photons and leptons radiated from the color QGP medium leave the system without further (strong) interactions in the QGP. When the temperature drops below the phase-transition critical value, the system starts to convert back into a hadronic state, in the form of baryons and mesons. The hadronization happens at ∼10 fm/c. After hadronization, the system enters the hadron gas state. In the hadron gas state, hadronic inelastic scatterings change the particle species at the level of hadrons instead of partons. When further hadronic inelastic scattering ceases, particle species is frozen. As the system further expands, the average distance between particles increases. Particle elastic scatterings continue until their distance is too large. Finally, the elastic scattering ceases and particles stream freely into the detector and are recorded. The experimental observables are the charge, momentum and energy of each final state particle reconstructed with the detectors. The final state particles carry the information about the QGP as well as the various stages of evolution.

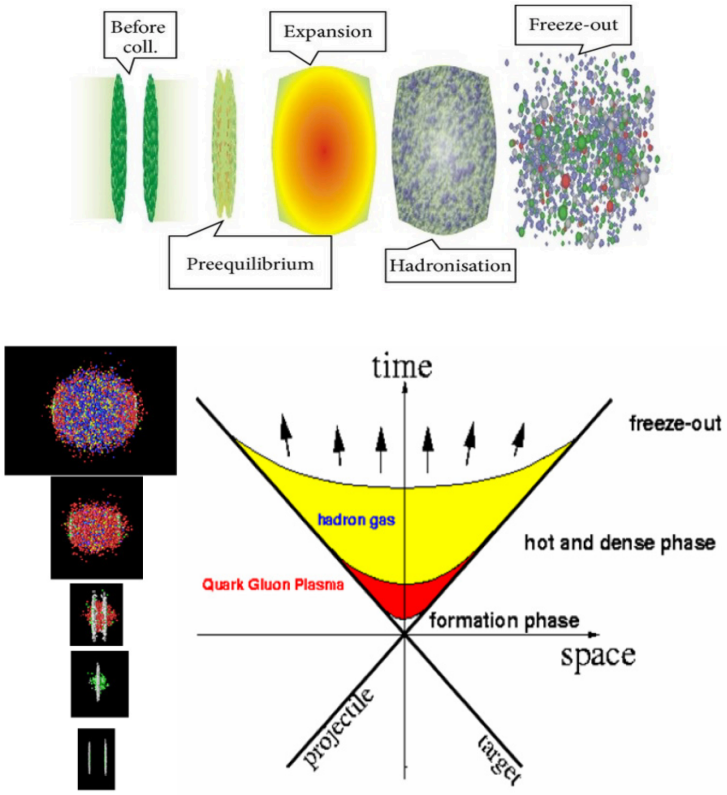

Figure 1.6: Schematic view of the QGP space-time evolution.

The primary goal of the high energy heavy ion collision program is to create the deconfined QGP and to investigate the QGP's properties, such as the temperature and order of the phase transition, the equation of state, and the transport properties.

1.3 Motivation of the Study

1.3.1 Higher Order Moments and Cumulants

In statistics[14], the distribution function can be characterized by the various moments, such as mean (M), variance (σ^2), skewness (S), kurtosis (κ). Before introducing the above moments used in our analysis, we would like to define cumulants, which are alternative approach compared to moments to characterize a distribution.

For a probability distribution, cumulants are defined as:

$$C_n = g^{(n)}(0) = \frac{\partial^n}{\partial t^n} g(t)|_{t=0} \tag{1.2}$$

where $g(t)$ is the cumulant generating function and the cumulants C_n are the coefficients of Taylor expansion of $g(t)$, about the centre. For a random variable X, $g(t)$ is defined as:

$$g(t) = logE[e^{tX}] \tag{1.3}$$

the $E[e^{tX}]$ is the moments generating function, so the moment-generating function for moments about zero can be written as:

$$G(t) = E[e^{tX}] = 1 + \sum_{n=1}^{\infty} \langle X^n \rangle \frac{t^n}{n!} \tag{1.4}$$

with the above definition, the nth order moments at zero can be expressed as:

$$\mu_n^{'} = \langle X^n \rangle = G^{(n)}(0) = \frac{\partial^n}{\partial t^n} G(t)|_{t=0} \tag{1.5}$$

Finally, we can get the relationship between cumulants, moments (zero) and central moments (mean):

$$C_n = \mu_n^{'} - \sum_{m=1}^{n-1} \binom{n-1}{m-1} C_m \mu_{n-m}^{'} \tag{1.6}$$

$$= \mu_n - \sum_{m=1,(n-m,n\geqslant 2)}^{n-1} \binom{n-1}{m-1} C_m \mu_{n-m} \tag{1.7}$$

Generally, the central moments are more useful than the moments at zero. The distribution function can be characterized by the various central moments, such as variance (σ^2), skewness (S), kurtosis (κ). The normalized 3rd central moment Skewness, represents the asymmetry of the probability distribution. For a distribution, a longer left tail means a negative skewness value, and a longer right tail means a positive skewness value as shown in figure **??**. For a symmetric or Gaussian distribution the Skewness value is zero. The fourth order central moment kurtosis, gives the information about the peakness of the probability distribution. Figure **??** shows the kurtosis of seven well known symmetric distributions.

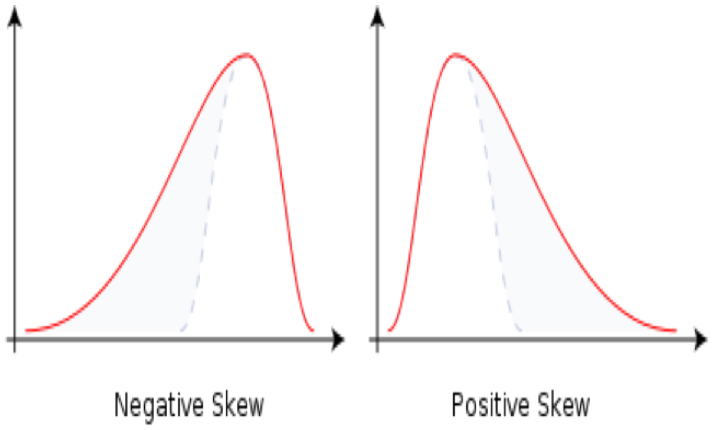

Figure 1.7: Example of two different distributions with negative Skewness (left panel) and positive Skewness (right panel).

In the moments analysis, we use N to represent the net-proton ($N_p - N_{\bar{p}}$), net-charge ($N_+ - N_-$) and net-kaon($N_{K^+} - N_{K^-}$) number in one event. The average value over whole event ensemble is denoted by $< N >$. We use $\delta N = N - < N >$ to denote the deviation of N from its mean value. Then the various order cumulants of event-by-event distributions of a variable N are defined as:

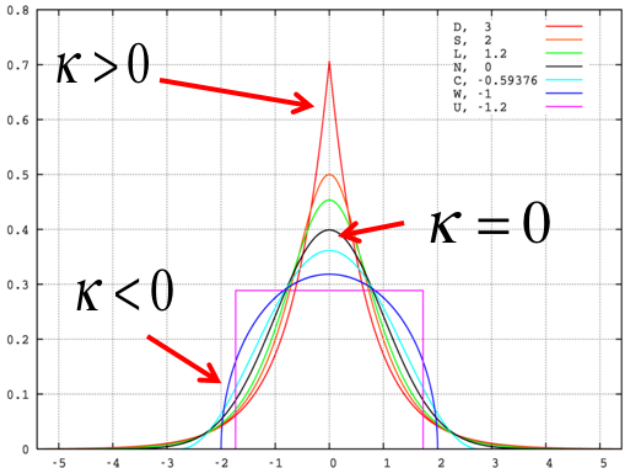

Figure 1.8: Probability distribution for seven well known distribution with unity variance, zero mean and skewness.

$$C_{1,N} =< N > \tag{1.8}$$

$$C_{2,N} =< (\delta N)^2 > \tag{1.9}$$

$$C_{3,N} =< (\delta N)^3 > \tag{1.10}$$

$$C_{4,N} =< (\delta N)^4 > -3 < (\delta N)^2 > \tag{1.11}$$

An important properties of the cumulants is their additivity for independent variables. If X and Y are two independent random variables, then we have $C_{i,X+Y} = C_{i,X} + C_{i,Y}$ for ith order cumulant. We will use this property in our study.

Once we have the definition of cumulants, various moments can be denotes as:

$$M = C_{1,N}, \sigma^2 = C_{2,N}, S = \frac{C_{3,N}}{(C_{2,N})^{\frac{3}{2}}}, \kappa = \frac{C_{4,N}}{(C_{2,N})^2} \tag{1.12}$$

In addition, the moments product $\kappa\sigma^2$ and $S\sigma$ can be expressed in term of cumulant ratio:

$$\kappa\sigma^2 = \frac{C_{4,N}}{C_{2,N}}, S\sigma = \frac{C_{3,N}}{C_{2,N}} \tag{1.13}$$

With above definitions, we can calculate various cumulants and ratios of cumulants for the measured event-by-event net-proton,net-charge and net-kaon multiplicity distributions at STAR.

1.3.2 Experimental Observables

One of the main goals of the high energy nuclear collisions is to explore the phase structure of the strongly interacting hot and dense nuclear matter. The QCD phase structure can be displayed in the two dimensional (temperature (T) Vs. baryon chemical potential (μ_B)) QCD phase diagram. The first principle Lattice QCD calculations demonstrate that the transition from the hadron phase to Quark-Gluon Plasma (QGP) at zero μ_B is a smooth crossover[15, 16]. While at large μ_B region, the phase transition could be of the first order[17, 18]. Thus, there should be a QCD Critical Point (CP) as the end point of the first order phase boundary towards the crossover region[13]. Experimental discovery of the critical point will be a landmark for the study of the phase structure of QCD matters. During the last five years, the scientific community has extensively studied the higher moments of conserved quantities distributions in heavy-ion collisions, such net baryon, net charge, and net strangeness, experimentally and theoretically, to search for the possible QCD critical point in the phase diagram of strongly interacting matters[19–29].

Fluctuations of conserved quantities, such as net-baryon (B), net-charge (Q) and net-strangeness (S), have long been predicted to be sensitive to the QCD phase transition and QCD critical point. Experimentally, one can measure various order moments (Variance(σ^2), Skewness(S), Kurtosis(κ)) of the event-by-event conserved quantities distributions in heavy-ion collisions. These moments are sensitive to the correlation length (ξ) of the hot dense matter created in the heavy-ion collisions[30] and also connected to the thermodynamic susceptibilities computed in Lattice QCD[13, 31, 32] and in the Hadron Resonance Gas (HRG)[33, 24, 23] model. For instance, the variance, skewness and kurtosis have been shown to be related to the different power of the correlation length as ξ^2, $\xi^{4.5}$ and ξ^7[30] , respectively. Theoretically, the n^{th} order susceptibilities $\chi^{(n)}$ are related to cumulant as $\chi^{(n)} = C_n/VT^3$[16], where V, T are the volume and temperature of the system, C_n is the n^{th} order cumulants of multiplicity distributions. In order to compare with the theoretical calculations, cumulant ratios ($S\sigma = C_3/C_2, \kappa\sigma^2 = C_4/C_2$) are constructed to cancel the volume effects. Thus, those moment products are also directly related to the ratios of various order susceptibilities as $\kappa\sigma^2$=$\chi_B^{(4)}/\chi_B^{(2)}$ and $S\sigma$=$\chi_B^{(3)}/\chi_B^{(2)}$. Due to the high sensitivity to the correlation length and the connection with the susceptibilities, one can use the moments of the conserved quantity

distributions to search for the QCD critical point and the QCD phase transition[34]. These have been widely studied experimentally and theoretically. To locate the critical point and map out the first order phase boundary, the first phase of the beam energy scan program has started in the year 2010 at RHIC. It tunes the Au+Au colliding energies from 200 GeV down to 7.7 GeV[35, 36], which correspond to a baryon chemical potentials range from 20 to 420 MeV[37–41].

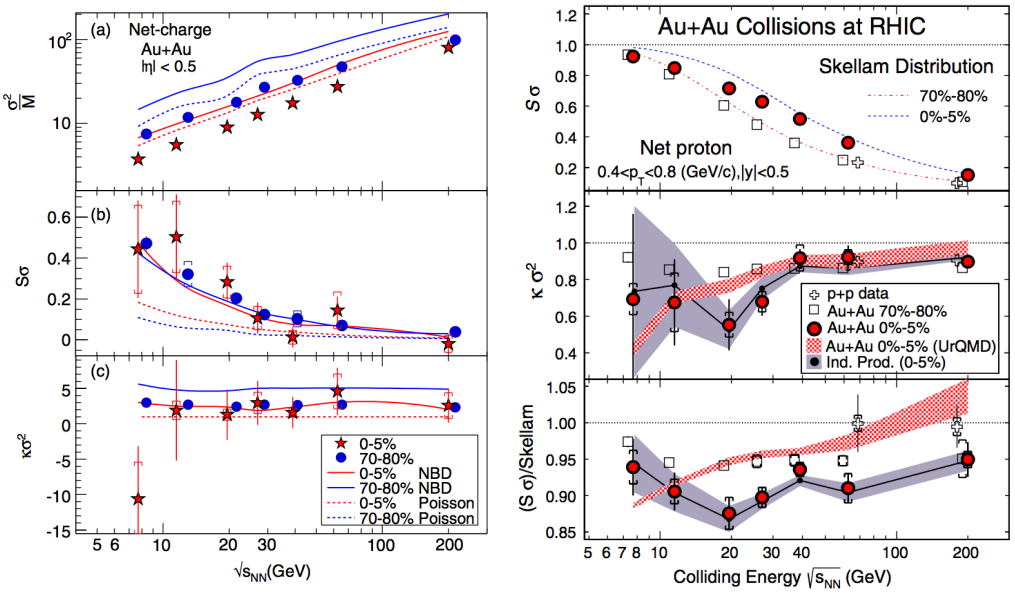

Figure 1.9: Collision energy and centrality dependence of the net-proton and net-charge of $S\sigma$ and $\kappa\sigma^2$ from Au+Au collisions at RHIC. Figure taken from[36, 42]

STAR experiment have published the measurements of net-proton and net-charge multiplicity fluctuations. Figure 1.9 shows the Collision energy and centrality dependence of the net-proton and net-charge of σ^2/M, $S\sigma$, and $\kappa\sigma^2$ from Au+Au collisions at RHIC, which were published at 2014[36, 42].

In this thesis, we performed the first measurements by the STAR experiment for the high moments of net-kaon multiplicity distributions in Au+Au collisions at $\sqrt{s_{NN}} = 7.7$, 11.5, 14.5, 19.6, 27, 39, 62.4, and 200 GeV. These results are compared with baseline calculations (Poisson and Negative Binomial) and UrQMD model with version 2.3.

Chapter 2

STAR Experiment

2.1 The Relativistic Heavy-Ion Collider

The Relativistic Heavy Ion Collider is a world class particle accelerator located at Brookhaven National Laboratory, Upton, NY. The project to study matter created in relativistic heavy ion collisions was proposed to the US Department of Energy in the year 2000. It is capable of accelerating nuclei for Au+Au collisions up to centre of mass energy $\sqrt{s_{NN}} = 200GeV$ and that for proton is $\sqrt{S}$= 500 GeV. A diagram of RHIC area at Brookhaven National Laboratory along with a design diagram is shown in the Figure 3.1[43]. These double storage rings are hexagonal shaped and 3.8 km long in circumference. The six interaction points (between the particles circulating in the two rings) are in the middle of the six relatively straight sections, where the two rings cross, allowing the particles to collide. The interaction points are enumerated by clock positions, with the injection near six. Two large experiments, STAR and PHENIX, are located at six and eight respectively. The RHIC consists of several subsystems like Linear Accelerator (Linac), Tandem Van de Graaff (TVG), Tandem- to-Booster line (TTB), Booster Accelerator, Electron Beam Ion Source (EBIS), Alternating Gradient Synchrotron (AGS), AGS-to-RHIC Line etc[44].

For heavy ion physics, RHIC accelerates heavy nuclei of various species to various energies. From its commissioning in 2000 to the present day (2016), RHIC has performed proton and proton (p + p), deuteron and gold (d+Au), copper and copper (Cu+Cu), gold and gold (Au+Au), copper and gold (Cu+Au), uranium and uranium (U+U), helium 3 and gold (He3+Au) collisions. RHIC has conducted a beam energy scan program for Au+Au collisions at center of mass energy $\sqrt{s_{NN}}$ from 7.7 GeV to the top energy of 200 GeV per nucleon pair. The various energies

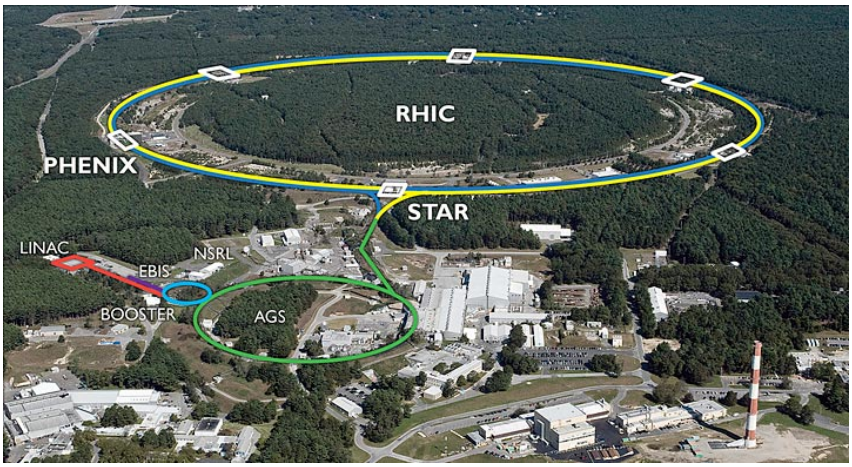

Figure 2.1: The Relativistic Heavy Ion Collider at Brookhaven National Laboratory.

facilitate the search for the possible critical point of QCD phase diagram[45, 46, 36, 42].In the first phase of the Beam Energy Scan (BES) program at RHIC, eight beam energies have already been analysized from $\sqrt{s_{NN}} = 7.7$GeV to 200GeV.

As Figure 2.1 shows, there are six interaction points on RHIC's 3.8 km long storage ring, among which are four experiments. They are STAR at 6 o'clock, PHENIX at 8 o'clock, PHOBOS at 10 o'clock, and BRAHMS at 1 o'clock. While PHOBOS and BRAHMS finished their missions in 2005 and 2006, respectively, the STAR and PHENIX experiments are still operating as of 2014.

2.2 STAR Detector

The Solenoidal Tracker at RHIC (STAR) detector is a general purpose detector. STAR has various detector subsystems. The main detector component is the TPC. It has full azimuthal and approximately 2.5 units of rapidity coverage. Three major detector subsystems used in this analysis are theTime Projection Chamber (TPC) and Time Of Flight (TOF) Detector, as shown in Figure 2.2. The conventional coordinate system at STAR uses the center of the Time Projection Chamber as the origin point. The beam pipe direction is the z direction with the west direction as being positive. The x direction is pointing to the south and the y direction is pointing up. For the d+Au collisions conducted in 2003 and 2008, the deuteron beam was going to the west, the positive z direction, and the gold beam was going to the east, the negative z direction. The azimuthal direction is in the x-y plane.

The cross-section layout of the STAR detector system is shown in Figure 2.3. The main tracking detector systems are TPC, two Forward TPCs (FTPC) and the silicon vertex tracker (SVT). The event multiplicity is measured by the Central Trigger Barrel (CTB). The Time of Flight (ToF) and a ring-imaging Cherenkov detector extend the particle identification up to a very high p_T. The measurement of photons, electrons and transverse energy of events use 10% of the barrel electromagnetic calorimeter. The detector subsystem also include two zero-degree calorimeters (ZDCs) at both of the ends which measure the daughter spectator neutrons.

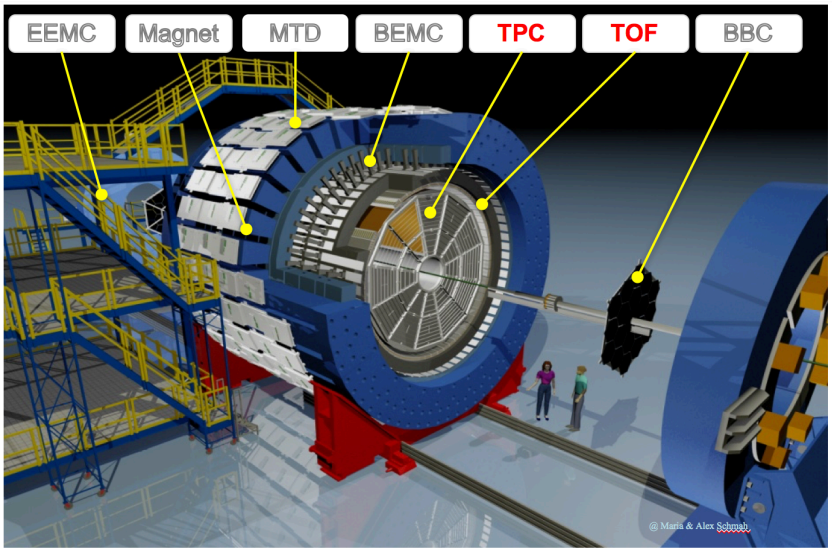

Figure 2.2: A perspective view of the STAR detector system with a cutaway for viewing inner sub-systems.

2.2.1 TPC – Time Projection Chamber

The TPC is the primary tracking detector at STAR[47]. The TPC records charged particle tracks, measures particle momentum and charge, and identifies particle species. It is 4 meters in diameter and 4.2 meters long, providing coverage of $-1.2< \eta < 1.2$ in pseudo-rapidity with high-quality tracking. With the STAR magnetic field of 0.5 Tesla in the z direction, the TPC can measure particles with momentum larger than 150 MeV/c.

The TPC tracks particles via ionization they cause in the TPC gas volume. As Figure 2.4 illustrates, the thin conductive Central Membrane, the concentric field cage cylinders and two end caps provide a nearly uniform electric field along the

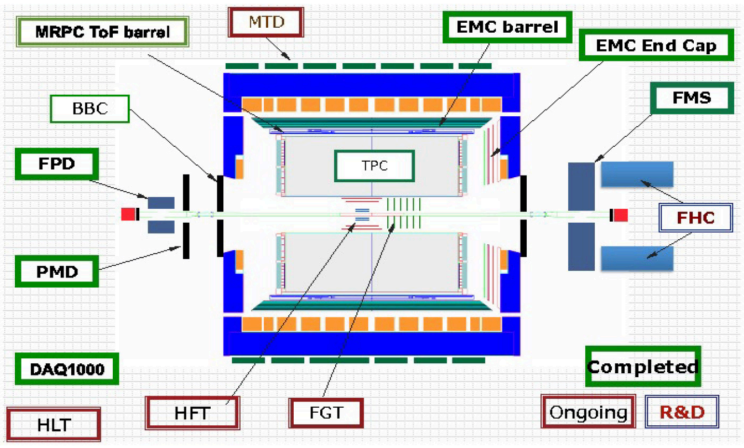

Figure 2.3: A cross-sectional cutaway of the STAR detector in its configuration with other sub systems.

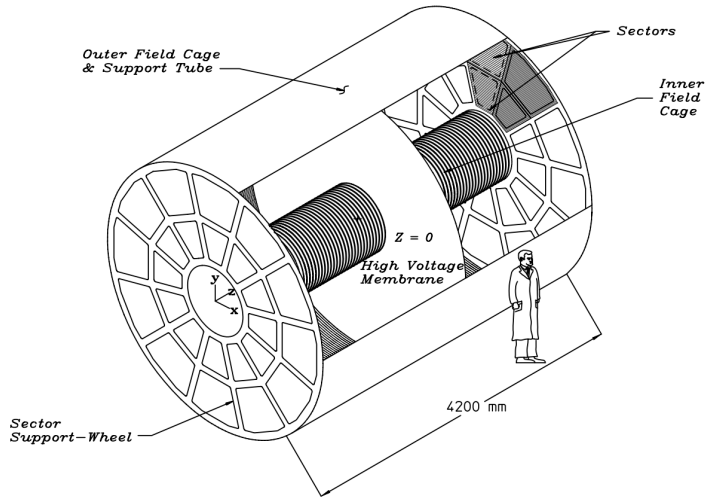

Figure 2.4: The STAR TPC surrounds a beam–beam interaction region at RHIC. The collisions take place near the center of the TPC.

beam pipe z direction in the TPC. As a charged particle traverses in the TPC gas, it ionizes the gas atoms and electrons are released. The ionization electrons drift in the electric field. The drifting electrons avalanche in the high field around the anode in the Multi-Wire Proportional Chambers at the end cap readout. The current collected by wire gives the hit location in the x-y plane and the current amplitude is proportional to the ionization energy loss. Each end cap has 12 sectors with 45 pad rows which gives a maximum of 45 hits per track. At the sector boundaries, the

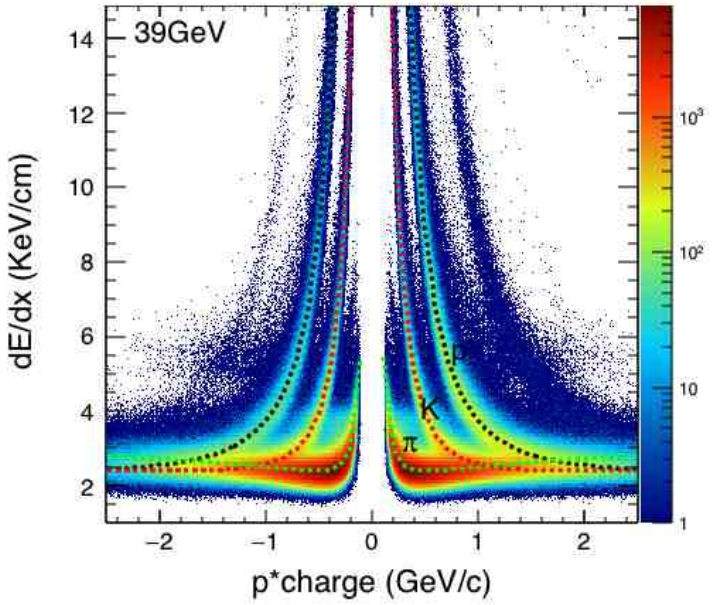

Figure 2.5: De/dx from Time Projection Chamber vs. rigidity (charge momentum) for Au +Au collision at $\sqrt{_{NN}} = 39$GeV.

particle reconstruction efficiency is low. Hence, the TPC has detecting deficiency at the sector boundaries. The z position of the charged particle is measured by the product of electron drifting time and drift velocity. The TPC is filled with P10 gas (Ar 90% + CH_4 10%) which provides a stable electron drift velocity that is insensitive to small variations of temperature and pressure. With the hit points x, y and z known, the helix of the particle motion is reconstructed. The particle helix and the STAR magnetic field magnitude together are used to determined the particle momentum and the particle charge sign using the Lorentz force equation of motion.

The ionization energy loss dE/dx measured from the readout current is used to identify the particle species. When a charged particle passes through the TPC gas volume, its ionizes the gas medium and loses energy. For the particle identification the information of dE/dX energy loss in the TPC gas medium is a valuable tool. The total charge collected on pad rows from each hit of a track are proportional to the ionization energy loss of the particle. The energy loss information works very well for the low momentum particles for particle identification. For the particles with higher momentum, the energy loss depends very weakly on the mass and after $v > 0.7c$, it's hard to separate particle species. For a particle passing through the

gas medium the dE/dX energy loss given by the Bethe-Bloch formula [48]:

$$Z = \frac{log[(dE/dx)_{measure}/(dE/dx)_{theory}]}{\sigma_E} \tag{2.1}$$

where $(dE/dx)_{theory}$ is the Bethe-Bloch [48] expectation for the given particle type (eg. π, K, p), it is parametrized as:

$$< dE/dx >_{BB} = A(1 + \frac{m^2}{p^2_{mag}}) \tag{2.2}$$

where m is the particle rest mass and p_{mag} is the particle momentum magnitude. This parametrization is found to describe the data well, with the normalization factor A determined from data. The expected value of z for the particle in study is around 0. In our higher moments of net-kaon distribution analysis, we select kaons and anti-kaons event-by-event by using cut $|Z_K| < 2$ within transverse momenta $0.2 < pT < 1.6(GeV/c)$ and mid-rapidity $|y| < 0.5$.

The particle tracks reconstructed by the TPC hit points are called global tracks. After finishing all track reconstructions in a collision event, the primary vertex of the collision, which is the estimate of the interaction point, is reconstructed from the global tracks. The Distance of Closest Approach (dca) is the closest distance from the primary vertex to the track helix. The tracks with dca less than 3 cm are refitted with the primary vertex, which are then called primary tracks. The primary track has better momentum resolution than the global track because the primary vertex position from all tracks is more precise than the single track when the track is from the primary vertex. However, when the track is from a secondary vertex, for example from a resonance decay, the primary track becomes less accurate than the global tracks. Hence, the dca is used to distinguish whether a track is from the primary vertex or a secondary vertex in the analysis.

2.2.2 TOF – Time Of Flight Detector

One of the major upgrade in STAR is the Time of Flight (ToF) detector which increase the discovery potential of STAR by increasing the capability of particle identification[49, 50]. This has enhanced the data quality being presented in this thesis. The increased particle identification helps to understand the large scale

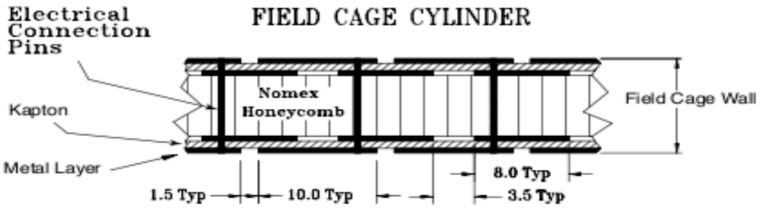

Figure 2.6: Field cage cylinder of TPC. The construction and composition are shown.

correlation and multi particle correlations produce in Au + Au collisions. The figure 3.17 shows the diagrammatic representation of the STAR TOF subsystems in association with TPC and beam pipe. The basic principle of TOF is to measure the time intervals of particle traveling within the TPC volume by using TPC information. The integrated TOF system consists of MRPC detectors, the gas system, the mechanical components and the electronics. TOF measures the time interval of TPC tracks with the help of an "event start" and a charged particle "stop detector". For each TPC reconstructed track with momentum, p, TOF measures the time interval Δt and inverse velocity $(1/\beta\ )$ by using,

$$\frac{1}{\beta} = \frac{c\Delta t}{s} \tag{2.3}$$

where, c is the speed of light and s total path length measure by TPC. The particle mass, M calculated by the associated momentum and inverse velocity via,

$$M = p\sqrt{(\frac{1}{\beta})^2 - 1} \tag{2.4}$$

TOF has 100 ps of time interval resolution. The combination of TPC and TOF made STAR a powerful particle identifier. The PID capability of STAR using TOF is shown in the Figure refFig:massResolution[51]. The momentum and path length resolution along with the measured hadron masses using TOF are also shown in the Figure 2.9. The upper (lower) pair shows the $M + \Delta M(M - \Delta M)$ dependence with the momentum. The solid and dashed pair lines represent the tracks near the center $(\eta \sim 0)$ and near the end of TPC $((\eta \sim 1)$.

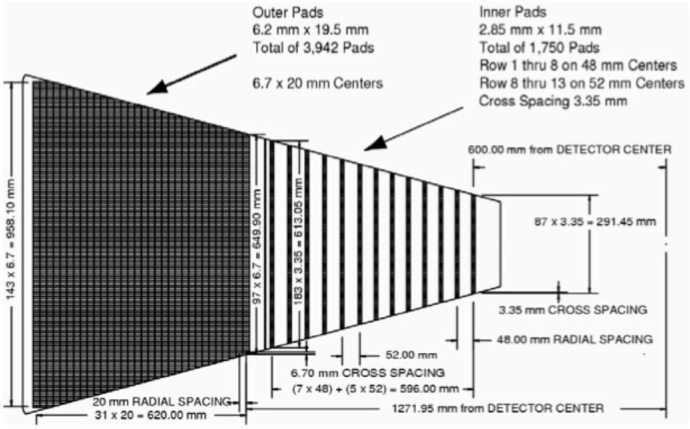

Figure 2.7: The anode pad plane with one full sector shown. The inner sub-sector is on the right and it has small pads arranged in widely spaced rows. The outer sub-sector is on the left and it is densely packed with larger pads.

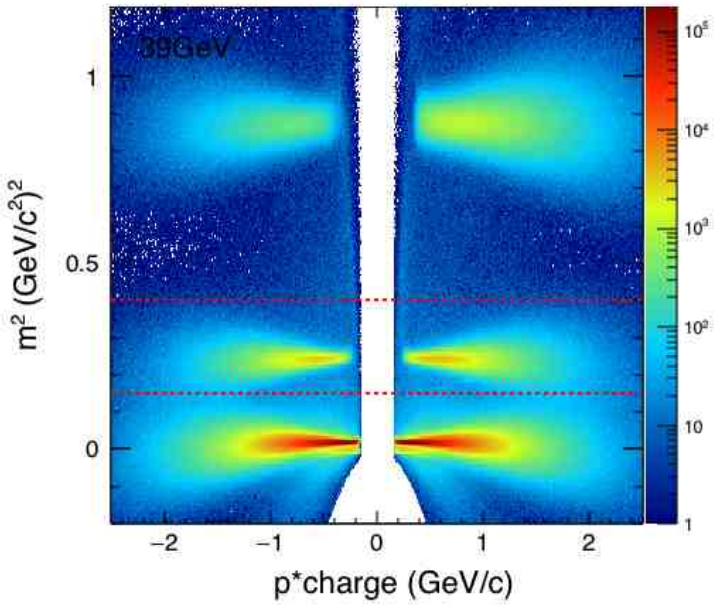

Figure 2.8: Mass square from Time Flight detector plotted as function of rigidity (charge momentum) for Au+Au collision at $\sqrt{_{NN}} = 39$GeV.

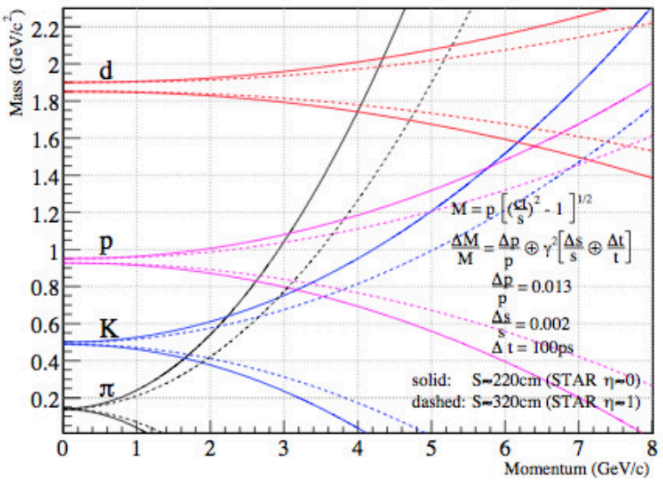

Figure 2.9: The particle mass resolution for a 100 *ps* total resolution of TOF as a function of momentum. Particles can be identified up to the regions where the lines are overlapping.

Chapter 3

Higher Moments of Net Kaon Multiplicity Distributions At RHIC

The Beam Energy Scan (BES) program aims to map the QCD phase diagram which normally plotted as a 2D plot (the temperature versus Baryon Chemical potential). By varying the colliding energy, RHIC can access a wide range of baryon chemical potential from 20MeV to 420MeV. RHIC has carried out the first phase of BES program in the year 2010, 2011 and 2014 to study the QCD phase diagram and search for the QCD critical point. The distribution of conserved quantities at the critical point would fluctuate. The higher moments of conserved quantities is sensitive probe to search for the critical point .

As mentioned before, we have constructed the net-kaon multiplicity distribution ($\Delta N_K = N_{K^+} - N_{K^-}$). And from that we can derived the higher order cumulants and volume independent cumulant ratios for the BES energies. In this chapter, we describe how the data was selected, which including the selecting of run number, event number and particle tracks. I will also discuss several factor which affect the determination of the higher moments like centrality bin width effect, auto-correlation effect, centrality resolution effect and the detector efficiency effect. Finally I will give the results of centrality and energy dependence of these cumulants and their ratios.

3.1 Data Selection

3.1.1 Data Set

In the first phase of the Beam Energy Scan (BES) program at RHIC, eight beam energies have already been carried out from $\sqrt{s_{NN}} = 7.7$GeV to 200GeV for Au+Au collisions. All the information about the data taken of these eight center-of-mass energies are listed in table 3.1. The data were taken in three different years, 2010, 2011, and 2014. We can see that the collisions at 200GeV have the largest statistics, and this is because the beam luminosity at 200GeV is higher compared with the low energy. With high luminosity, the collision between two nucleus have more chance to happen. The chemical freeze-out parameters T and μ_B shown in table 3.1 is obtained from the thermal model fitting[37].

$\sqrt{s_{NN}}$(GeV)	Statistics(M)	Year	μ_B(MeV)	T(MeV)
7.7	~ 4	2010	420	140
11.5	~ 12	2010	315	152
14.5	~ 20	2014	266	156
19.6	~ 36	2011	205	160
27	~ 70	2011	155	163
39	~ 130	2010	115	164
62.4	~ 67	2010	70	165
200	~ 350	2010	20	166

Table 3.1: Data set of Beam Energy Scan Phase I, including the statistics, the year of the production, and the corresponding baryon chemical potential and temperature which is extracted from Hadron Resonance Gas (HRG) model [37].

There are several bad runs associated with the data, depending on several conditions during the recording. It happens many times that the detector is not fully functional and that introduces a numbers of bad runs. Sometimes there are electronic problem during the run that may introduce bad runs. In RHIC the filling of the beam last between 15 minutes and 8 hours. The background noise is different for each fill and also depends on the beam energy. As the beam energy increase the beam spreads less in its lateral side so the background is reduced which in turn increases the relative number of good events. Table 3.2 shows the trigger information used in all the 8 energies for the analysis.These data sets were taken with a minimum bias trigger, which was defined by the zero degree calorimeters (ZDCs) [64], vertex position detectors (VPDs) [50], and beam-beam counters (BBCs) [65].

$\sqrt{s_{NN}}$(GeV)	Production	Trigger Name	TriggerID
7.7	AuAu7_Production	P10ih	290001, 290004
11.5	AuAu11_Production	P10ih	310004, 310014
14.5	production_15GeV_2014	P14ii	440015, 440016
19.6	AuAu19_Production	P11ik	340001, 340011, 340021
27	AuAu27_Production_2011	P11id	360001
39	AuAu39_Production	P10ik	280001
62.4	AuAu62_Production	P10id	270001, 270011, 270021
200	AuAu200_production	P1o1k	260001, 260011, 260021, 260031

Table 3.2: Trigger ID of mini-bias trigger for Beam Energy Scan phase I

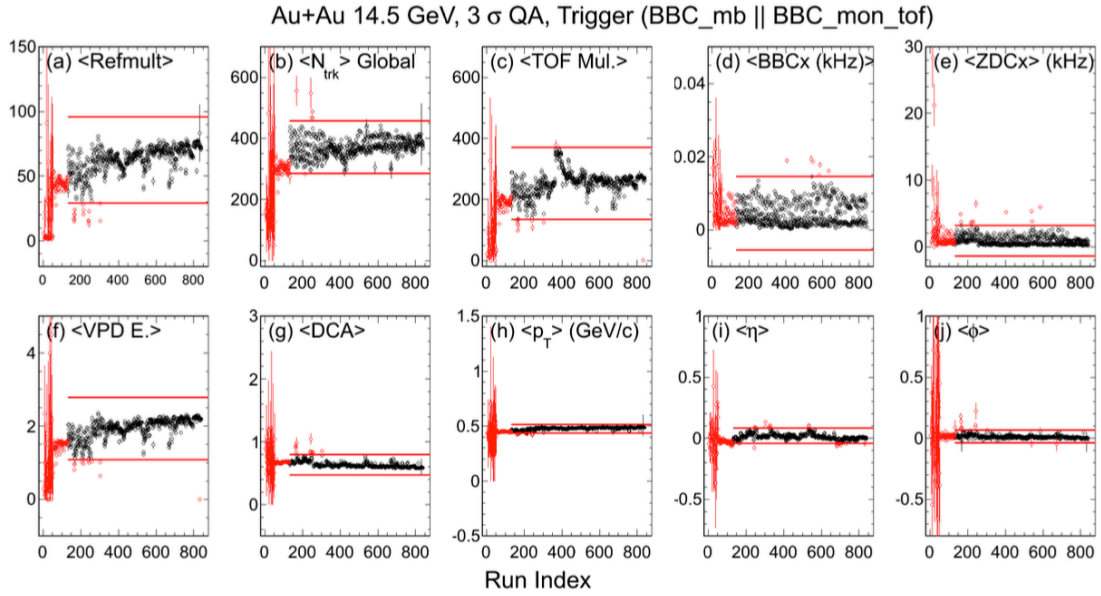

Figure 3.1: Run by run QA at Au+Au $\sqrt{s_{NN}}$ = 14.5 GeV Au+Au collisions.

To ensure the quality of our data, run by run study of many variables have already performed to remove the bad runs for every energy. For instance, we use the average reference multiplicity ($\langle Refmult \rangle$), $\langle dca \rangle$, $\langle p_T \rangle$, $\langle \eta \rangle$, $\langle \phi \rangle$ to remove the outlier runs beyond +/-3σ. The figure 3.1 shows the run by run QA at 14.5GeV Au+Au collisions. Each dot represent a run, and the red dots are the runs we decide not to use for the moments analysis.

3.1.2 Event Selection

In this analysis, we select only minimum bias trigger events for all Beam Energy Scan data. Along with the sensitivity in the critical fluctuations, higher moments

are also very sensitive to the experimental effects. These experimental effects includes background noise, drift in the TPC volume, noise due to the electrical signals etc. Sizable number of events that did not satisfy these criterion have been discarded to remove trigger biases. To remove these experimental effects from the data a good Quality Assurance (QA) is very important.

Events with a reconstructed primary vertex position in the fiducial region $|V_z| <$ 30 cm ($<$ 50 cm for 7.7GeV) and $|v_r| <$ 2cm ($<$ 1cm for 14.5GeV) were considered. At higher energies, the luminosity is always higher, which means that particles from a previous event could still be traversing the TPC when a new event triggered the detector to begin reading out data, a problem called pile-up. In this case, $|VpdVz - Vz| < 3$ is applied to suppress the pile-up events at 39, 62.4, and 200GeV. All the event cuts are listed in the table 3.3. From figure 3.2 to figure 3.4, we presented the distributions for $|V_z|$, $|VpdVz - Vz|$, V_x vs V_y, and V_r at $\sqrt{s_{NN}} = 39$ GeV, respectively. The event cuts for all the 8 energies are listed in table 3.3.

$\sqrt{s_{NN}}$(GeV)	$\|V_z\|$	$\|V_r\|$	$\|VpdVz - V_z\|$	TofMult
7.7	50	2	Nan	2
11.5	30	2	Nan	2
14.5	30	1	Nan	2
19.6	30	2	Nan	2
27	30	2	Nan	2
39	30	2	3	2
62.4	30	2	3	2
200	30	2	3	2

Table 3.3: Event selection cuts used in BESI energies.

3.1.3 Track Quality Cuts

Track Selection cuts for all energies are listed in table 3.4. In order to reduce the contamination from secondary charged particles, only primary particles have been selected, requiring a distance of closest approach (DCA) to the primary vertex of less than 1 cm. Tracks must have at least 15 points (nFitPoints) used in track fitting out of maximum of 45 hits possible in the TPC. The minimum number of points used to derive dE/dx values is limited to 5. To prevent multiple counting of split tracks, at least 52% of the total possible fit points are required (nHitsFit/NFitPoss).

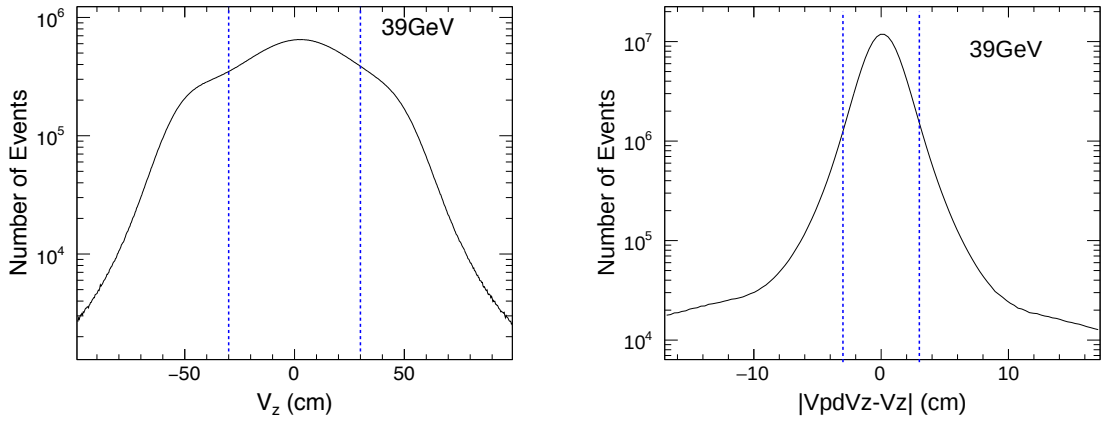

Figure 3.2: Left: V_z distribution for Au+Au 39GeV. Right: $VpdV_z$ minus V_z distribution for Au+Au 39GeV

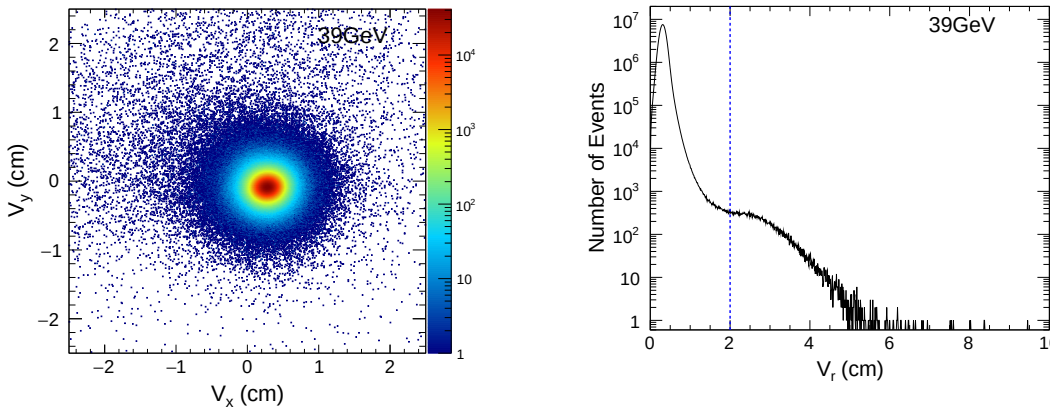

Figure 3.3: Left: V_x vs V_y distribution at Au+Au 39GeV. Right: V_r distribution at Au+Au 39GeV

All the tracks are taken within mid-rapidity $|y| < 0.5$, and transverse momentum range $0.2 < p_T < 1.6$ (GeV/c). These cuts are same for all the 8 energies.

Transverse Momentum (p_T)	$0.2 < p_T < 1.6$ (GeV)
Rapidity ($\|y\|$)	< 0.5
NfitPoints	> 15
nhitdedx	> 5
gDCA	< 1
nHitsFit/NFitPoss	> 0.52

Table 3.4: Track quality cuts used in BESI energies.

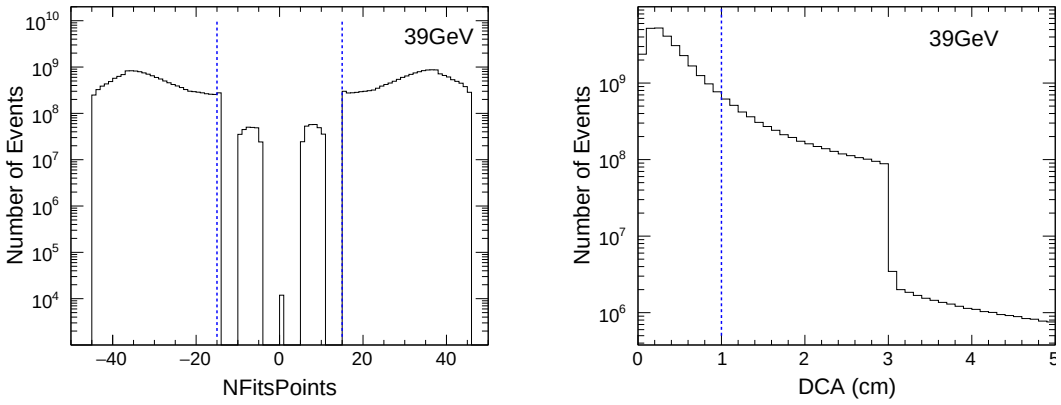

Figure 3.4: DCA Distribution for Au+Au 39GeV

3.2 Particle Identification

3.2.1 Kaon Identification

The STAR (Solenoidal Tracker At RHIC) detector [66] at BNL has a large uniform acceptance at mid-rapidity and excellent particle identification capabilities. Energy loss (dE/dx) in the Time Projection Chamber [47] and mass-squared (m^2) from the Time-Of-Flight [50, 49] detector are used to identify kaons.

The left panel of figure 3.5 show the ionization energy loss distributions as a function of particle momentum, which are measured by STAR TPC and can be used to identify charged particles. The energy resolution of the ionization energy loss measurement σ_E is the standard deviation of the gaussian distribution for the truncated mean values and is proportional to the energy deposit δE. The relative energy resolution for energy loss of STAR TPC is about σ_E/E =7.5%. To ensure good gaussian distributions, another variable is constructed to identify particles in the STAR experiment, which is defined as:

$$Z = \frac{log[(dE/dx)_{measure}/(dE/dx)_{theory}]}{\sigma_E} \tag{3.1}$$

where $(dE/dx)_{theory}$ is the Bethe-Bloch [67] expectation for the given particle type (eg. π, K, p), it is parametrized as:

$$< dE/dx >_{BB} = A(1 + \frac{m^2}{p^2_{mag}}) \tag{3.2}$$

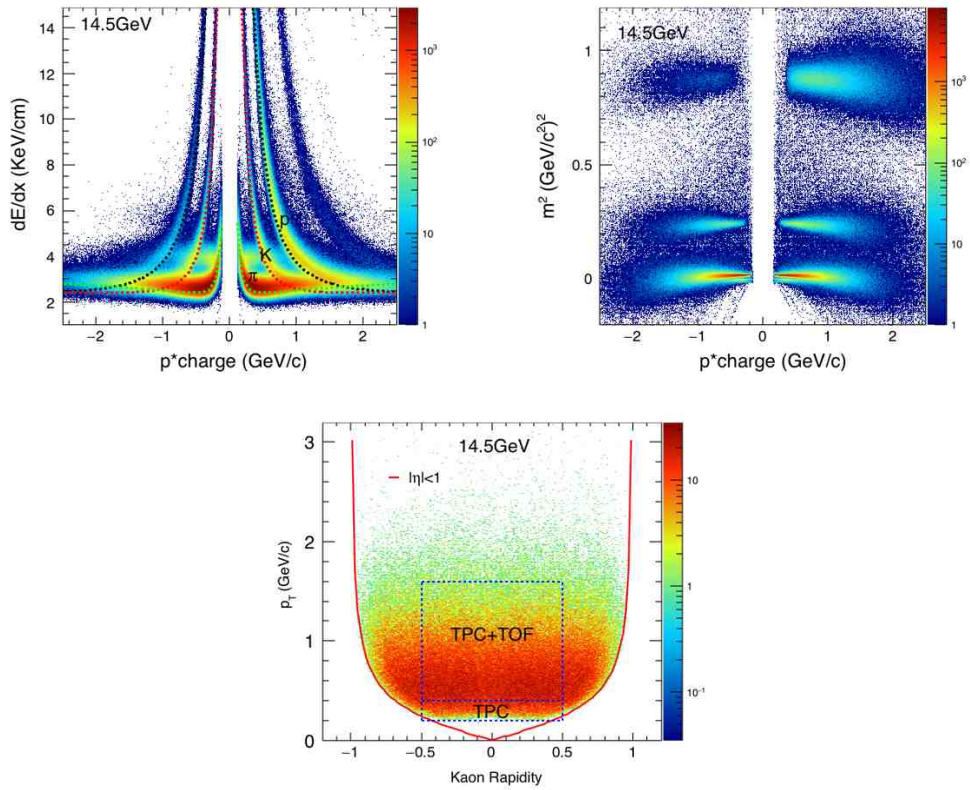

Figure 3.5: Left panel: The dE/dx of tracks plotted as function of rigidity (charge*momentum) for Au+Au 14.5GeV. The dashed lines in the figure are expectation line from bethe-bloch formula. Middle: Mass square vs. rigidity distributions at Au+Au 14.5 GeV. Right: The kaon accepted phase space within STAR TPC and TOF. The kaon distributed in the blue box are used in the moment analysis.

where m is the particle rest mass and p_{mag} is the particle momentum magnitude. This parametrization is found to describe the data well, with the normalization factor A determined from data. The expected value of z for the particle in study is around 0. In our higher moments of net-kaon distribution analysis, we select kaons and anti-kaons event-by-event by using cut $|Z_K| < 2$ within transverse momenta $0.2 < pT < 1.6(GeV/c)$ and mid-rapidity $|y| < 0.5$.

Another detector used to identify particles in our analysis is the Time of flight detector (TOF), which measures the flight time of a particle from the primary vertex of the collision. Once the time of flight and path length information are obtained, we can directly calculate the velocity of the particles and their mass.

$$\beta = \frac{v}{c} = \frac{L}{ct} \tag{3.3}$$

$$m^2 = (\frac{1}{\beta^2})xp = (\frac{c^2t^2}{L^2} - 1)xp \tag{3.4}$$

The right panel of figure 3.5 shows the mass square as a function of rigidity for Au+Au collision at $\sqrt{s_{NN}} = 14.5$ GeV. In this analysis, we use mass square cut $0.15 < m^2 < 0.4(GeV^2/c^4)$ to select proton and anti-proton within the p_T range $0.4 < pT < 1.6(GeV/c)$.

$0.2 < p_T <$0.4 (GeV)	$0.4 < p_T <$1.6 (GeV)
TPC	TPC + TOF
$\|Z_K\| < 2$	$\|Z_K\| < 2$,$0.15 < m^2 < 0.4$

Table 3.5: Kaon identification cuts used in different transverse momentum range.

The K^+ (K^-) for net-kaon are measured at mid-rapidity ($|y|$<0.5) within the transverse momentum 0.2<p_T<1.6 (GeV/c). In order to maximize the purity and efficiency of kaons, we split the transverse momentum range into two intervals: the lower p_T range (0.2<p_T<0.4 GeV/c) with TPC only, and the higher p_T range (0.4<p_T<1.6 GeV/c) with both TPC and TOF.

Figure 3.5 shows the kaon accepted phase space within STAR TPC and TOF. The left upper panel is the plot of de/dx vs. $p * Q$ from the TPC, the dashed lines are from the Bethe-Bloch function. We can see that the kaon band begin to merge with the pion band at p ~0.5GeV, so we need TOF at higher momentum range. The right upper panel is the plot of mass square vs. $p * Q$ from TOF, the middle band represent kaons. We can see that the kaon band is far away from the proton band (the upper band), will merge with pion band at about 2 GeV. In this analysis, the kaon included in the blue box, shown in the lower panel at figure 3.5 are used in the moment analysis.

3.2.2 Kaon Purity

In the lower p_T range (0.2<p_T<0.4 GeV/c) , $|n\sigma_K| < 2$ from TPC de/dx are applied. In the higher p_T range (0.4<p_T<1.6 GeV/c) , additional cut $0.15 < m^2 < 0.4$ from TOF are applied. Figure 3.6 shows the $n\sigma_K$ distribution from TPC de/dx at 14.5GeV, the lines are fitted by Gaussian. Figure 3.7 shows the mass square distributions from TOF, the lines are fitted by Student's t-distribution. The student's t-distribution can be expressed as:

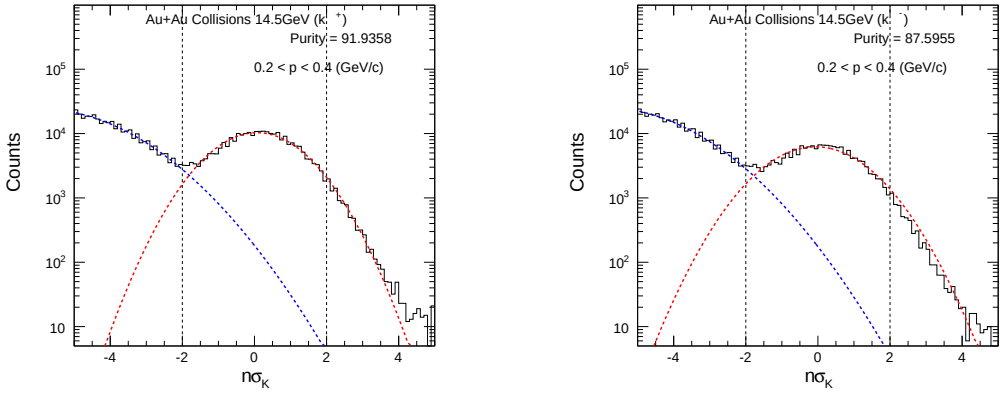

Figure 3.6: Left: nσ_{kaon} distribution from TPC de/dx for K^+ at 14.5 GeV. Right: nσ_{kaon} distribution from TPC de/dx for K^- at 14.5 GeV. Blue and red lines are fitted by gaussian.

$$f(t) = \frac{\Gamma(\frac{\nu+1}{2})}{\sqrt{\nu\pi}\Gamma(\frac{\nu}{2})}(1+\frac{t^2}{\nu})^{-\frac{\nu+1}{2}} \tag{3.5}$$

Once we have the fit parameters, we can get the purity of kaons in different p_T bins shown as figure 3.8. At lower momentum range ($0.2<p_T<0.4$ GeV/c), the purity is lower than high momentum range ($0.4<p_T<1.6$ GeV/c). The purity decrease with the momentum increase at higher momentum range.

3.3 Centrality Definition

The centrality of nucleus-nucleus collisions is an important parameter in heavy ion collision physics. It can be defined by several different parameters, such as impact parameter b, the number of nucleons that participate, N_{part} and the number of binary collisions, N_{coll}. Unfortunately, those geometry observables can not be directly measured and must be deduced from a combination of experimentally measured quantities and Monte-Carlo simulations. This usually is done by a purely geometric model, the so called Glauber model [68]. In heavy ion collision experiments it is not possible to reconstruct the vertex at high precision with low multiplicity.

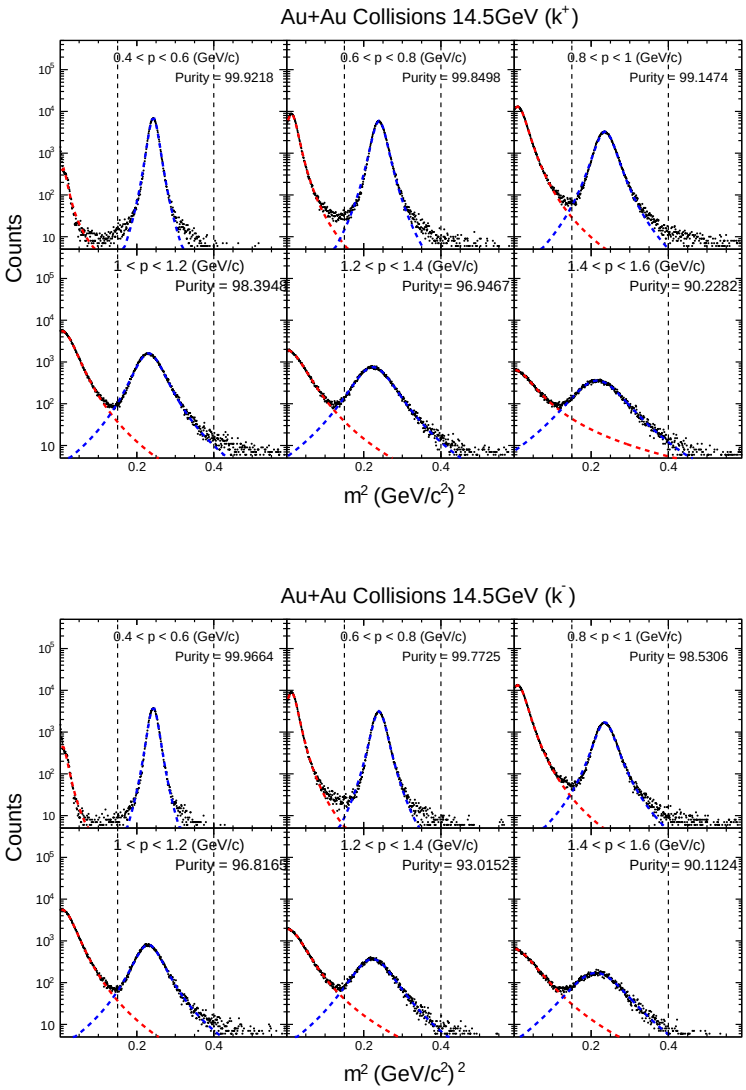

Figure 3.7: Left: mass square distribution from TOF for K^+ at 14.5 GeV. Right: mass square distribution from TOF for K^- at 14.5 GeV. The blue and red lines are fitted by Student's t-distribution.

In the peripheral events the multiplicity is very low hence the vertex reconstruction efficiency is also low.

In the STAR experiment, the efficiency-uncorrected charged particle multiplicity, which is also called reference multiplicity measured by the Time Projection Champer (TPC) and Time of Flight (TOF) combined with Glauber model simulations is used for centrality determination. In our analysis, the definition of reference multiplicity is defined as figure 3.9. It consist most of pions and protons. We call

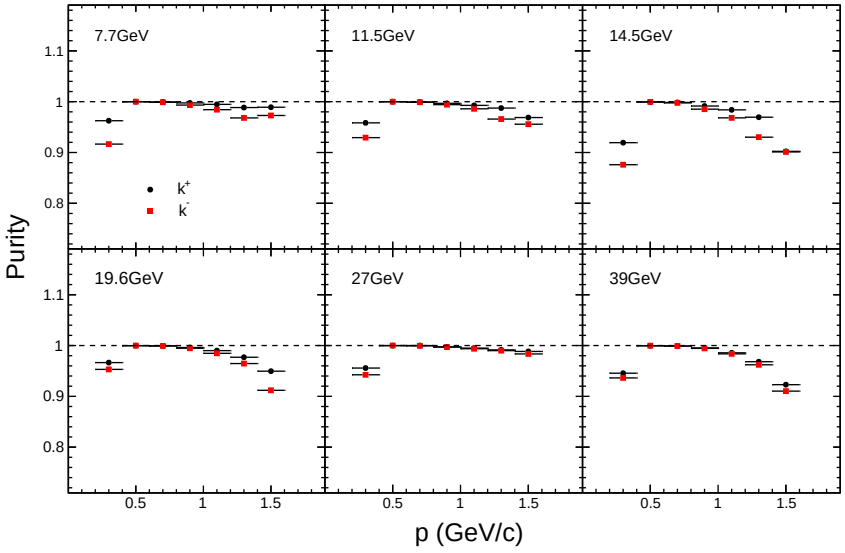

Figure 3.8: Kaon purity plotted as the function of momentum at Au+Au $\sqrt{s_{NN}}$ = 7.7, 11.5, 14.5, 19.6, 27 and 39GeV.

this definition refmult4. The reason that we only use the multiplicity of charged kaons and pions to define the centrality in Au+Au collisions is to avoid the effect of auto-correlation between kaons/anti-kaons involved in our moment analysis and in the centrality definition.

Figure 3.12 shows the normalized reference multiplicity 4 distributions for Au+Au collisions from $\sqrt{s_{NN}}$ = 7.7 GeV to 200GeV, which are used for centrality definition in net-kaon moments analysis. Red lines come from the fittings from Glauber MC simulation. We can calculate the reference multiplicity and determine the centrality classes with Glauber model simulations, in which the average geometrical parameters (N_{part} and N_{coll}) for each centrality bin can be also calculated. The blue bands indicate the 0-5% most central collisions, which is defined by binning the distribution on the basis of the fraction of the total integral.

3.4 Event-By-Event Net Kaon Distributions

After the kaon identification and centrality is done , we can get the event-by-event net-kaon distributions. Event-by-event net-proton multiplicity distributions for various colliding energies are measured within $0.4 < p_T < 0.8$ GeV/c

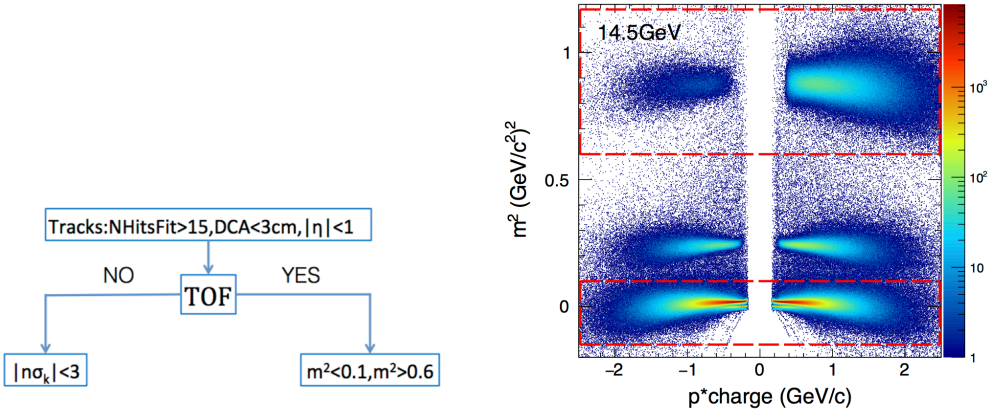

Figure 3.9: Left: Cuts used in the definition of reference multiplicity for centrality determination. Right: Mass square vs. rigidity to illustrate that reference multiplicity 4 is consist most of protons and pions.

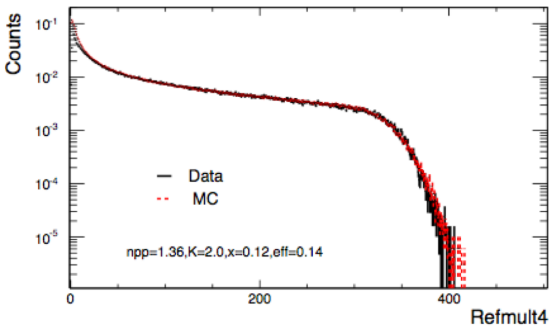

Figure 3.10: The Refmult4 distribution of data and MC at $\sqrt{s_{NN}}$= 7.7 GeV .

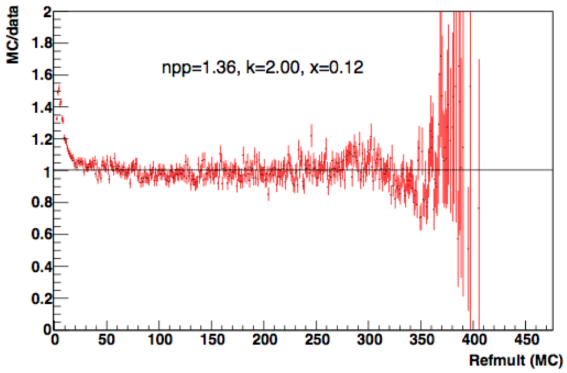

Figure 3.11: Right: The Refmult4 ratio of data to MC at $\sqrt{s_{NN}}$=7.7GeV.

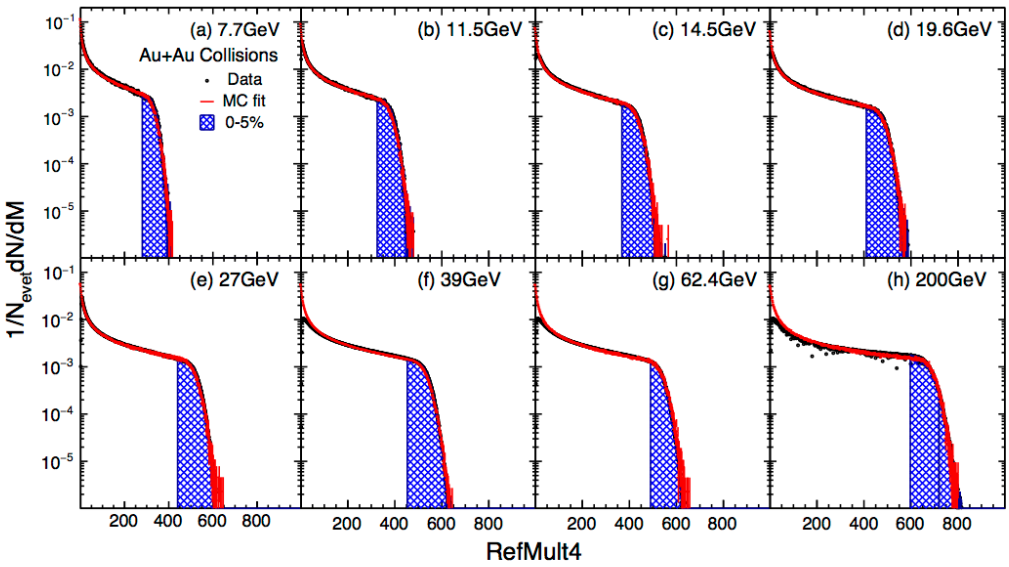

Figure 3.12: Normalized reference multiplicity 4 distributions for Au+Au collisions from $\sqrt{s_{NN}}$ = 7.7 GeV to 200GeV, which are used for centrality definition in net-kaon moments analysis. Red lines come from the fittings from Glauber MC simulation.

and $|y| < 0.5$. The uncorrected raw event-by-event net-kaon multiplicity distributions for 0-5% top central, 30-40% central, and 70-80% peripheral collisions are shown at figure 3.13. We can see that most central collisions have a wider distribution compared with peripheral collisions. The peak of the net-kaon distributions shift slightly towards the positive direction as the energy decreases. These distributions are raw distributions, and some effects need to be addressed to get final moments/cumulants. These effects include auto-correlation effects, effects of volume fluctuations, and finite detector efficiency [69, 56, 57].

3.5 The Volume Fluctuation Effect

In heavy-ion collisions, the collision centrality and/or initial collision geometry of two nuclei with finite volume is estimated by comparing the particle multiplicities with the Glauber simulation [68] and cannot be measured directly. This drawback in general can cause two effects in the moment analysis of particle multiplicity distributions within a finite centrality bin. One is the so-called CBWE [22], which

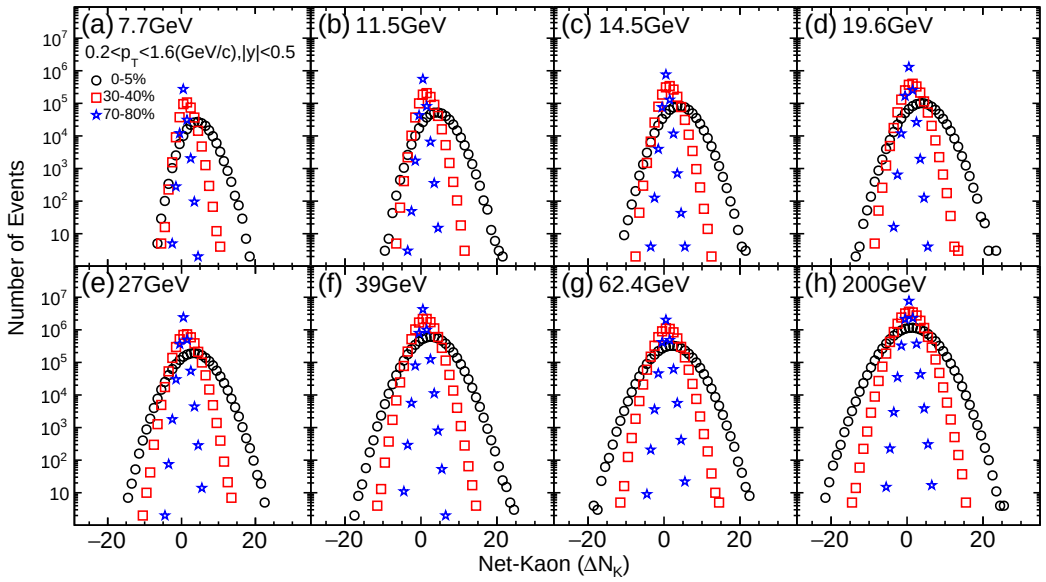

Figure 3.13: Uncorrected raw event-by-event net-kaon multiplicity distributions for Au+Au collisions at various $\sqrt{s_{NN}}$ for 0-5% top central (black circles), 30-40% central (red squares), and 70-80% peripheral collisions (blue stars).

is caused by volume variation within a finite centrality bin size and the other is the CRE, which is caused by the initial volume fluctuations [70].

3.5.1 The Centrality Bin Width Effect (CBWE)

Generally, we report the results for a wider centrality bin, such as 0-5% and 5-10%, for better statistical accuracy. But before calculating various moments of particle number distributions for one wide centrality bin, such as 0-5%, 5-10%, we should consider the so-called CBWE arising from the impact parameter (or volume) variations due to the finite centrality bin. This effect must be eliminated, as an artificial centrality dependence could be introduced due to finite centrality bin width.

To eliminate the CBWE, we have applied a technique called centrality bin width correction (CBWC), to calculate the various moments of particle number distributions in one wide centrality bin. These formulas are:

$$\sigma = \frac{\Sigma_r n_r \sigma_r}{\Sigma_r n_r} = \Sigma_r \omega_r \sigma_r \tag{3.6}$$

$$S = \frac{\Sigma_r n_r S_r}{\Sigma_r n_r} = \Sigma_r \omega_r S_r \tag{3.7}$$

$$\kappa = \frac{\Sigma_r n_r \kappa_r}{\Sigma_r n_r} = \Sigma_r \omega_r \kappa_r \tag{3.8}$$

where n_r is the number of events in the rth multiplicity for centrality determination, and σ_r, S_r and k_r represent the standard deviation, skewness and kurtosis of particle number distributions at rth multiplicity. The corresponding weight for the rth multiplicity is $\omega_r = n_r/\Sigma_r n_r$.

3.5.2 The Centrality Resolution Effect (CRE)

Particle multiplicity not only depends on physics-based processes, but also reflects the initial geometry of the heavy- ion collision. This indicates that the relation between measured particle multiplicity and the impact parameter does not correspond one-to-one, and there are fluctuations in the particle multiplicity even for a fixed impact parameter. Thus, it could have different initial collision geometry resolutions (centrality resolutions) for different centrality definitions with particle multiplicity.

Figure 3.14 shows the energy dependence of moment product $(S\sigma, \kappa\sigma^2)$ of net-proton multiplicity distributions for three different centralities (0-5%, 30-40%, 70-80%) with four different *eta* ranges in Au+Au collisions. We can find that the $\kappa\sigma^2$ (fourth order fluctuation) is more sensitive to the CRE than the $S\sigma$ (third order fluctuation), and it has a greater effect in the peripheral collision and at low energies. Thus, we should use a larger η range in the centrality definition for the real experimental moment analysis.

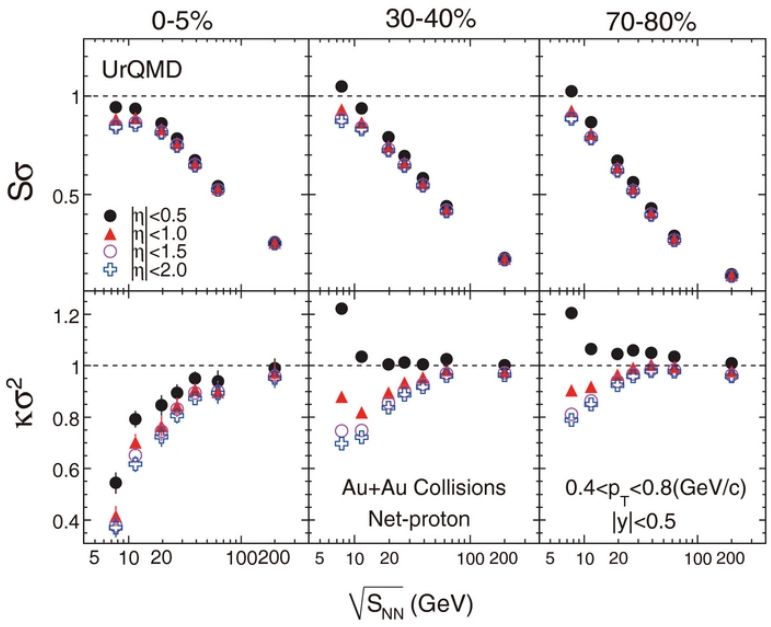

Figure 3.14: The energy dependence of the moments products $(S\sigma, \kappa\sigma^2)$ of net-proton multiplicity distributions for Au+Au collisions at $\sqrt{s_{NN}}$ = 7.7, 11.5, 19.6, 27, 39, 62.4, 200GeV in the UrQMD model with different centrality definitions.

3.6 Efficiency Correction

In real case, as we don't have 100% detector efficiency (include acceptance), we have to estimate the effect of the detector efficiency on the observable. Generally, the efficiency ε for particle detection can be treated as a binomial sampling $B(\varepsilon, N)$ with a efficiency parameter ε,

$$B(k; N, \varepsilon) = \frac{N!}{\kappa!(N-k)!}\varepsilon^k(1-\varepsilon)^{N-k} \tag{3.9}$$

where k is the detected number of particles.

Figure 3.15 and 3.16 show the p_T dependence of the TPC embedding efficiencies for π, K, p at Au+Au 39GeV. The TPC tracking efficiencies can be estimated by embedding Monte Carlo (MC) tracks in the real event, it can be expressed by: $\varepsilon = N_{rec}/N_{primary}$. The lines in the Figure 3.15 and 3.16 are fitted by the function:

$$y = p_0 e^{-(\frac{p_1}{x})^{p_2}} \tag{3.10}$$

Figure 3.17 and 3.18 show the p_T dependence of the TOF match efficiencies for π, K, p at Au+Au 39GeV. It can be expressed by: $\varepsilon = \frac{N_{(|n\sigma_{de/dx}|<0.5\&\&\beta>0)}}{N_{(|n\sigma|<0.5)}}$. The

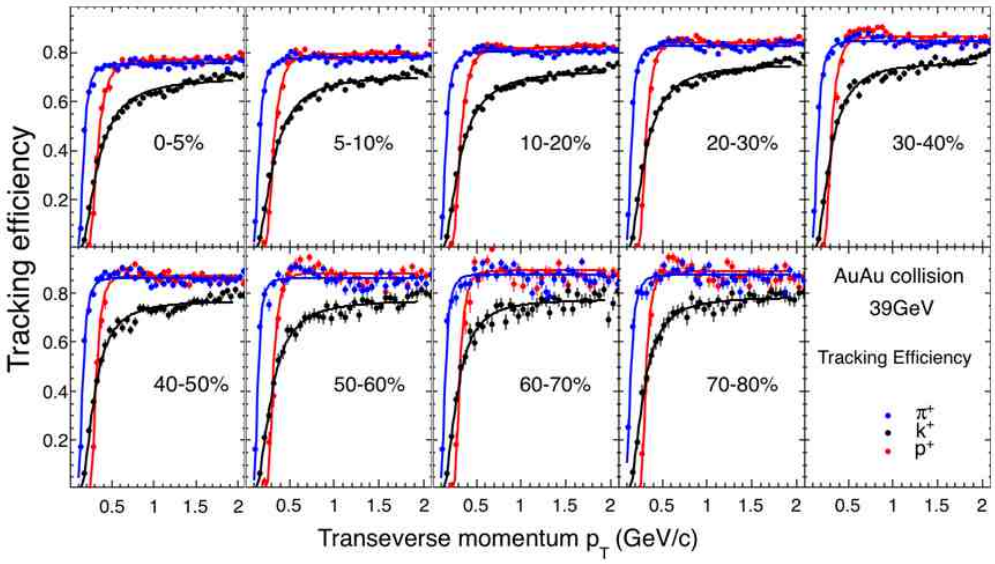

Figure 3.15: TPC tracking efficiencies for π^+, K^+, p at Au+Au 39GeV.

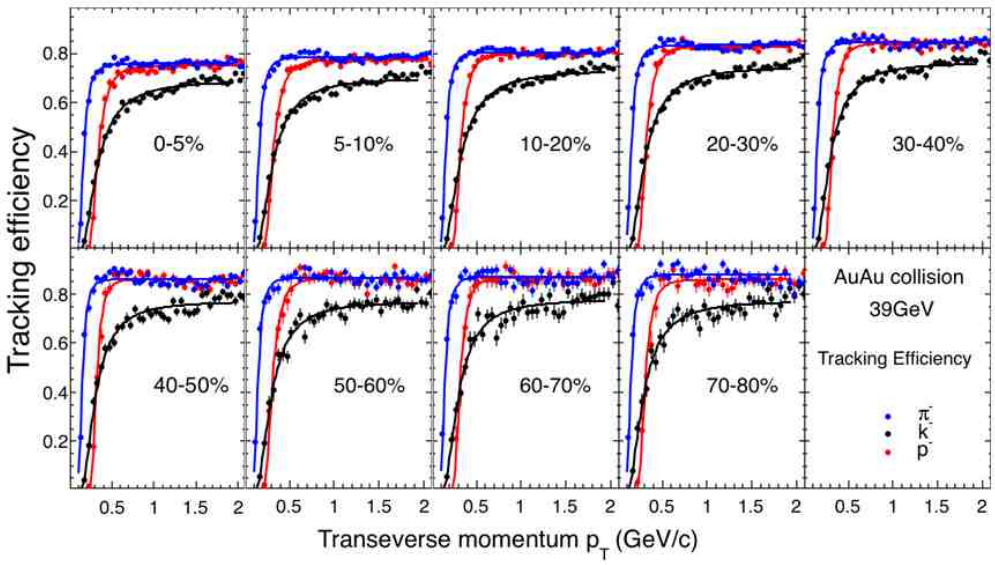

Figure 3.16: TPC tracking efficiencies for $\pi^-, K^-, \bar{p}$ at Au+Au 39GeV.

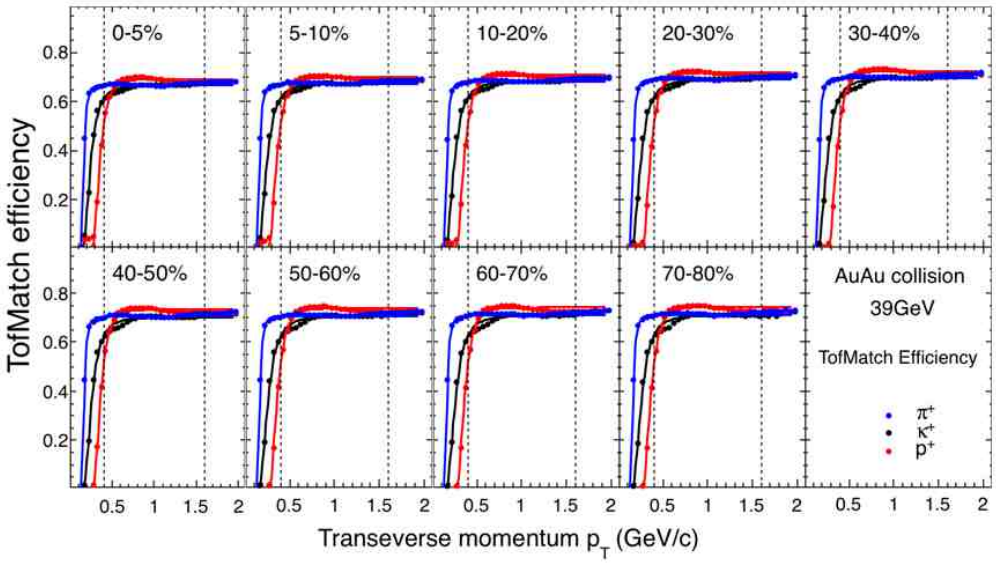

Figure 3.17: TOF match efficiencies for π^+, K^+, p at Au+Au 39GeV.

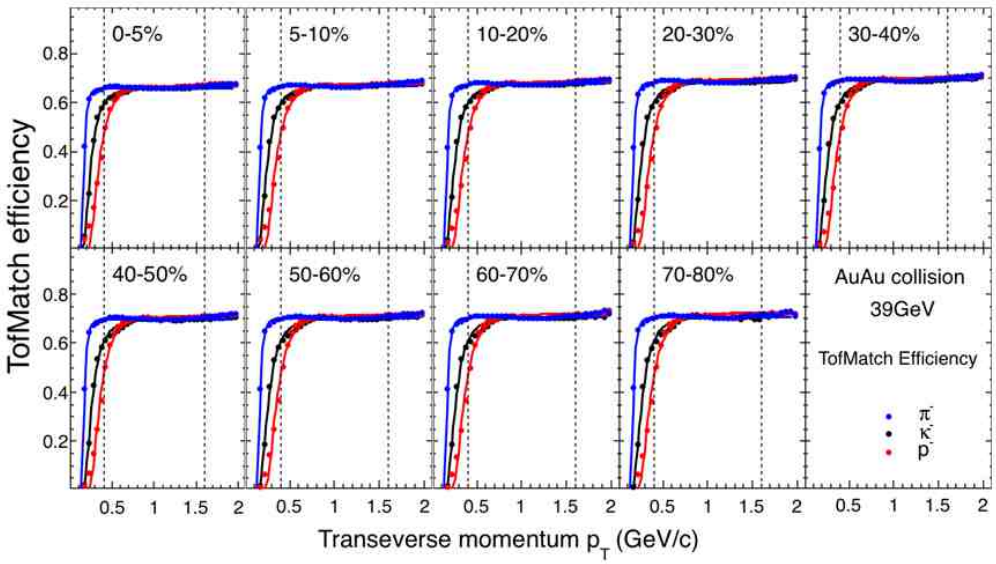

Figure 3.18: TOF match efficiencies for $\pi^-, K^-, \bar{p}$ at Au+Au 39GeV.

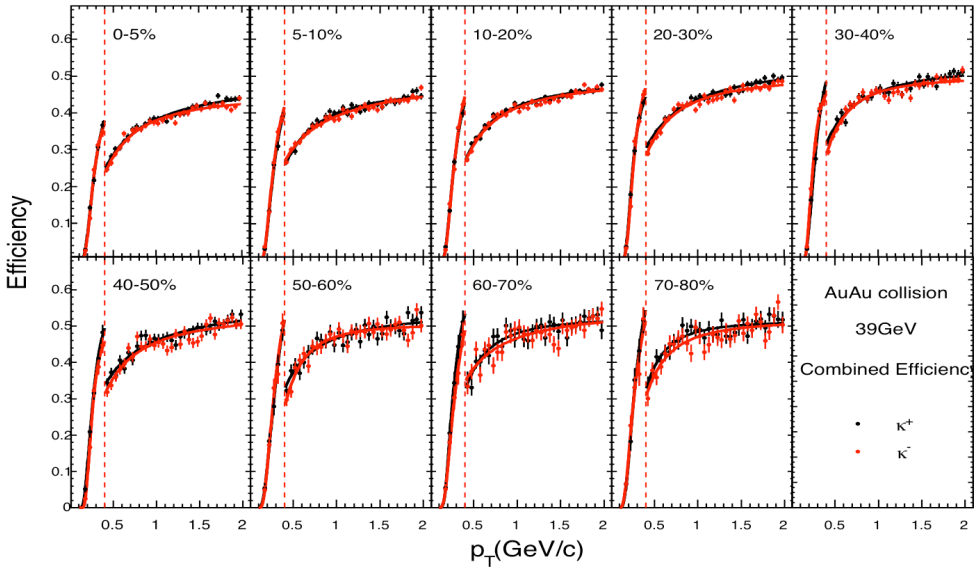

Figure 3.19: Combined efficiencies for K^+, K^- at Au+Au 39GeV.

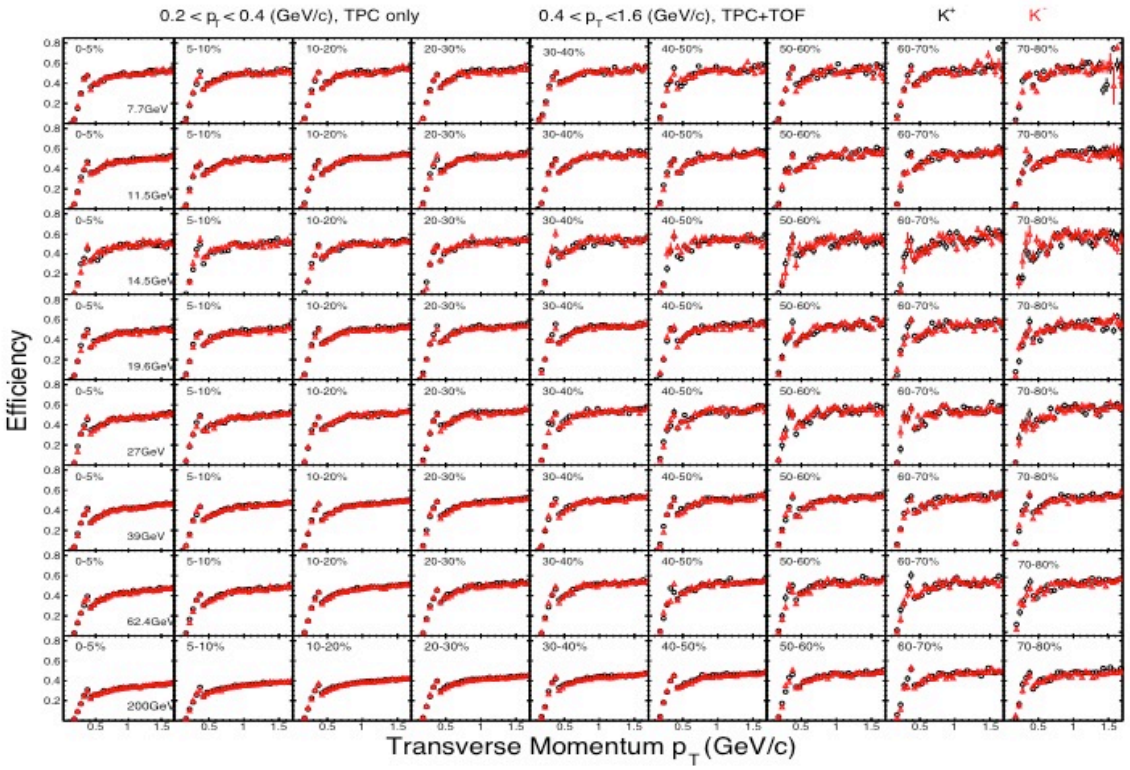

Figure 3.20: Combined efficiencies for K^+, K^- for all the Beam Energy Scan energies.

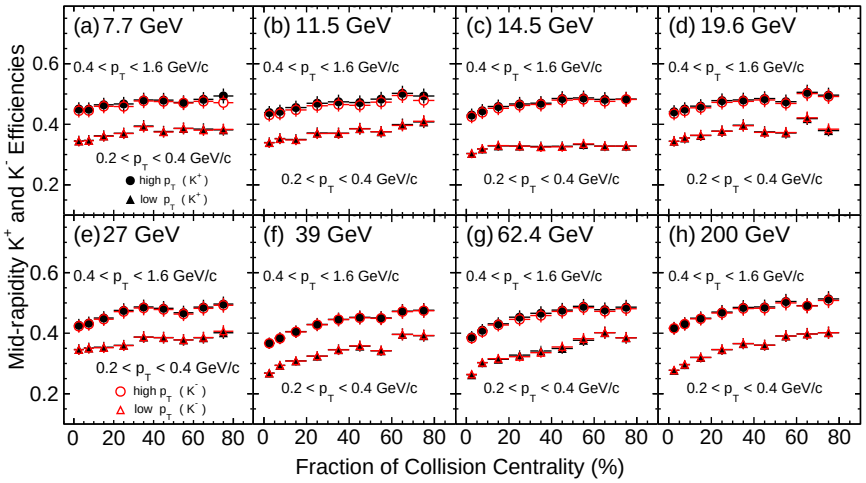

Figure 3.21: Collision centrality dependence of the p_T-averaged efficiencies in Au+Au collisions. For the lower p_T range ($0.2 < p_T < 0.4$ GeV/c, only the TPC is used. For the higher p_T range ($0.4 < p_T < 1.6$ GeV/c, both the TPC and TOF are used.

fit function is same with TPC.

Figure 3.19 show the centrality dependence of final combined efficiency of TPC and TOF at Au+Au 39GeV. Figure 3.20 shows all efficiencies of the BESI energies.

The efficiencies in our final calculation is p_T averaged efficiencies and can be calculated based on:

$$\varepsilon = \frac{\int_a^b \varepsilon^{'}(p_T) f(p_T) p_T dpT}{\int_a^b f(p_T) p_T dpT} \tag{3.11}$$

, where the transverse momentum dependence efficiency $\varepsilon^{'}(p_T)$ is from the embedding data with the same track cuts as used in the data analysis. $f(p_T)$ is the efficiency corrected transverse momentum spectra for kaon/anti-kaon. (a, b) is the momentum range. At lower p_T range $0.2 < p_T < 0.4(GeV/c)$, only TPC is used, and at higher p_T range $0.4 < p_T < 1.6(GeV/c)$, both TPC and TOF are used. So the final efficiencies can be calculated by:

$$< \varepsilon_{high} >= \frac{\int_{0.4}^{1.6} \varepsilon_{TPC}(p_T) f(p_T) p_T dpT}{\int_{0.4}^{1.6} f(p_T) p_T dp_T} \tag{3.12}$$

$$< \varepsilon_{low} >= \frac{\int_{0.2}^{0.4} \varepsilon_{TPC}(p_T)\varepsilon_{TOF}(p_T)f(p_T)p_T dpT}{\int_{0.2}^{0.4} f(p_T)p_T dp_T} \tag{3.13}$$

The efficiencies values in the final correction can be found in figure 3.21. Once we have all the efficiencies values, the efficiency correction can be done. We can express the moments and cumulants in terms of the factorial moments, which can be easily efficiency corrected.

$$\begin{aligned}
&F_{r_1,r_2} = F_{r_1,r_2}(N_{K_1^+} + N_{K_2^+}, N_{K_1^-} + N_{K_2^-}) \qquad (3.14)\\
&= \sum_{i_1=0}^{r_1}\sum_{i_2=0}^{r_2} s_1(r_1,i_1)s_1(r_2,i_2)\langle (N_{K_1^+} + N_{K_2^+})^{i_1}(N_{K_1^-} + N_{K_2^-})^{i_2}\rangle \\
&= \sum_{i_1=0}^{r_1}\sum_{i_2=0}^{r_2} s_1(r_1,i_1)s_1(r_2,i_2)\langle \sum_{s=0}^{i_1}\binom{i_1}{s} N_{K_1^+}^{i_1-s}N_{K_2^+}^{s} \sum_{t=0}^{i_2}\binom{i_2}{t} N_{K_1^-}^{i_2-t}N_{K_2^-}^{t}\rangle \\
&= \sum_{i_1=0}^{r_1}\sum_{i_2=0}^{r_2}\sum_{s=0}^{i_1}\sum_{t=0}^{i_2} s_1(r_1,i_1)s_1(r_2,i_2)\binom{i_1}{s}\binom{i_2}{t}\langle N_{K_1^+}^{i_1-s}N_{K_2^+}^{s}N_{K_1^-}^{i_2-t}N_{K_2^-}^{t}\rangle \\
&= \sum_{i_1=0}^{r_1}\sum_{i_2=0}^{r_2}\sum_{s=0}^{i_1}\sum_{t=0}^{i_2}\sum_{\mu=0}^{i_1-s}\sum_{\nu=0}^{s}\sum_{j=0}^{i_2-t}\sum_{k=0}^{t} s_1(r_1,i_1)s_1(r_2,i_2)\binom{i_1}{s}\binom{i_2}{t}\rangle \\
&\times s_2(i_1-s,\mu)s_2(s,\nu)s_2(i_2-t,j)s_2(t,k) \times F_{\mu,\nu,j,k}(N_{K_1^+}, N_{K_2^+}, N_{K_1^-}, N_{K_2^-})
\end{aligned}$$

$$F_{\mu,\nu,j,\kappa}(N_{K_1}, N_{K_2}, N_{\bar{K}_1}, N_{\bar{K}_2}) = \frac{f_{\mu,\nu,j,\kappa}(n_{K_1}, n_{K_2}, n_{\bar{K}_1}, n_{\bar{K}_2})}{(\varepsilon_{K_1})^{\mu}(\varepsilon_{K_2})^{\nu}(\varepsilon_{\bar{K}_1})^{j}(\varepsilon_{\bar{K}_2})^{\kappa}} \tag{3.15}$$

where $f_{\mu,\nu,j,\kappa}(n_{K_1}, n_{K_2}, n_{\bar{K}_1}, n_{\bar{K}_2})$ are the measured multivariate factorial moments of K^+ and K^-antiproton distributions. One can found the details about the efficiency correction in [69, 56, 71]

3.7 Error Estimation

3.7.1 Statistic Error Estimation

The statistical errors are based on Delta Theorem. The delta theorem is a well known theorem in statistics, which is used to approximate the distribution of a transformation of a statistic in large samples if we can approximate the distribution

of the statistic itself. Distributions of transformations of a statistic are of great importance in applications. The delta theorem can be describe as following,

Suppose that $\mathbf{X} = \{X_1, X_2, ..., X_k\}$ is normally distributed as $N(\mu, \Sigma/n)$, with Σ a covariance matrix. Let $\mathbf{g}(\mathbf{x}) = (g_1(\mathbf{x}), ..., g_m(\mathbf{x})), \mathbf{x} = (x_1, ..., x_k)$, be a vector-valued function for which each component function $g_i(\mathbf{x})$ is real-valued and has a nonzero differential $g_i(\mu)$, at $\mathbf{x} = \mu$. Put

$$\mathbf{D} = \left[\frac{\partial g_i}{\partial x_j}|_{x=\mu}\right]_{m\times k} \tag{3.16}$$

Then

$$\mathbf{g}(\mathbf{X}) \xrightarrow{d} N\left(g(\mu), \frac{D\Sigma D^{'}}{n}\right), \tag{3.17}$$

where n is the number of event. The details about the error estimation can be found in [56, 57].

3.7.2 Systematic Error Estimation

To evaluate the systematic uncertainties in this analysis we have studied four basic track quality parameters. The parameters used for the systematic study are the distance of closest approach (DCA) to the primary vertex, number of fit points used to fit the trajectory of each tracks (nFitPoints), the $n\sigma_K$ used for the kaon PID, and the efficiency fluctuation. The following quality cuts have been used to extract the systematic errors:

- NFitPoint: 9, 12, 15(default), 18, 20
- DCA: 0.8, 0.9, 1.0(default),1.1,1.2
- $n\sigma_K$: 1, 1.5, 2, 2.5, 3
- Efficiency: (K^+: lower p_T, higher p_T)+(K^-: lower p_T, higher p_T)
  (+5%, +5%)+(+5%, +5%)
  (-5%, -5%)+(-5%, -5%)
  (+2%, -2%)+(+2%, -2%)
  (-2%, +2%)+(-2%, +2%)

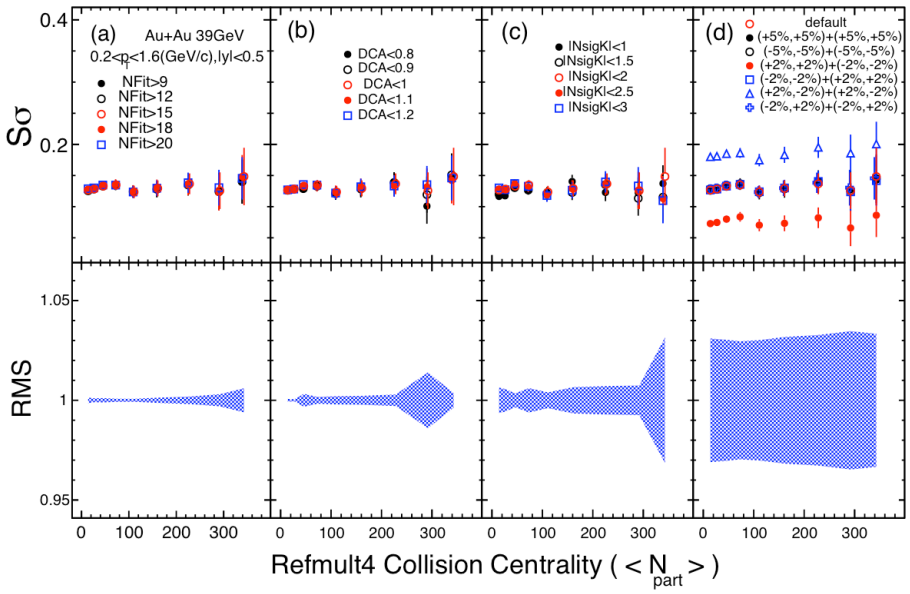

Figure 3.22: Systematic errors estimation of $S\sigma$ for different cuts at Au+Au 39GeV.

The results from each set of the cuts are corrected for efficiency. For each set of the cuts, we can calculate the point by point difference between the efficiency corrected results from the varied cuts and the defaults cuts. Then the systematic errors is the sum square root of those difference.

$$RMS = \sqrt{\frac{1}{N}\Sigma_{i-1}^{N}(X_i - Y)^2} \tag{3.18}$$

where, X_i is the observable in our case moments and moments products from different systematic cuts and Y is the moments and moment products from default cuts. The systematic errors can be calculated as,

$$SysErr. = \sqrt{\Sigma_j RMS_j^2} \tag{3.19}$$

where, the summation is over the number of the variables. The systematic study has been done after efficiency calculation. Figure 3.22 and 3.23 show centrality dependence of the efficiency corrected $S\sigma$ and $\kappa\sigma^2$ for variation of track cuts and systematic error in Au+Au collisions $\sqrt{s_{NN}} = 39$GeV.

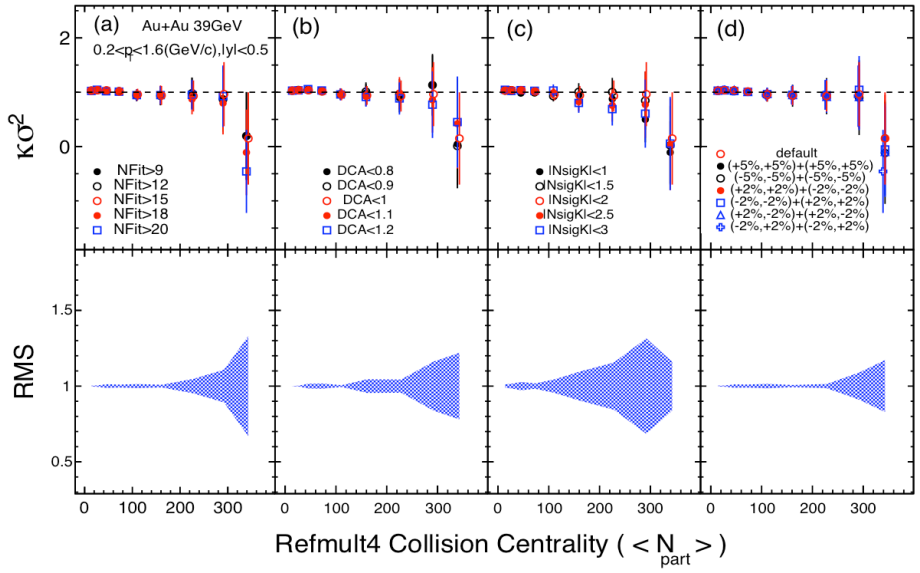

Figure 3.23: Systematic errors estimation of $\kappa\sigma^2$ for different cuts at Au+Au 39GeV.

3.8 Baselines Study

3.8.1 Poisson Baseline

Assuming kaon and anti-kaon are independent distributed as Poisson distribution. The difference of two independent Poisson distributions distributed as the Skellam distributions. It's probability density formula is:

$$P(N) = (\frac{\mu_1}{\mu_2})^(N/2) I_N(2\sqrt{\mu_1\mu_2]}) e^{-(\mu_1+\mu_2)} \tag{3.20}$$

, where the μ_1 and μ_2 are the mean value of two Poisson distributions, respectively, the $I_k(z)$ is the modified bessel function of the first kind. Then the net-kaon distribution can be expressed as skellam distribution. Then the expectation of the various cumulants (C_1, C_2, C_3, C_4) and moment products (σ^2/M, Sσ, $\kappa\sigma^2$) can be

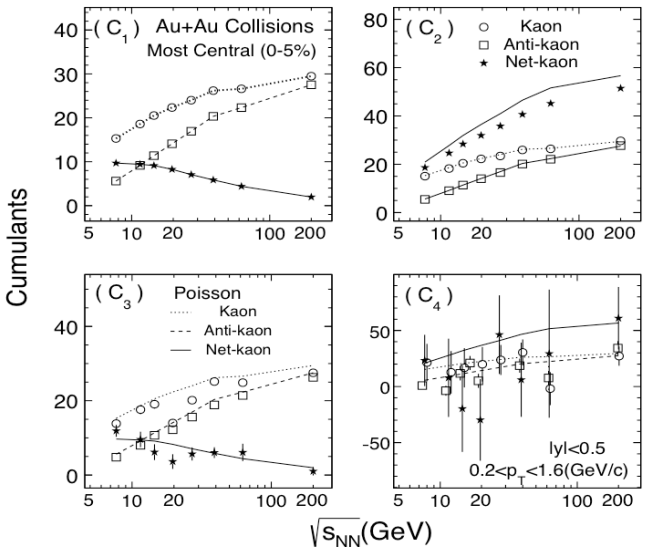

Figure 3.24: Energy dependence of cumulants of kaon, anti-kaon, and net-kaon multiplicity distributions for Au+Au collisions at $\sqrt{s_{NN}}$ = 7.7, 11.5, 14.5, 19.6, 27, 39, 62.4, and 200GeV for most central(0-5%). The lines are from Poisson expectations. The results are corrected for the kaon reconstruction efficiency.

written by:

$$C_{2n} = \mu_K + \mu_{\bar{K}}, (n = 1, 2, 3, ...) \tag{3.21}$$

$$C_{2n-1} = \mu_K - \mu_{\bar{K}}, (n = 1, 2, 3, ...) \tag{3.22}$$

$$\sigma^2/M = \frac{\mu_K + \mu_{\bar{K}}}{\mu_K - \mu_{\bar{K}}} \tag{3.23}$$

$$S\sigma = \frac{\mu_K - \mu_{\bar{K}}}{\mu_K + \mu_{\bar{K}}} \tag{3.24}$$

$$\kappa\sigma^2 = 1 \tag{3.25}$$

, where the μ_K is the mean value of kaon distribution, and the $\mu_{\bar{K}}$ is the mean value of anti-kaon distribution.

3.8.2 Negative Binomial Distribution Baseline

Binomial Distribution (BD) and Negative Binomial Distribution (NBD) are widely used to describe distributions with variance smaller than mean and larger than mean, respectively. Negative Binomial Distribution (NBD) can be expressed

as:

$$NB(k;r,p) = \binom{k=r-1}{k} p^r (1-p)^k \tag{3.26}$$

The cumulants for BD and NBD are:

$$C_2 = \sigma^2 = r\mu \tag{3.27}$$

$$C_3 = S\sigma^3 = r\mu(2r-1) \tag{3.28}$$

$$C_4 = \kappa\sigma^4 = r\mu(6r^2 - 6r + 1) \tag{3.29}$$

,where μ is the mean value, $r = \frac{\sigma^2}{\mu} = 1 - \varepsilon < 1$ is the ratio between variance and mean value. If we assume the kaon and anti-kaon are independent distributed. Then we can obtain the cumulants of net-kaon distributions:

$$C_n = C_n^+ + (-1)^n C_n^- \tag{3.30}$$

3.9 Results and Disscussion

The results presented here are obtained from the Au+Au collisions at 7.7, 11.5, 14.5, 19.6, 27, 39, 62.4 and 200 GeV in the first phase of the BES program at RHIC. Energy loss (dE/dx) in Time Projection Chamber and mass-squared (m^2) from Time of Flight are used to identify kaons within $0.2 < p_T < 1.6$ (GeV/c) and at mid-rapidity $|y| < 0.5$. The centrality is determined from the uncorrected charge particle multiplicity by excluding the kaons and anti-kaons within pseudo-rapdity $|\eta| < 1$.

3.9.1 Centrality Dependence of Cumulants and Cumulant Ratios

The centrality dependence of cumulants (C_1, C_2, C_3, andC_4) plotted as a function of N_{part} is presented in Figure 3.25. The centrality dependence of moment products (σ^2/M, $S\sigma$, and $\kappa\sigma^2$) plotted as a function of N_{part} is presented in Figure 3.26, 3.27, and 3.28, respectively. The results are corrected for the finite centrality bin width effects . We use the Delta theorem approach to obtain statistical errors.

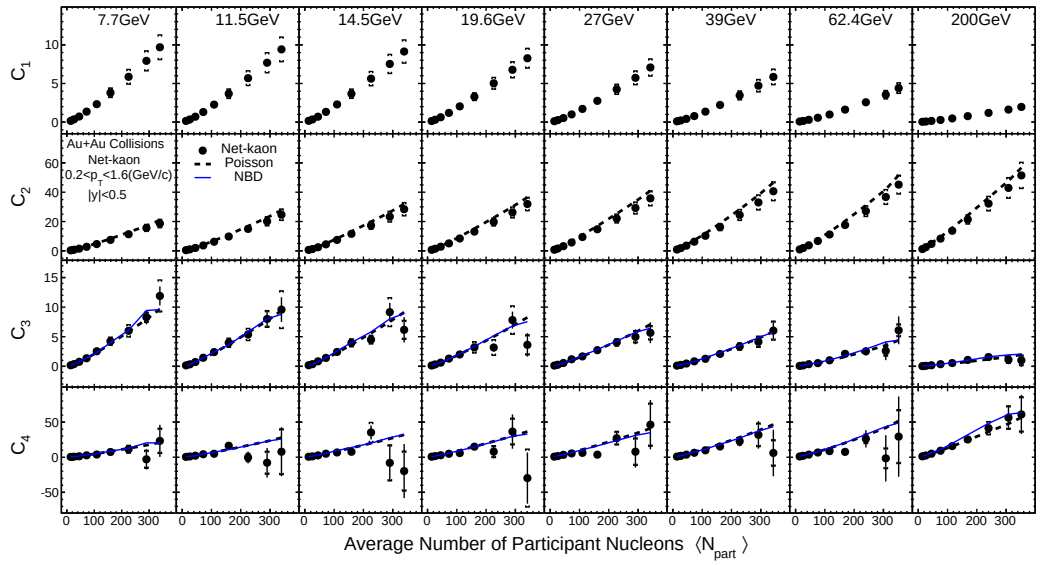

Figure 3.25: Centrality dependence of cumulants for net-kaon multiplicity distributions in Au+Au collisions at $\sqrt{s_{NN}}$ = 7.7, 11.5, 19.6, 27, 39, 62.4, and 200GeV. The results are corrected for the kaon reconstruction efficiency.

Figure 3.25 shows the collision centrality dependence of cumulants C_1, C_2, C_3, and C_4 for ΔN_K distributions at the measured collision energies as a function of the average number of participant nucleons ($\langle N_{\rm part}\rangle$). The statistical errors for the four cumulants are obtained using the Delta theorem approach. The efficiency corrections have been done by using the values shown in figure 3.21. In general, the cumulants show a nearly linear variation with $\langle N_{\rm part}\rangle$, which can be understood as the additivity property of the cumulants by increasing the volume of the system. This reflects that the cumulants are extensive quantities that are proportional to system volume. The decrease in the C_1 and C_3 values with increasing collision energy indicates that K^+/K^- approaches unity for the higher collision energies.

Figure 3.25 shows the Poisson and negative binomial distribution (NBD)[72] expectations. The Poisson baseline is constructed using the measured means of the multiplicity distributions of K^+ and K^-. The NBD baseline is constructed using both the measured means and the measured variances of the multiplicity distributions of K^+ and K^-. Assuming that the event by event multiplicities of K^+ and K^- are independent random variables, the Poisson and NBD assumptions result in baselines that provide references for the moments of the net-kaon distributions.Within uncertainties, the measured cumulants values and ratios are consistent with both the Poisson and NBD baselines.

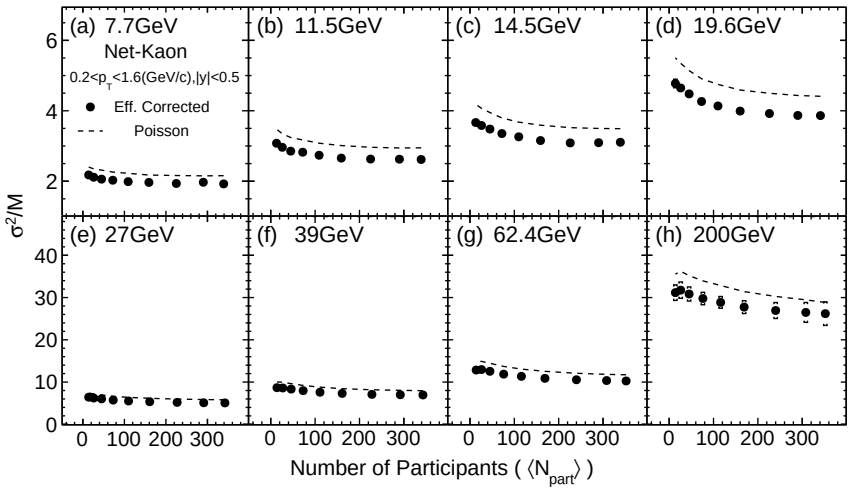

Figure 3.26: Centrality dependence of σ^2/M for net-kaon multiplicity distributions in Au+Au collisions at $\sqrt{s_{NN}}$ = 7.7, 11.5, 14.5, 19.6, 27, 39, 62.4, and 200GeV. The results are corrected for the kaon reconstruction efficiency.

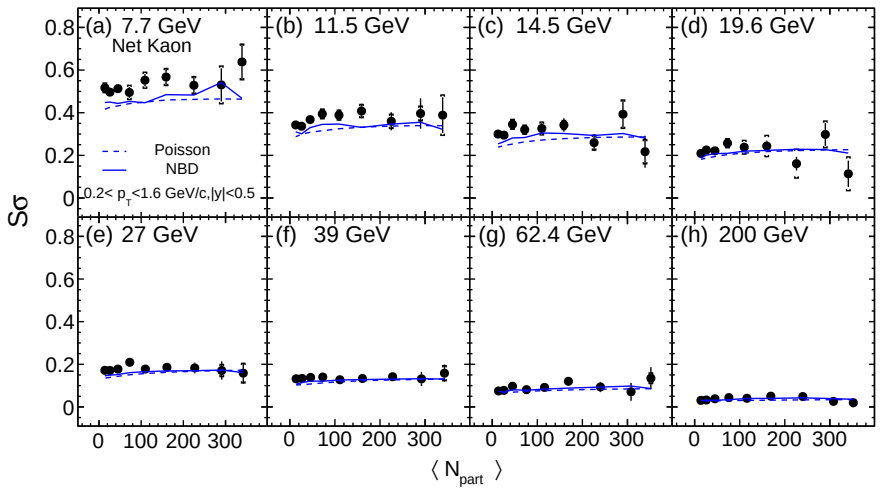

Figure 3.27: Centrality dependence of $S\sigma/$ for net-kaon multiplicity distributions in Au+Au collisions at $\sqrt{s_{NN}}$ = 7.7, 11.5, 14.5, 19.6, 27, 39, 62.4, and 200GeV. The results are corrected for the kaon reconstruction efficiency.

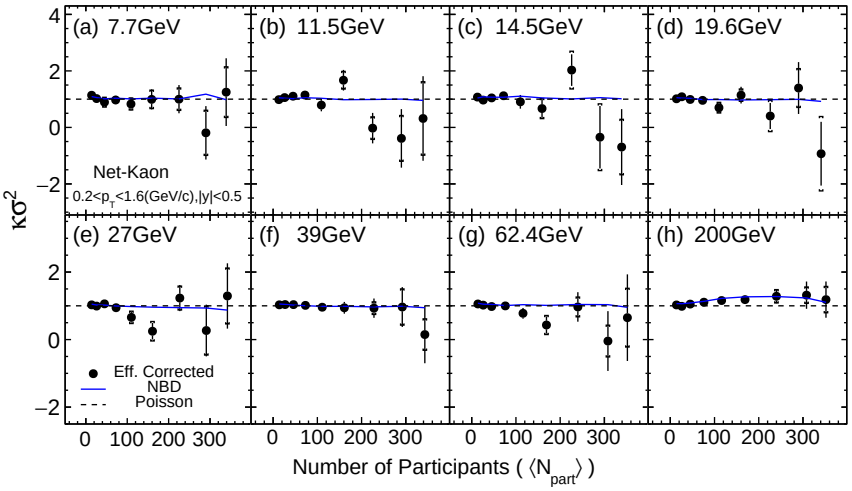

Figure 3.28: Centrality dependence of $\kappa\sigma^2$ for net-kaon multiplicity distributions in Au+Au collisions at $\sqrt{s_{NN}}$ = 7.7, 11.5, 14.5, 19.6, 27, 39, 62.4, and 200GeV. The results are corrected for the kaon reconstruction efficiency.

The ratios between different order cumulants are taken to cancel the volume term. Figures 3.26, 3.27, and 3.28 shows the $\langle N_{\rm part}\rangle$ dependence of ΔN_K distributions for cumulant ratios C_2/C_1 ($=\sigma^2/M$), C_3/C_2 ($=S\sigma$), and C_4/C_2 ($=\kappa\sigma^2$), respectively. The values of C_2/C_1, shown in figure 3.26, systematically decrease with increasing collision energy for all centralities. The Poisson baseline for C_2/C_1 slightly overestimates the data. This may indicate that there is a positive correlation between K^+ and K^-. For C_3/C_2 ($=S\sigma$), we observe that the Poisson and NBD expectations are lower than the measured $S\sigma$ values at low collision energies.The measured values for C_4/C_2 ($=\kappa\sigma^2$) are consistent with both the Poisson and NBD baselines within uncertainties.

3.9.2 Energy Dependence of Cumulant Ratios

Figure 3.29 show the energy dependence of cumulant ratios ($S\sigma$, and $\kappa\sigma^2$) for net-kaon multiplicity distributions in Au+Au collisions from UrQMD[73] and HRG calculation[24]. Form the HRG calculation of the upper panel, $S\sigma$ of net-strangeness increase with energy increase, while for net-kaon, the values are larger than net-strangeness and decrease with energy decreases. $\kappa\sigma^2$ for net-strangeness is about 1.8 while 1.1 for net-kaon. Effect from the resonance decay have negligible

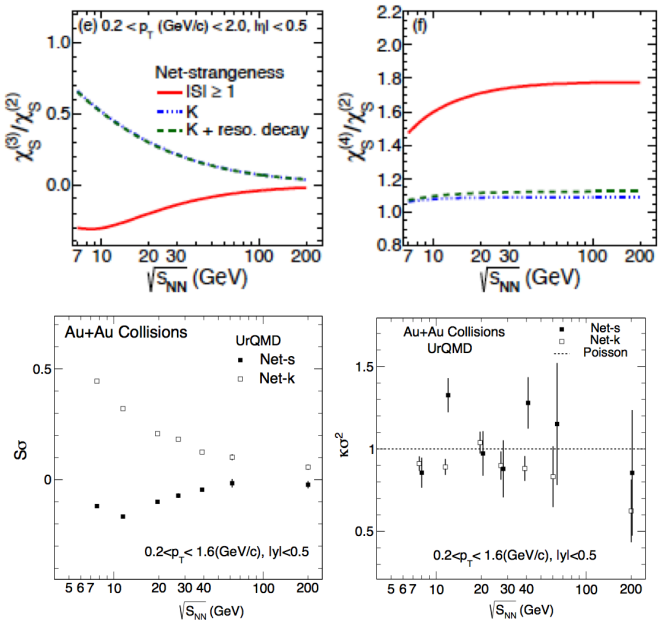

Figure 3.29: Energy dependence of cumulant ratios ($S\sigma$, and $\kappa\sigma^2$) for net-kaon multiplicity distributions in Au+Au collisions from UrQMD and HRG calculation.

effect on both $S\sigma$, and $\kappa\sigma^2$. From the lower panel of UrQMD calculation, we can see that UrQMD predictions are consistent to HRG model for $S\sigma$, and for $\kappa\sigma^2$, net-kaon results are similar to net-strangeness, within errors.

The collision energy dependence of the volume-independent cumulant ratios (C_2/C_1 ($=\sigma^2/M$), C_3/C_2 ($=S\sigma$), and C_4/C_2 ($=\kappa\sigma^2$)) for ΔN_K multiplicity distributions in Au+Au collisions are presented in Figure 3.30. The results are shown in two collision centrality bins, one corresponding to most central (0-5%) and the other to peripheral (70-80%) collisions. Results from the Poisson and NBD baselines are derived for both of the centralities. One can see that the values of σ^2/M increase as the collision energy increases, and are larger for peripheral collisions compared with the central collisions. Within uncertainties, the values of $S\sigma$ and $\kappa\sigma^2$ are consistent with both the Poisson and NBD baselines in central collisions. For peripheral collisions, both the Poisson and NBD baselines underestimate the measured $S\sigma$ values. The blue bands give the results from the UrQMD model calculations for central (0-5%) Au+Au collisions. The width of the bands represents the statistical uncertainties. The UrQMD calculations for σ^2/M, $S\sigma$, and $\kappa\sigma^2$ are consistent with the measured values within uncertainties except for σ^2/M at $\sqrt{s_{\rm NN}}$ = 200 GeV.

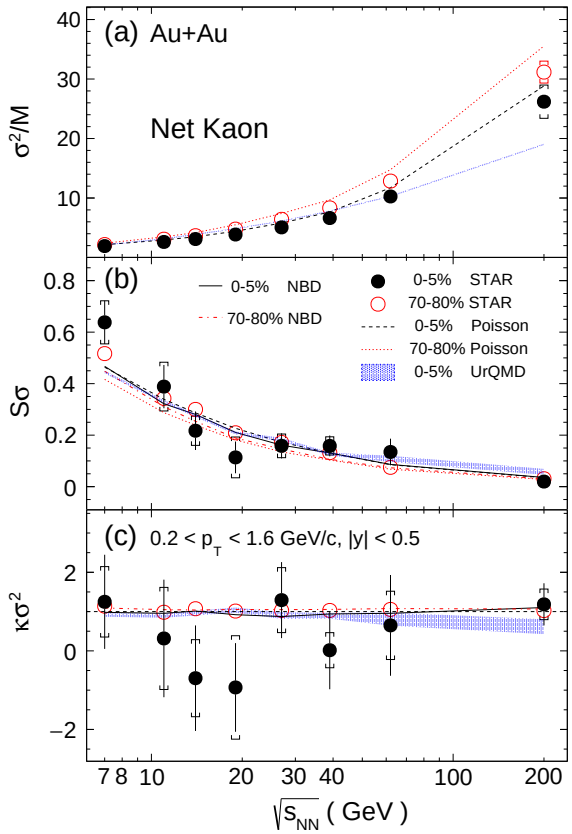

Figure 3.30: Energy dependence of cumulant ratios (σ^2/M, $S\sigma$, and $\kappa\sigma^2$) for net-kaon multiplicity distributions in Au+Au collisions at $\sqrt{s_{NN}} = 7.7$, 11.5, 14.5, 19.6, 27, 39, 62.4, and 200GeV. The Poisson expectations are denoted as dotted lines and UrQMD calculations are shown as blue bands. The error bars are statistical and caps are systematic errors.

Chapter 4

UrQM Studies And Discussion

4.1 UrQMD Model

The Ultra Relativistic Quantum Molecular Dynamics (UrQMD) is a microscopic many-body approach to study p + p, p + A, and A + A interactions at relativistic energies and is based on the covariant propagation of color strings, constituent quarks, and diquarks accompanied by mesonic and baryonic degrees of freedom. Furthermore it includes rescattering of particles, the excitation and fragmentation of color strings, and the formation and decay of hadronic resonances. UrQMD is a transport model for simulating heavy-ion collisions in the energy range from SIS to RHIC (even in LHC). It combines different reaction mechanism, and can provide theoretical simulated results of various experimental observables. It provides us the baselines and qualitative estimate on the background effects for the experimental search for the QCD phase transition and QCD critical point. The main parts of UrQMD model are: two body reaction cross section, two body potential and decay width. More details about the UrQMD model can be found in the reference [52, 53].

In this Chapter, we performed our calculations with UrQMD model in version 2.3 for Au+Au collision at $\sqrt{s_{NN}}$=7.7, 11.5, 19.6, 27, 39, 62.4, 200 GeV and the corresponding statistics are 72.5, 105, 106, 81, 133, 38, 56 million, respectively.

4.2 Results from UrQMD Model

In the UrQMD model calculations, we applied the same kinematic cuts as used in the data analysis [36, 42, 54]. The protons and anti-protons are obtained at mid-rapidity ($|y| < 0.5$) and within the transverse momentum $0.4 < p_T < 0.8$ GeV/c,

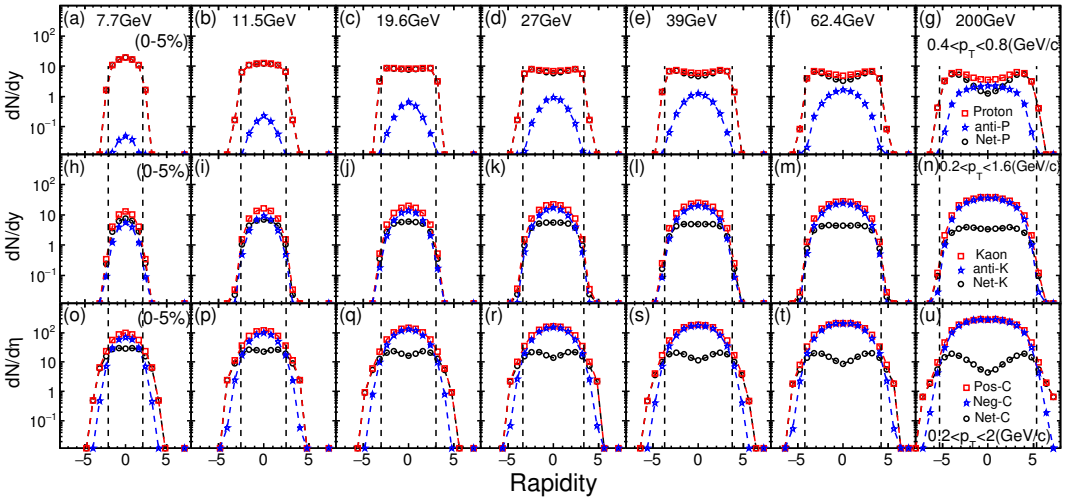

Figure 4.1: (Color online) The dN/dy distributions of net-proton, proton, anti-proton, net-kaon, K^+, K^- and $dN/d\eta$ distributions of net-charge, positive and negative charge multiplicity in Au+Au collisions at $\sqrt{s_{NN}}$ =7.7, 11.5,19.6, 27, 39, 62.4 and 200GeV for most central collision (0-5%). The vertical black dashed lines in the figure represent the beam rapidity for each energy.

the charged particles in the net-charge fluctuations are measured at pseudo-rapidity range $|\eta| < 0.5$ and within the transverse momentum $0.2 < p_T < 2$ GeV/c, and the K^+ (K^-) for net-kaon study are measured at mid-rapidity ($|y| < 0.5$) within the transverse momentum $0.2 < p_T < 1.6$ GeV/c.

Figure 4.1 shows the rapidity distributions (dN/dy) of net-proton, proton, anti-proton and net-kaon, K^+, K^-, pseudo-rapidity ($dN/d\eta$) distribution for net-charge, positive charge and negative charge particle multiplicities for the most central (0-5%) Au+Au collisions at $\sqrt{s_{NN}}$ = 7.7 to 200 GeV from UrQMD calculations. It is observed that the dN/dy distributions of net-proton and proton are nearly flat at mid-rapidity ($|y| < 0.5$). The dN/dy distribution of net-proton closely follow the distributions of proton at low energies and the values at $y = 0$ ($dN/dy|_{y=0}$) monotonically increase with decreasing energies. The anti-proton $dN/dy|_{y=0}$ show monotonically decrease with decreasing collision energies. These can be explained by the interplay between the baryon stopping and pair production of proton and anti-proton from high to low energies. The baryon stopping is stronger at low energies, while the pair production dominate the production of proton and anti-proton at high energies. For kaons, the and are mainly produced from pair production at high energies, where the number of K^+ and K^- are very similar. At low energies,

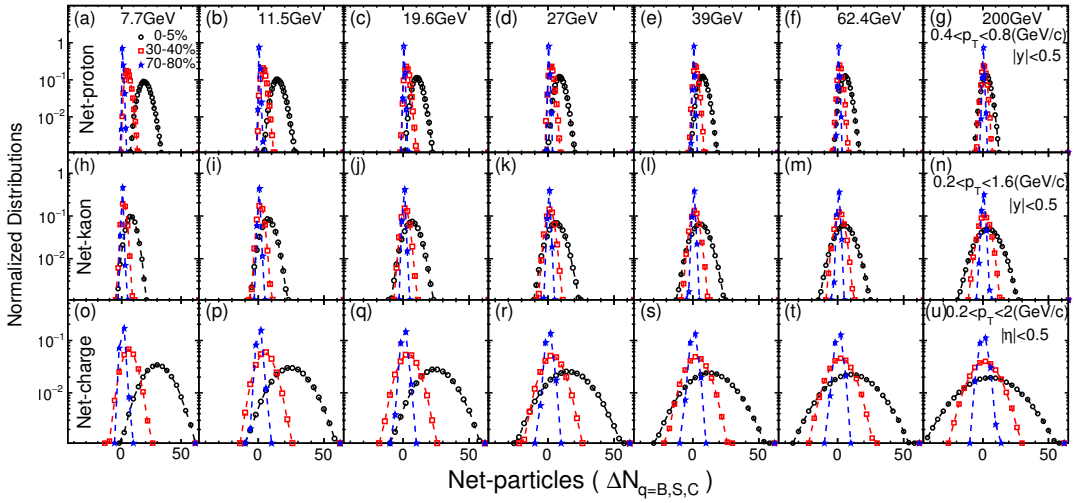

Figure 4.2: (Color online)Event-by-event distributions of net-proton, net-charge and net-kaon multiplicity distributions for Au+Au collisions at $\sqrt{s_{NN}}$ =7.7, 11.5, 19.6, 27, 39, 62.4 and 200GeV for three centrality bins(0-5%, 30-40%, 70-80%).

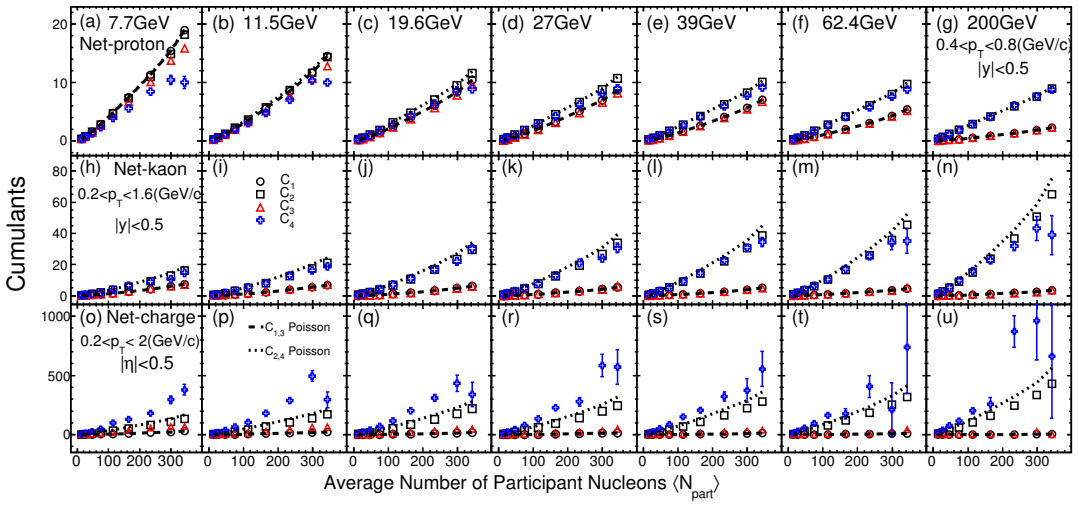

Figure 4.3: (Color online) Centrality dependenece of cumulants (C_1, C_2, C_3, C_4) of net-proton, net-kaon and net-charge multiplicity distributions for Au+Au collisions at $\sqrt{s_{NN}}$ =7.7, 11.5, 19.6, 27, 39, 62.4 and 200GeV. The dashed lines represent the Poisson expectation.

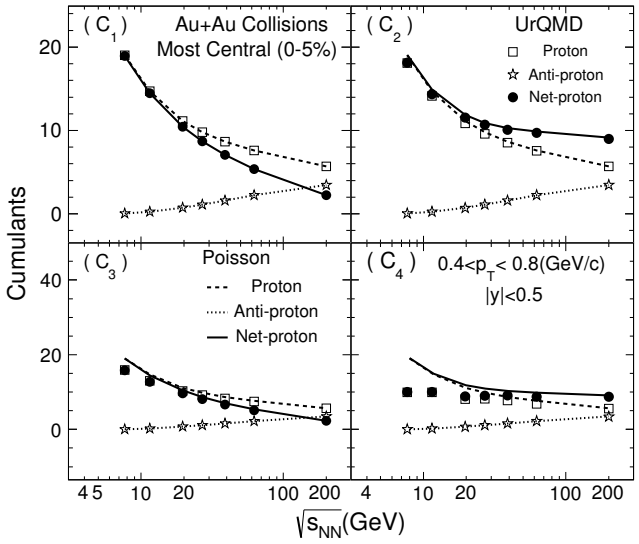

Figure 4.4: Energy dependence of cumulants of proton, anti-proton and net-proton multiplicity distribution for Au+Au collisions at $\sqrt{s_{NN}}$ =7.7, 11.5, 19.6, 27, 39, 62.4 and 200GeV for most central(0-5%). The lines represent the Poisson expectations.

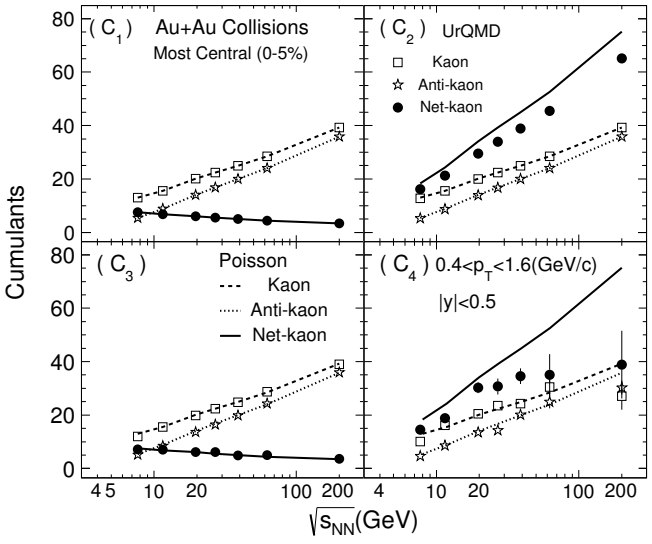

Figure 4.5: Energy dependence of cumulants of kaon, anti-kaon and net-kaon multiplicity distribution for Au+Au collisions at $\sqrt{s_{NN}}$ =7.7, 11.5, 19.6, 27, 39, 62.4 and 200GeV for most central(0-5%). The lines represent the Poisson expectations.

the associate production of the K^+ with a hyperon become more important. Due to electric charge conservation in particle production, the net-charge number will be conserved. Thus, the number of positive charge and negative charge particle multiplicity always follow closely with each other at all energies.

Figure 4.2 shows the event-by-event net-proton, net-charge and net-kaon multiplicity distributions for Au+Au collisions at $\sqrt{s_{NN}}$ =7.7∼200 GeV for three centralities (0-5%, 30-40%, 70-80%). For each energy, the mean value and the width (σ) of the net-proton, net-charge and net-kaon distributions are larger for central than peripheral collisions. For the same centrality, the mean value of net-proton, net-kaon and net-charge multiplicity distributions become larger as decreasing the collision energy. The width of the net-kaon and net-charge multiplicity distributions decrease with decreasing the collision energy while the net-proton distribution shows opposite trend. The width of the net-charge distributions are much larger than the net-proton and net-kaon distribution. Based on the Delta theorem [55, 56], the statistical errors of various cumulants are proportional to the different power of σ value of the distributions. Thus, the cumulant of net-charge multiplicity distributions are with larger statistical errors than the net-proton and net-kaon cumulants with the same number of events. On the other hand, the volume fluctuations originated from the finite centrality bin width and initial volume (geometry) fluctuations of the colliding nuclei [57] will enhance the fluctuation measurements. The raw multiplicity distributions of net-proton, net-charge and net-kaon shown in Fig.4.2 should not be directly used to calculate the various cumulants and one needs to apply so called centrality bin width correction[57] to address the effects of the volume fluctuations in a wide centrality bin.

Figure 4.3 shows the centrality dependence of cumulants (up to fourth order) of net-proton, net-charge and net-kaon multiplicity distributions in Au+Au collisions at $\sqrt{s_{NN}}$ =7.7∼200 GeV. In general, those cumulants show a linear variation with the averaged number of participant nucleons, which can be understood as the additivity property of the cumulants by increasing the volume of the system. The odd order cumulants (C_1 and C_3) and the even order cumulants (C_2 and C_4) are separated into two groups as the C_1 and C_2 values are closely follow the C_3 and C_4, respectively. If the multiplicity distributions of particles and anti-particles are independent Poissonian, the corresponding net-particle cumulants can be simply

constructed from the mean values as

$$C_n(N^+ - N^-) = C_1(N^+) + (-1)^n C_1(N^-) \tag{4.1}$$

where $C_1(N^+)$ denotes the mean value of proton, K^+ and positive charge particle distributions, $C_1(N^-)$ represents the mean value of anti-proton, K^- and negative charge particle, respectively. The separation gets smaller when the energy decreases because of the reduction of number of anti-proton and K^- produced from pair production at low energies.

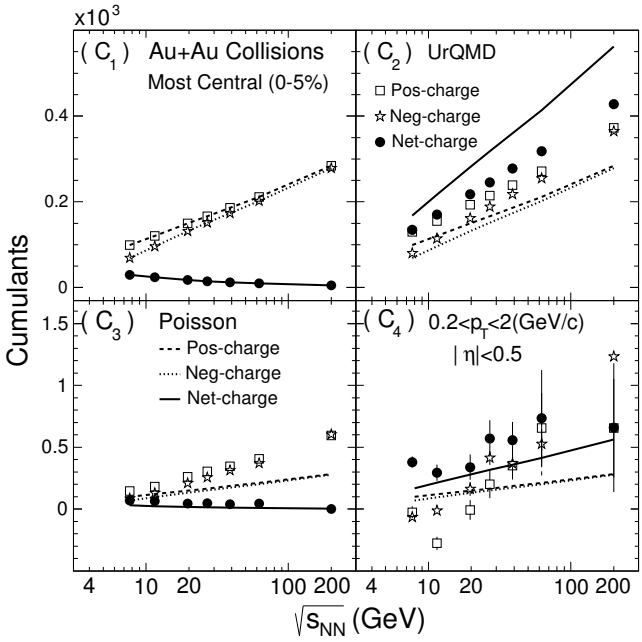

Figure 4.6: Energy dependence of various cumulants of positive charge, negative charge and net-charge multiplicity distribution for Au+Au collisions at $\sqrt{s_{NN}}$ =7.7, 11.5, 19.6, 27, 39, 62.4 and 200GeV for most central(0-5%). The lines represent the Poisson expectations.

Figure 4.4 shows energy dependence of cumulants ($C_1 \sim C_4$) of proton, anti-proton and net-proton multiplicity distributions for the most central(0-5%) Au+Au collisions at $\sqrt{s_{NN}}$ =7.7 to 200 GeV. The cumulants of net-proton and proton distribution monotonically increase when energy decreases, while the cumulants of anti-proton distribution show decreasing trends. The net-proton cumulants follow closely with the proton cumulants at low energies. Those can be understood by the

interplay between baryon stopping and pair production at different energies. The anti-proton cumulants ($C_1 \sim C_4$) can be well described by the Poisson expectations, while large deviations from Poisson expectations are observed for the C_3 and C_4 of net-proton and proton multiplicity distributions, especially for the low energies. Figure4.5 shows the energy dependence of cumulants of the net-kaon, K^+ and K^- distributions. The mean value of K^+ distributions decrease with decreasing energies, which is different from proton cumulants shown in Fig.4.4. At low energies, baryon stopping dominated the production of protons at mid-rapidity. However, the K^+ and K^- are produced particles and the pair production is the main production mechanism, which leads to the monotonically increase of the yields when the collision energy increases. Furthermore, the odd order cumulants (C_1 and C_3) and the even order cumulants (C_2 and C_4) of net-kaon distributions shows opposite energy dependence trend. Those can be explained qualitatively in terms of the Poisson expectations of the cumulants in Eq. 4.1 and the energy dependence of the associate and pair production mechanism for the K^+ and K^-. When the energy increases, the pair production become more important and the yields of K^+ and K^- increase with increasing energy. That's why the even order cumulants (C_2 and C_4) of net-kaon distributions show monotonically increase trends. On the other hand, associate production of K^+ will increase when the energy decrease. The cumulants of net-charge, positive and negative charge multiplicity distributions are shown in Fig. 4.6. The energy dependence trends in Fig. 4.6 are similar in Fig. 4.5, since most of the charged particles (e.g. kaon and pion) are directly produced. The deviations from the Poisson expectations begin to show up at second order cumulants (C_2). It indicates a strong correlation between the positive and negative charged particles in heavy-ion collisions. The errors of forth order cumulant are very large for net-charge multiplicity distributions due to the wide distributions.

4.3 Comparisons Between STAR Data and UrQMD Model

The STAR Collaboration has published the centrality and energy dependence of the moments of net-proton and net-charge multiplicity distributions for Au+Au collision at $\sqrt{s_{NN}}$=7.7, 11.5, 19.6, 27, 39, 62.4, 200 GeV [36, 42]. Those data are taken from the first phase of RHIC BES program in the years 2010 and 2011

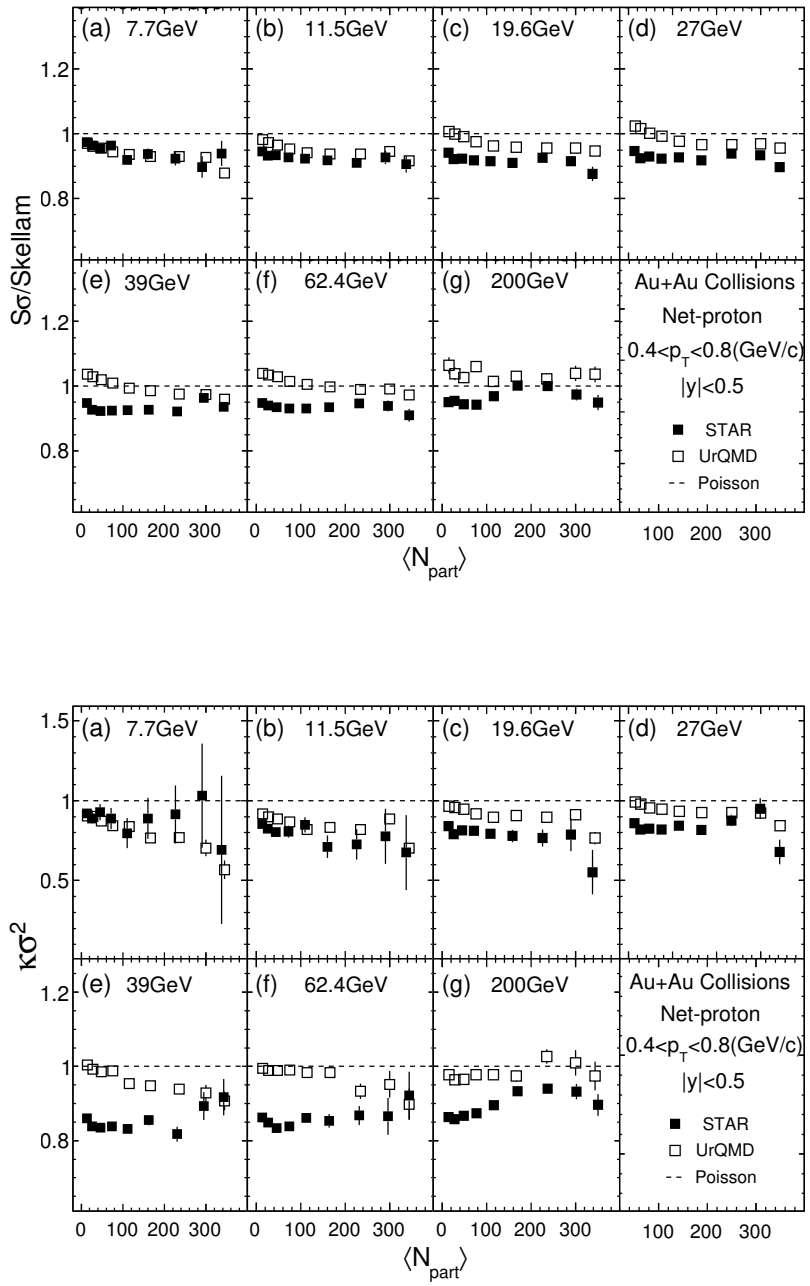

Figure 4.7: Centrality dependence of the cumulant ratios($S\sigma$, $\kappa\sigma^2$) of net-proton multiplicity distributions for Au+Au collision at $\sqrt{s_{NN}}$ =7.7 to 200 GeV. The solid markers represent the results from STAR measurement, the open markers represent results from UrQMD calculation.The dashed lines denote the Poisson expectations for the STAR data.

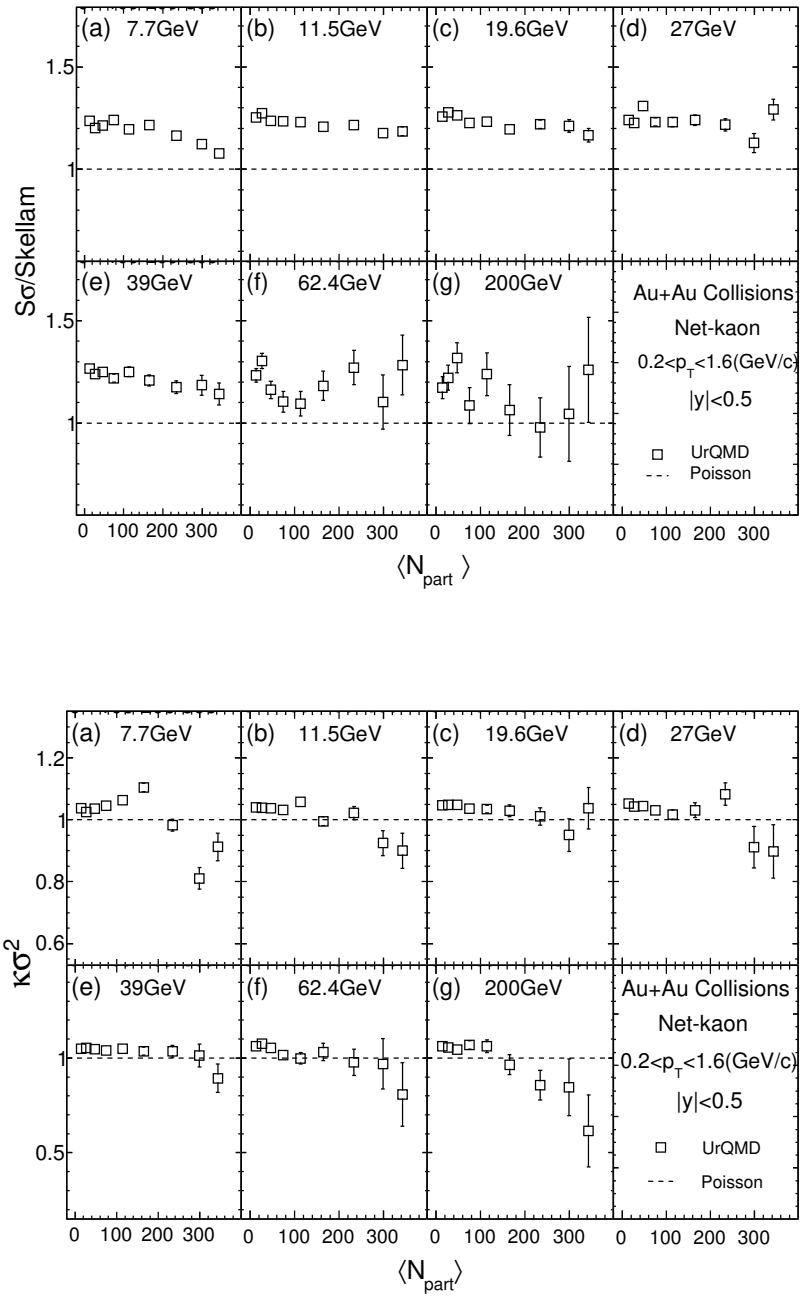

Figure 4.8: Centrality dependence of the cumulant ratios($S\sigma$, $\kappa\sigma^2$) of net-kaon multiplicity distributions for Au+Au collision at $\sqrt{s_{NN}}$ =7.7 to 200 GeV. The solid markers represent the results from STAR measurement, the open markers represent results from UrQMD calculation.

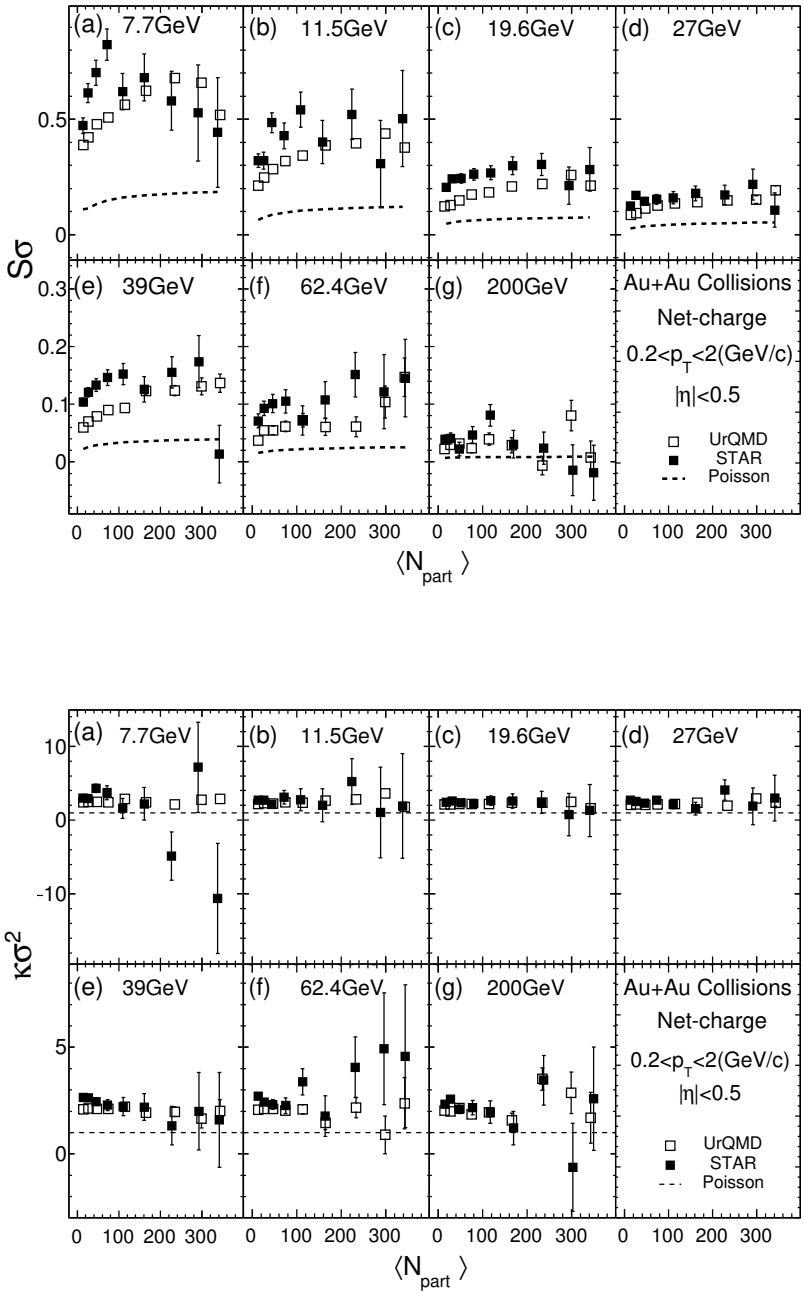

Figure 4.9: Centrality dependence of the cumulant ratios($S\sigma$, $\kappa\sigma^2$) of net-charge multiplicity distributions for Au+Au collision at $\sqrt{s_{NN}}$ =7.7 to 200 GeV. The solid markers represent the results from STAR measurement, the open markers stand for the results from UrQMD calculation. The dashed lines denote the Poisson expectations for the STAR data.

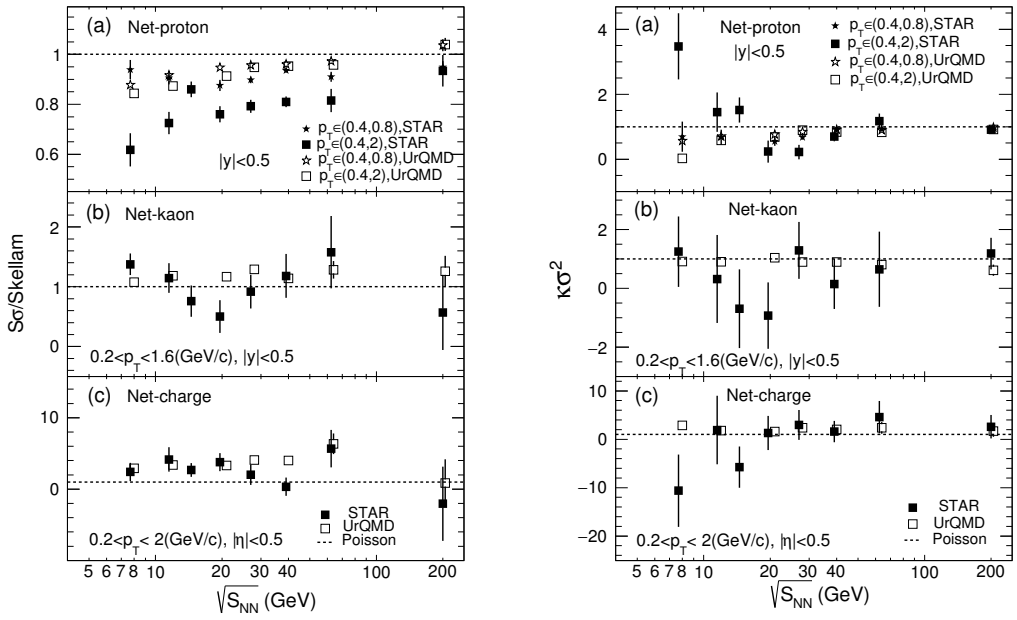

Figure 4.10: Energy dependence of cumulant ratios($S\sigma$, $\kappa\sigma^2$) of net-proton, net-charge and net-kaon multipliity distributions for Au+Au collision at $\sqrt{s_{NN}}$ =7.7 to 200 GeV. The solid markers represent the results from STAR measurement, the open markers represent results from UrQMD calculation. The dashed lines denote the Poisson expectations for the STAR data.

[58]. Recently, the new net-proton and net-kaon results have been presented in CPOD2014 [59] and QM2015 conference, respectively [60, 61]. The net-proton fluctuation measurement $\kappa\sigma^2$ of most central Au+Au collisions clearly show non-monotonic energy dependence after extending the transverse momentum (p_T) coverage of proton and anti-proton from 0.4 $\sim$ 0.8 to 0.4 $\sim$ 2 GeV/c. The acceptance dependence of the fluctuation measurements have been discussed by the theoretical calculations in terms of critical contribution and the thermal blurring/diffusion effects in heavy-ion collisions[62, 63]. In the following, we will make a comparison for the cumulant ratios ($S\sigma$ and $\kappa\sigma^2$) of the net-proton, net-charge and net-kaon distributions between the STAR data and UrQMD calculations.

Experimentally, the volume independent cumulant ratios ($C_3/C_2 = S\sigma$, $C_4/C_2 = \kappa\sigma^2$) are constructed to be the main observables to search for the QCD critical point. Fig. 4.7 shows the centrality dependence of $S\sigma$/Skellam and $\kappa\sigma^2$ of net-proton multiplicity distributions for Au+Au collisions from $\sqrt{s_{NN}}$=‘7.7 to 200GeV.

Based on the Eq. 4.1, the Skellam (Poisson) baseline for net-proton $S\sigma$ is constructed from the mean value of the proton ($< N_p >$) and anti-proton ($< N_{\bar{p}} >$)

number as $(< N_p > - < N_{\bar{p}} >)/(< N_p > + < N_{\bar{p}} >)$. For $S\sigma$/Skellam and $\kappa\sigma^2$, the UrQMD results follow closely with the STAR measurements at 7.7 and 11.5 GeV whereas the experimental results show larger deviation from the Poisson baselines than the model results.The large statistical error bars of the STAR data in $\kappa\sigma^2$ of 0-5% most central collisions at $\sqrt{s_{NN}}$=7.7 and 11.5 GeV can be reduced by a factor of 3 $\sim$ 4 in the second phase of the RHIC beam energy scan (2019-2020). In the fig. 4.8, since the centrality dependence of net-kaon cumulant ratios from BES energies is not public yet, we only show the results from the UrQMD model calculations. It is observed that the $S\sigma$/Skellam values are always above unity, which means $S\sigma$ values are larger than Poisson baselines. The net-kaon $\kappa\sigma^2$ from UrQMD calculations are close to unity. Figure 4.9 shows the centrality dependence of cumulants ratios ($S\sigma$, $\kappa\sigma^2$) of net-charge multiplicity distributions. The $S\sigma$ from UrQMD calculations are in general smaller than the STAR data, which show large deviation from the Poisson expectation at low energies. For net-charge $\kappa\sigma^2$, the STAR results can be well described by the UrQMD results, however the experimental results are with large statistical errors.

Figure 4.10 shows the energy dependence of cumulant ratios ($S\sigma, \kappa\sigma^2$) of net-proton, net-charge and net-kaon multiplicity distributions of the 0-5% most central Au+Au collisions at RHIC BES energies from the STAR experiments and UrQMD calculations. The $S\sigma$ values have been scaled by the Skellam (Poisson) baselines. Within statistical uncertainties, the net-charge and net-kaon results has weak energy dependence and are close to Skellam (Poisson) baselines. Both of the net-charge and net-kaon $S\sigma, \kappa\sigma^2$ measured by STAR experiment can be well described by the UrQMD model. On the other hand, the STAR experiment has measured the high order net-proton fluctuations for the two transverse momentum (p_T) coverages 0.4 $\sim$ 0.8 GeV/c and 0.4 $\sim$ 2 GeV/c, respectively. For the net-proton $S\sigma$/Skellam, both the UrQMD results and STAR data show monotonic decreasing trends as the collision energy decreases. For net-proton $\kappa\sigma^2$ with the small p_T coverage 0.4 $\sim$ 0.8 GeV/c, the STAR data show large deviations from unity below $\sqrt{s_{NN}}$ = 39 GeV, especially at 19.6 and 27 GeV. The statistical errors of the data at 7.7 and 11.5 GeV are much larger than higher energies due to the limited statistics. For wider p_T coverage 0.4 $\sim$ 2 GeV/c, we observe a clear non-monotonic energy dependence for the net-proton $\kappa\sigma^2$ with a minimum around 19.6 GeV, then become above unity in the energies below 19.6 GeV. However, the UrQMD model without implementing

the critical point physics, failed to describe the STAR data especially for large p_T coverage 0.4 $\sim$ 2 GeV/c case and low collision energies. The monotonic decrease when decreasing energies and strong suppression below unity at low energies are consistent with the effects of the baryon number conservations.

4.4 Summary

Experimentally, fluctuations of conserved quantities have been applied to probe the signature of the QCD phase transition and critical point in heavy-ion collisions. To understand the non-critical contributions to the observables, we have performed detailed model calculations. In this paper, we present the centrality and energy dependence of the cumulants (C_1, C_2, C_3, C_4) and their ratios ($C_3/C_2 = S\sigma, C_4/C_2 = \kappa\sigma^2$) of net-proton, net-charge and net-kaon multiplicity distributions with UrQMD model for Au+Au collision at $\sqrt{s_{NN}}$=7.7, 11.5, 19.6, 27, 39, 62.4 and 200 GeV. It has been found that the production mechanism of the proton and kaon have a significant impact on the fluctuations of net-particles. For e.g, the interplay of the baryon stopping-pair production of proton and anti-proton, and the associate-pair production of the K^+ and K^- at different energies. At low energies, the baryon stopping of protons and associate production of kaons play an important roles. This will lead to big difference between the fluctuations of proton, anti-proton numbers and fluctuations of K^+, K^-. Finally, the comparisons for the cumulant ratios ($S\sigma$, $\kappa\sigma^2$) of net-proton, net-charge and net-kaon multiplicity distributions has been made between the STAR data and the UrQMD calculations. Within the uncertainties, the net-charge and net-kaon fluctuations measured by STAR experiment can be described by the UrQMD results. For the net-proton fluctuations, the STAR measured $\kappa\sigma^2$ at the 0-5% most central Au+Au collisions show a clear non-monotonic energy dependence with a minimum around 20 GeV. This non-monotonic behavior can not be described by the UrQMD model, in which there has no critical physics implemented. The large suppression of the net-proton fluctuations at low energies could be explained by the effects of baryon number conservations. Since the UrQMD model are blind to the critical phenomena in the heavy ion collision, the results from UrQMD calculations can provide us non-CP physics baselines and a qualitatively estimation for the background contributions to the QCD critical point search in heavy-ion collisions by using the fluctuations of the net-proton, net-charge

and net-kaon numbers.

Chapter 5

Event Plane Detector

5.1 Introduction

The RHIC Beam Energy Scan (BES) program has been identified as a top priority by Brookhaven Lab. STAR detector, which built for multi-purpose, correlated studies with broad acceptance, is an existing detector likewise ideal for BES. The EPD is a new detector dedicated to event plane, centrality, and trigger Detector (EPD) in the forward direction of STAR for the Beam Energy Scan (BES) phase II. The new detector will cover the pseudo-rapidity range between 2.1 and 5.1, with high radial and azimuthal segmentation. The EPD will allow the centrality and the event plane to be measured in the forward region, reducing the systematics due to autocorrelations from mid-rapidity analyses. The baseline detector design utilizes scintillator plastic, wavelength-shifting fibers and silicon photomultipliers (SiPMs). The EPD consists of two disks that will be placed on either side of the STAR interaction region, in the current location of the Beam-Beam Counter (BBC). We installed 1/4 of one of the disks for run 17. The remaining 7/8 of the detector will be built and installed for run 18. The EPD serves several purposes which including the event plane, centrality, and trigger.

5.2 Physics of the EPD

The directed flow is expected to be especially sensitive to the early evolution of a heavy-ion collision. Three-fluid hydrodynamic models with an explicit first-order phase transition in the equation of state predict a dip in the slope of the (net)proton v_1 at mid-rapidity [74–76]. This non-monotonic behavior is not seen in transport models, such as UrQMD [77, 52], nor is it seen in hybrid[78] or PHSD[79]

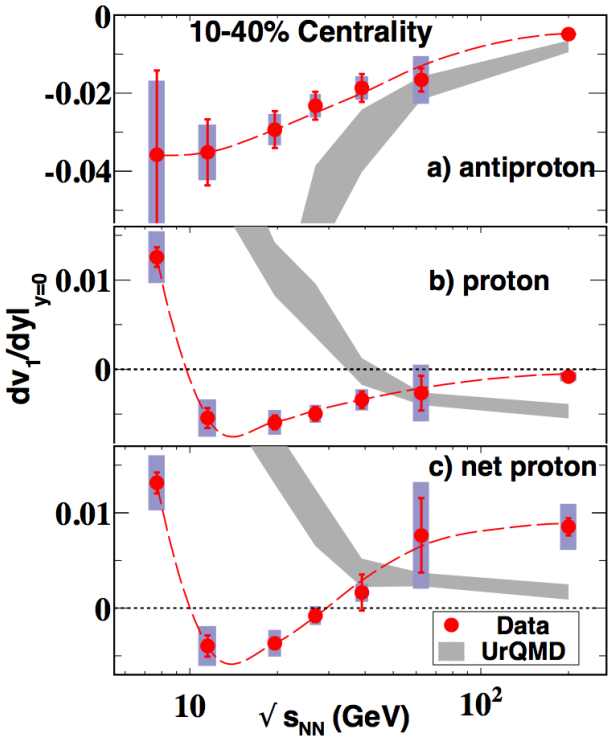

Figure 5.1: Directed flow slope (dv_1/dy) versus the beam energy at mid-rapidity for protons, ant-protons, and net protons, respectively, along with UrQMD calculations subject to the same cuts and fit conditions. Plot taken from [80]

calculations. A double sign change in the mid-rapidity net-proton v1 slope is seen in the STAR BES for mid-central (10-40%) collisions (Figure 5.1)[80]. Net-protons are used as a proxy of transported particles pushed to mid-rapidity, as anti-protons may only be produced. v_1 results require forward instrumentation to measure the first order event plane. For 7.7GeV to 39GeV, this analysis is performed using the BBC, while at 62.4GeV and 200GeV the ZDC is used. A detector, such as the EPD, with high η segmentation increases our understanding of this dependence. More obviously high segmentation in ϕ reduces statistical error by providing a better event-plane resolution. The statistical error here scales as $1/(R_1 * \sqrt{N})$, where R_1 is the first order event plane resolution. Error reductions from increased EPD R_1 and BES II statistics allow for a more finely centrality binned analysis which will lead to better understanding of the relevance of baryon stopping at low beam energies.

Fluctuation studies in BES-II require the EPD not for determination of the

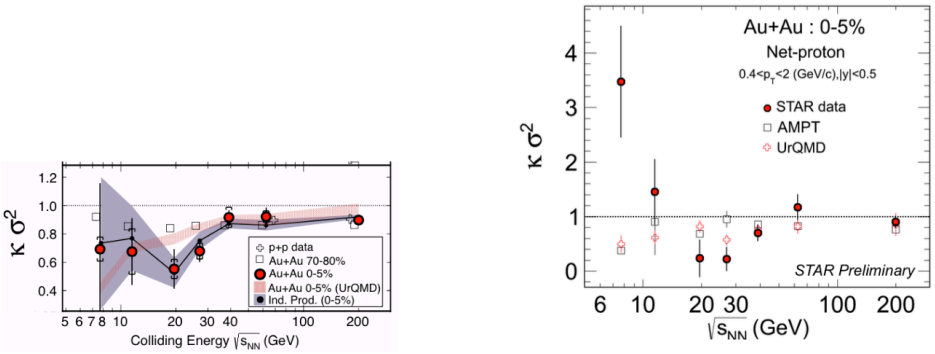

Figure 5.2: The product of 4th and 2nd moments of the net proton distribution from central collisions depends on $\sqrt{s_{NN}}$in a non-trivial. Left: The published values from STAR's 2014 PRL [36]. Right: Preliminary STAR data presented at CPOD 2014[81].

event plane, but rather for centrality determination in a region well separated (in rapidity) from the mid rapidity region under study. Others, such as forward-backward correlations and balance functions, require the extended rapidity coverage as part of the analysis itself. STAR has published results on the moments of conserved quantities in QCD–net electrical charge[42], net strangeness (restricted to kaons)[54], and net baryon number (restricted to protons)[36, 81]. The measurement of higher-order moments of the net proton distributions have attracted the most attention, as they display an energy dependence that is predicted for a system near a critical point. Of key focus is the product of the fourth to the second moment of the net-proton distribution, which is expected to evolve from above unity (super-Poissonian) to below unity, and then return to unity, as the energy of the collision increases. STAR's results, which have attracted intense attention, are shown in Figure 5.2.

The iTPC upgrade for BES-II is partly motivated by the need to widen the rapidity range of the net-proton analysis. As discussed above, a determination of event centrality at forward rapidity will be crucial to make a compelling and lasting message from this intriguing data. The EPD will be crucial. The net-proton kurtosis analysis uses for centrality estimation the charged-particle multiplicity at $|\eta| < 1.0$ –overlapping the same region ($|y| < 0.5$) from which the analyzed protons and antiprotons are drawn – excluding the protons and antiprotons themselves. This is hardly ideal. After all, pions make up the bulk of the midrapidity charged particles, and most of these arise from midrapidity *delta* baryons, especially at low $\sqrt{s_{NN}}$. The other decay product of a midrapidity $\sqrt{s_{NN}}$ is a midrapidity proton.

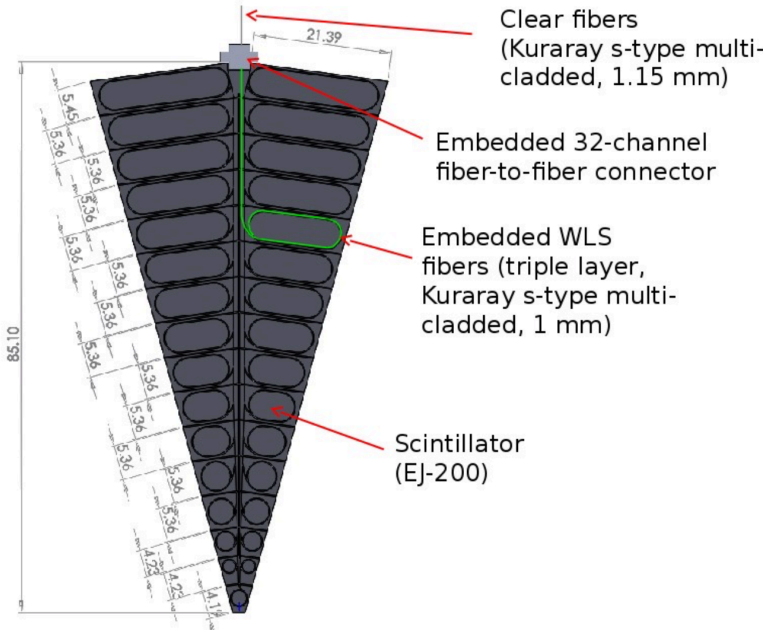

Figure 5.3: Super sector consists of two sectors divided into 31 separate tiles. Fibers will be routed in central grooves to outer edge connector.

A separation of at least one unit of rapidity between the region used for the proton analysis, and the region used for centrality estimation, is absolutely required if STAR's intriguing but somewhat unstable fluctuations signals will result in a convincing and lasting message of the RHIC BES program.

5.3 EPD Overview

The EPD will be the the same size as the Beam-Beam Counter (BBC), as it is required to sit in the same space within the STAR experiment, which gives is the same acceptance in $\eta - \phi$. The EPD will extend from a radius of 4.5 cm (1.77 in) to 90 cm (35.4 in) and will be located at $z = \pm 375$ cm, which corresponds to $5.1 < \eta < 2.1$. The design allows for the EPD to be installed behind the BBC, or for the EPD to be installed instead of the BBC. The EPD scintillator is 1.2 cm thick, the same thickness as the BBC.

The EPD will have 24 azimuthal segments, spanning an angle of 15° which we named as "sector". A super sector will contain two sectors and will be machined out of a single piece of scintillator, the outer dimensions are shown in Figure 5.3. There will be 16 segments radially, however the innermost tile will span an entire

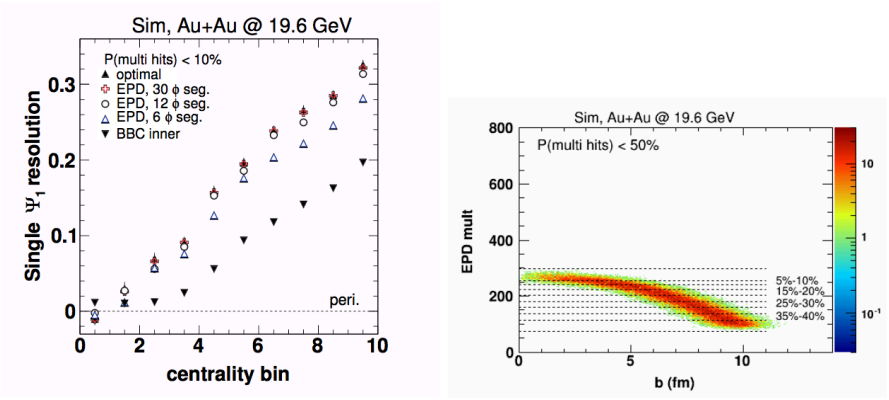

Figure 5.4: Left figure: 1 (single plane) event plane resolution as a function of centrality for different detector setups. Right figure: Multiplicity in the EPD acceptance as a function of the impact parameter b for multiple hits.

super sector. Each tile other than the innermost will span 15°, and the innermost tile will spans the full 30°of the super sector. The EPD is designed such that the probability of multiple particle hits in the same tile would be less than 10%. This increases to 65% for the top energy of 200 GeV with the same segmentation.

5.3.1 Centrality Resolution

Figure 5.4 shows the hit count versus the impact parameter, which drives the centrality resolution of the detector. For this plot, it was assumed that multiple hits could not be distinguished, which decreases the centrality resolution. The prototype data has shown us that while it is not possible to distinguish individual hits, we can use ADC weighting to better determine the centrality.

5.3.2 Event Plane Resolution

Figure 5.4 shows the event plane resolutions for different detector setups as a function of the centrality bin. The resolution for all configurations chosen is better than the BBC resolution. Above 12 sectors the gain in the event plan resolution is minimal for the first order event plane. However, a higher segmentation is needed for good higher order event plane resolution. For the first through 5th order plane, the resolution starts to saturate around 20 segments, which brings us to our choice of 24.

The Beam-Beam Counter (BBC) had been used as the trigger detector for the first Beam Energy Scan. The inner tiles of the BBC cover an area of $3.3 < \eta < 5.0$ and it has a timing resolution of 1 ns. For the EPD to replace this BBC, it has to perform at least this well, and given the requirements of the BES-II program it will be to be an improvement. In order to have high effciency for peripheral events at least 12 radial segments are needed for triggering. The EPD TACs need to be spread evenly in azimuth to reduce the systematic uncertainty.

5.3.3 Technology

The fibers used in the scintillator tiles for signal collection are Kuraray Y-11(200) Wavelength Shifting Fibers (WLS). These fibers have an attenuation length of $\lambda = 400$ cm. In order to transmit as much light as possible the fibers need to have polished ends cut perpendicular to the fibers'longitudinal axes.

Based on the physics requirements and the area to be covered, we uses a combination of scintillators and silicon photomultipliers (SiPM) for the detector. This combination is the most promising technology choice. Commercial SiPM technology as a replacement for standard photomultipliers (PMT) has been used for high energy experiments from 2005 to present day[82, 83]. Tests show a similar or even better performance compared to standard PMTs. Many experiments are currently planning upgrades using SiPM technology, e.g. the CMS HCAL upgrade for the high luminosity runs[84].

After polishing, the end of the WLS that will be embedded in the scintillator was painted with Eljen EJ-510 reflective paint in order to reflect back photons that were heading in the "wrong" direction. Additionally, the edges of the scintillator itself was polished with aluminum oxide powder in order to increase its reflectivity. Then the fibers were glued into the grooves of the scintillator using Eljen EJ-500 optical cement for good optical contact. In order to further ensure that signal photons were contained within the plastic scintillator, all tiles were tightly wrapped with aluminized mylar and then again with thick black paper. We found that it wasn't suffcient to simply take a piece of mylar and hand-wrap it around the tiles because the result isn't nearly tight enough. Instead, we drew a template cut for the mylar that would minimize the total surface area of the mylar while completely covering all faces of the tile. The mylar was then laid over the template and cut out with a box cutter for each tile. Any piece of the mylar that would be a fold

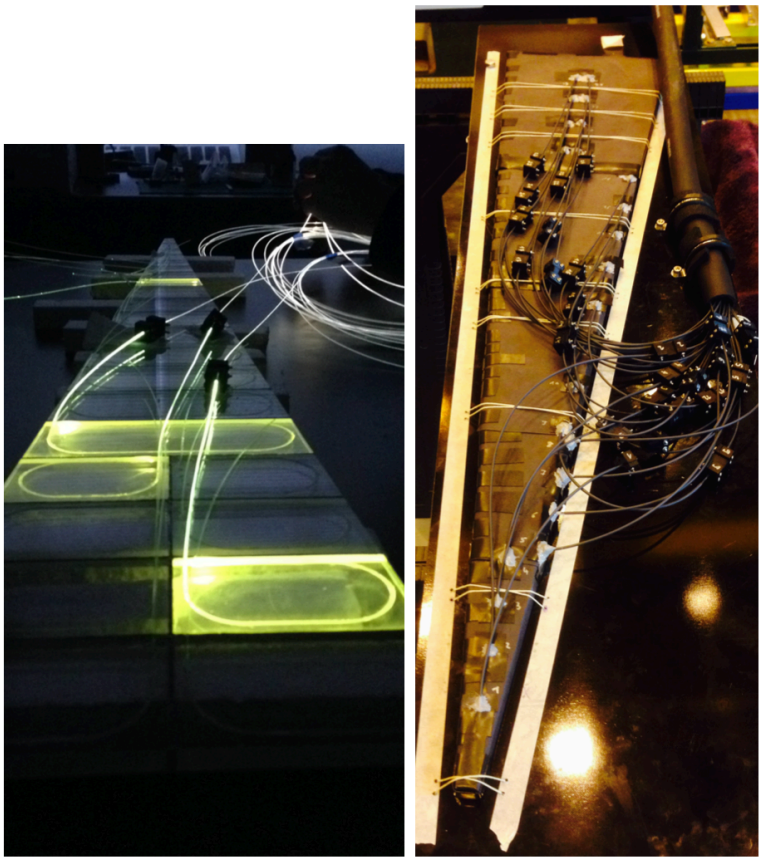

Figure 5.5: On the left is the light test done for the assembled prototype, where light was shined into the fiber optics. On the right is the finished EPD prototype.

on the tile was also perforated somewhat so as to ensure sharp edges all around. The result for test tiles is shown in Figure 5.5, though for this black tape was used instead of black paper.

The far end of each clear optical fiber was connected to a SiPM. These were then connected to the QT Boards that were borrowed from the FPS project for our use. The electronics box was designed for Ultra Low Density (ULD) in order to facilitate any interventions that would be needed.

5.3.4 Prototype Results and Dark Noise

The average number of photoelectrons that we detect for an MIP, is what we are most interested in finding out. This was measured to be around 40 in the lab, which is in good agreement with the fit value of 42 which was determined by a fit of

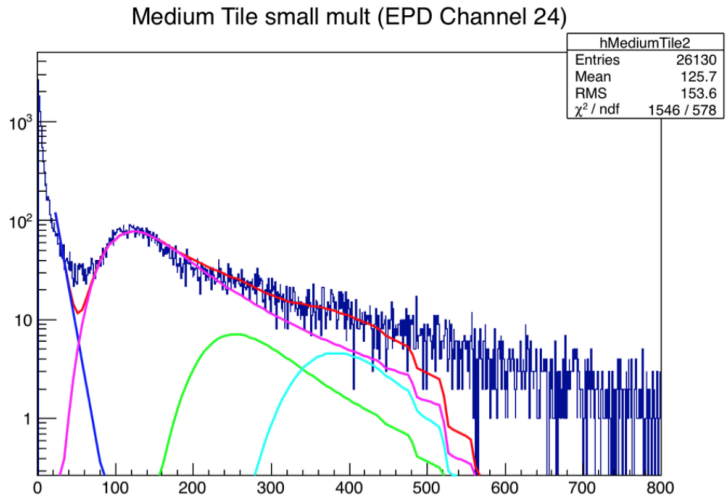

Figure 5.6: The ADC spectrum for channel 24.

the ADC spectrum from channel 42 as shown in Figure 5.6. It's in good agreement with the lab studies that have been done.

Signals of bare SiPMs, not connected to any detector, were measured in the lab to get the energy information for single fired pixels. Figure 5.7 shows the dark noise signals on the scope (top) and the integrated signals (bottom). The integrated double and triple signals scale as expected. This gives an estimate for the signals of single, double and triple photons. We divided the average signal of a triple WLS layer, 1cm scintillator tile design by the integrated single dark noise signal and get 250 photoelectrons/MIP. The prototype has only a single WLS fiber loop, which reduced the light output by about a factor of 2. The coupling to clear fibers for the prototype has an efficiency of 0.6. The attenuation due to WLS fibers (0.4 m attenuation length) and clear fibers (10 m attenuation length) is 0.5. All factors together result in an estimated number of 40 photoelectrons/MIP for the prototype. For the EPD we are going to use the S13360-1325PE type SiPMs with a pixel pitch of 25m and clear fibers with 1.15 mm diameter. That results in about 1600 pixels on the fiber area. The coupling efficiency is assumed to be at least 80%, the attenuation for WLS and clear fiber is 0.5, which results in about 100 photoelectrons/MIP. That means at maximum 16 MIPs can be detected in the extreme case.

During the measurement the trigger level for all three tiles was set to 6.0 mV and 1000 events were recorded. Any channel voltage larger than 6.0 mV was considered the start of a good signal and the time was recorded for the three readout

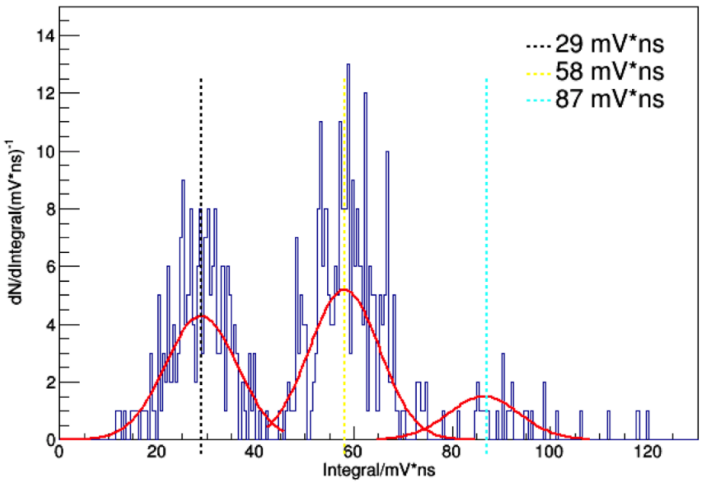

Figure 5.7: Top: Dark noise of the SiPMs, showing single, double and triple pixel signals. Bottom: Integrated dark noise signals, showing the peaks for single, double and triple pixels.

channels as T_1, T_2 and T_3 respectively.

The distribution of the time difference is shown in figure 5.8. The time difference distributions for $T_1 - T_3$ and $T_2 - T_3$ are similar and therefore only the distribution for $T_1 - T_3$ is shown. The distributions were fit with a gaussian and the sigma value was recorded as 0.99 ns. For the trigger reference we calculated the distribution for $T_1 - T_2$, which was similar to the other distributions.

The timing resolution is calculated as $\sigma/\sqrt{2} = 700$ for the triple layer fiber test tile. A second set of measurements was taken with the same setup and parameters for a test tile with only a single layer WLS fiber in an embedded sigma shape. For this second measurement $\sigma = 0.95 \pm 0.02$ ns and the timing resolution is calculated to be 670 ps. This shows that there is no significant difference between the single layered tile and the triple layered tile in terms of timing resolution. The timing resolution for the BBC detector is on the order of 1.0 ns, which is significantly higher than the projected resolution of the EPD. In conclusion, the EPD can successfully replace the BBC as a trigger detector.

5.3.5 The Final EPD Design

The final design for the EPD consists of two disks (wheels) made of 1.2 cm thick Eljen EJ-200 plastic scintillator with an inner radius of 4.5 cm and an outer radius of 90 cm. Each disk will be composed of 24 sectors, for a total of 48 sectors. A super

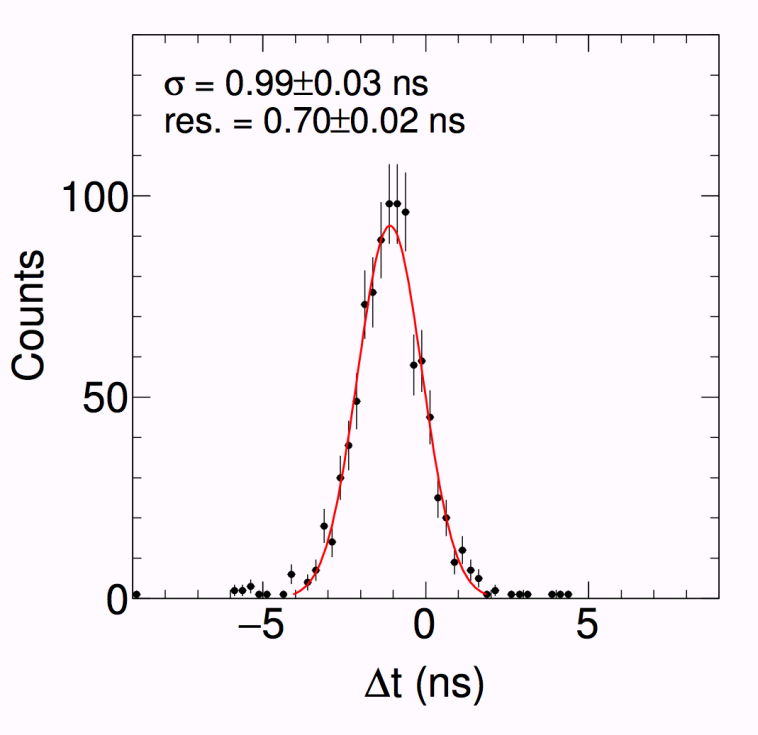

Figure 5.8: The gaussian distribution of the time difference between the test tile and trigger 1 ($T_1 - T_3$) from which the timing resolution of the EPD is calculated.

sector will consist of two sectors, for a total of 12 super sectors per wheel. Each super sector will be divided into 31 separate tiles. The inner-most tile, extending from a radius of 4.5 to 8.5 cm, will span the entire super sector. All subsequent tiles will only span a sector.

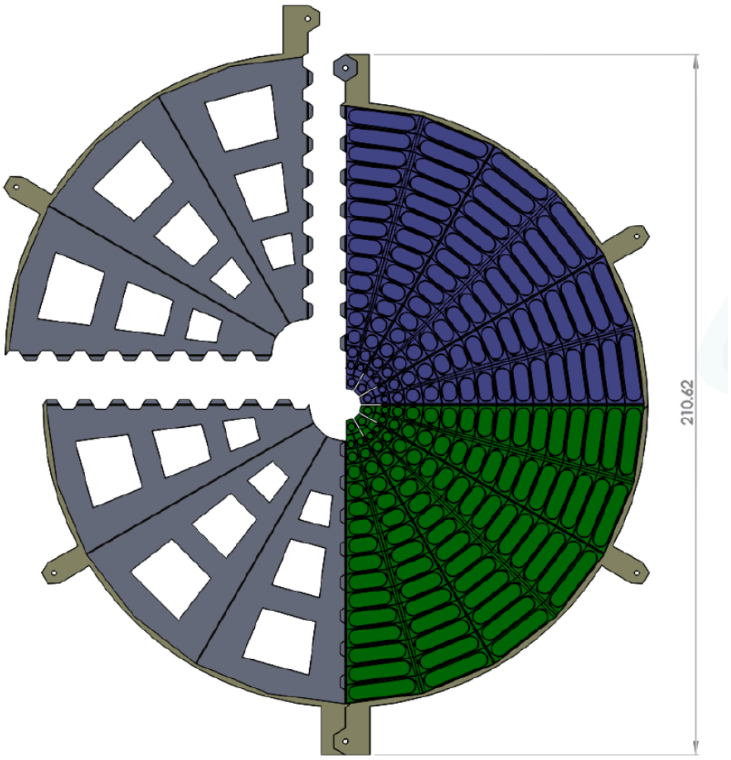

Figure 5.9: Schematic diagram of the mechanical support structure for mounting the EPD as viewed from the nominal collision point. Two quadrants are shown fully populated with three EPD supersectors each (green and blue). One quadrant (upper left) is shifted for clarification.

Chapter 6

Summary and Outlook

Fluctuations of conserved quantities, such as net-baryon (ΔN_B), net-charge (ΔN_Q) and net-strangeness (ΔN_S), have been predicted to be sensitive to the QCD phase transition and the QCD critical. The cumulants of the event-by-event distributions of these conserved quantities are directly connected to the thermodynamic susceptibilities computed with Lattice QCD and in the Hadron Resonance Gas (HRG) model. Thus, those cumulant ratios are equivalent to the ratios of various order susceptibilities as $C_4/C_2 = \chi_i^{(4)}/\chi_i^{(2)}$ and $C_3/C_2 = \chi_i^{(3)}/\chi_i^{(2)}$, where i indicates the conserved quantity. They are also related to different powers of the correlation length. In order to compare with theoretical calculations, cumulant ratios ($S\sigma = C_3/C_2$, $\kappa\sigma^2 = C_4/C_2$) are constructed to cancel the volume (VT^3) . Thus, those cumulant ratios are also directly related to the ratios of various order susceptibilities as $C_4/C_2 = \chi_i^{(4)}/\chi_i^{(2)}$ and $C_3/C_2 = \chi_i^{(3)}/\chi_i^{(2)}$, where i indicates the conserved quantity.

Experimentally, we use net-kaon (ΔN_K) as proxy for net-strangeness. In this thesis, we discuss the efficiency-corrected cumulants and cumulant ratios of the net-kaon (ΔN_K) multiplicity distributions measured in Au+Au collisions at $\sqrt{s_{\rm NN}}$ = 7.7, 11.5, 14.5, 19.6, 27, 39, 62.4, and 200 GeV collected in 2010, 2011, and 2014 by STAR at RHIC.

- STAR first measurement on collision energy and centrality dependence of net-Kaon cumulants and their ratios, within the kinematic range [$|y| < 0.5, 0.2 < p_T < 1.6$ (GeV/c))], for Au+Au collisions at $\sqrt{s_{NN}}$ = 7.7, 11.5, 14.5, 19.6, 27, 39, 62.4 and 200 GeV are presented.

- In general, the cumulants show a nearly linear variation with $\langle N_{part} \rangle$, which can be understood as the additivity property of the cumulants by increasing the volume of the system. This reflects that the cumulants are extensive

quantities that are proportional to system volume. The decrease in the C_1 and C_3 values with increasing collision energy indicates that K^+/K^1 approaches unity for the higher collision energies.

- The values of net-Kaon's $\kappa\sigma^2$ and $S\sigma$/Skellam are consistent with poisson and negative binomial distribution baseline within errors.

- Moments results from UrQMD (no Critical Point), shows no energy dependence for $S\sigma$/Skellam and $\kappa\sigma^2$.

To understand the non-critical contributions to the observables, we have performed detailed model calculations. In this analysis, we present the centrality and energy dependence of the cumulants (C_1, C_2, C_3, C_4) and their ratios $(C_3/C_2 = S\sigma, C_4/C_2 = \kappa\sigma^2)$ of net-proton, net-charge and net-kaon multiplicity distributions with UrQMD model for Au+Au collision at $\sqrt{s_{NN}}$=7.7, 11.5, 19.6, 27, 39, 62.4 and 200 GeV. The comparisons for the cumulant ratios ($S\sigma$, $\kappa\sigma^2$) of net-proton, net-charge and net-kaon multiplicity distributions has been made between the STAR data and the UrQMD calculations. Within the uncertainties, the net-charge and net-kaon fluctuations measured by STAR experiment can be described by the UrQMD results. For the net-proton fluctuations, the STAR measured $\kappa\sigma^2$ at the 0-5% most central Au+Au collisions show a clear non-monotonic energy dependence with a minimum around 20 GeV. Since the UrQMD model are blind to the critical phenomena in the heavy ion collision, the results from UrQMD calculations can provide us non-CP physics baselines and a qualitatively estimation for the background contributions to the QCD critical point search in heavy-ion collisions by using the fluctuations of the net-proton, net-charge and net-kaon numbers.

The upcoming RHIC BES II in 2019-2020, will include an upgraded STAR detector. An i(nner)TPC and Endcap TOF upgrade will enlarge the phase-space up to $|\eta|$ <1.5 and down to p_T = 60 MeV/c. The Event-Plane Detector at forward rapidities will allow for a better centrality estimation, suppressing auto-correlations. The figure 6.1 shows the error estimation at 19.6GeV for $\kappa\sigma^2$with the BESII detector upgrade. The error was estimated based on the Delta theorem. The x axis is the width of the acceptance window, the red markers represent the result from BES I, the blue bands represent the error estimation from BES II. We can clearly see that the statistic errors will be significantly improved with the detector upgrade in the same rapidity window.

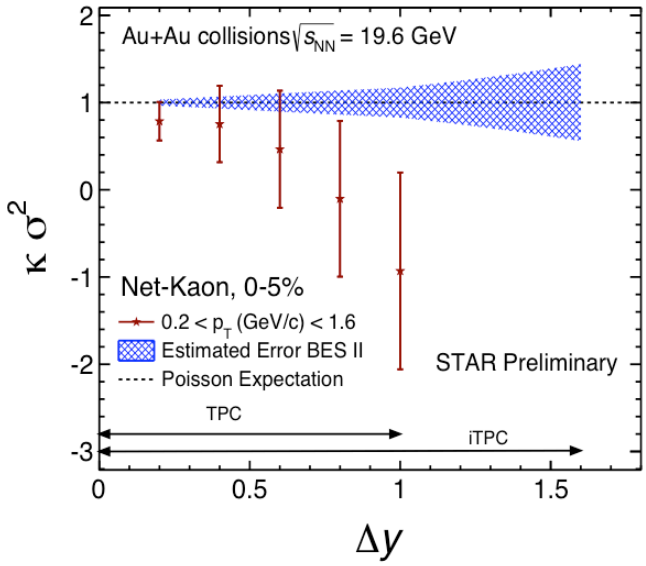

Figure 6.1: Error estimation (blue band) for net-kaon $\kappa\sigma^2$ in Au+Au collisions at $\sqrt{s_{NN}}$ = 7.7 GeV with the upgraded STAR detector and larger statistics in the upcoming RHIC Beam Energy Scan II for an increasing rapidity coverage.

Bibliography

[1] M. Gell-Mann, Acta Phys. Austriaca Suppl. **9**, 733 (1972).

[2] H. Fritzsch, M. Gell-Mann, and H. Leutwyler, Physics Letters B **47**, 365 (1973).

[3] R. P. Feynman, *QED The Strange Theory of Light and Matter (Princeton University, Princeton, 1985)* (S. Weinberg).

[4] J. D. Bjorken, Phys. Rev. D **27**, 140 (1983).

[5] J. Greensite, Lect. Notes Phys. **821**, 1 (2011).

[6] S. Bethke, Progress in Particle and Nuclear Physics **58**, 351 (2007).

[7] D. J. Gross and F. Wilczek, Phys. Rev. Lett. **30**, 1343 (1973).

[8] H. D. Politzer, Phys. Rev. Lett. **30**, 1346 (1973).

[9] N. Cabibbo and G. Parisi, Physics Letters B **59**, 67 (1975).

[10] R. D. Pisarski and F. Wilczek, Phys. Rev. D **29**, 338 (1984).

[11] M. P. Lombardo, XXIVth International Symposium on Lattice Field Theory , 140.1 (2006).

[12] M. Cheng, *et al.*, Phys. Rev. D **79**, 074505 (2009).

[13] R. V. Gavai and S. Gupta, Phys. Rev. D **78**, 114503 (2008).

[14] A. Hald, International Statistical Review **68**, 137 (2000).

[15] Y. Aoki, G. Endrődi, Z. Fodor, S. D. Katz, and K. K. Szabó, Nature **443**, 675 (2006).

[16] S. Gupta, X. Luo, B. Mohanty, H. G. Ritter, and N. Xu, Science **332**, 1525 (2011).

[17] E. S. Bowman and J. I. Kapusta, Phys. Rev. C **79**, 015202 (2009).

[18] S. Ejiri, Phys. Rev. D **78**, 074507 (2008).

[19] C. Athanasiou, K. Rajagopal, and M. Stephanov, Phys. Rev. D **82**, 074008 (2010).

[20] X. Luo, B. Mohanty, and N. Xu, Nuclear Physics A **931**, 808 (2014).

[21] P. K. Netrakanti, X. F. Luo, D. K. Mishra, B. Mohanty, A. Mohanty, and N. Xu, arXiv , arXiv:1405.4617 (2014), 1405.4617 .

[22] X. Luo and the STAR Collaboration, J. Phys.: Conf. Ser. **316**, 012003 (2011).

[23] J. Fu, Physics Letters B **722**, 144 (2013).

[24] P. Garg, D. K. Mishra, P. K. Netrakanti, B. Mohanty, A. K. Mohanty, B. K. Singh, and N. Xu, Physics Letters B **726**, 691 (2013).

[25] C. Herold, M. Nahrgang, Y. Yan, and C. Kobdaj, arXiv , 115106 (2014), 1407.8277 .

[26] K. Morita, B. Friman, and K. Redlich, Physics Letters B **741**, 178 (2015).

[27] P. Braun-Munzinger, B. Friman, F. Karsch, K. Redlich, and V. Skokov, Phys. Rev. C **84**, 064911 (2011).

[28] M. Sakaida, M. Asakawa, and M. Kitazawa, Phys. Rev. C **90**, 064911 (2014).

[29] P. Braun-Munzinger, B. Friman, F. Karsch, K. Redlich, and V. Skokov, Nuclear Physics A **880**, 48 (2012).

[30] M. A. Stephanov, Phys. Rev. Lett. **102**, 032301 (2009).

[31] M. Cheng, *et al.*, Phys. Rev. D **79**, 074505 (2009).

[32] S. Borsányi, G. Endrődi, Z. Fodor, and S. D. Katz, Journal of High Energy ... (2012).

[33] F. Karsch and K. Redlich, Physics Letters B **695**, 136 (2011).

[34] X. Luo, Nuclear Physics A **904-905**, 911c (2013).

[35] S. Collaboration and J. Adams, arXiv , 102 (2005), nucl-ex/0501009 .

[36] L. Adamczyk, *et al.*, Phys. Rev. Lett. **112**, 032302 (2014).

[37] J. Cleymans, H. Oeschler, K. Redlich, and S. Wheaton, Phys. Rev. C **73**, 034905 (2006).

[38] P. Alba, W. Alberico, R. Bellwied, M. Bluhm, V. Mantovani Sarti, M. Nahrgang, and C. Ratti, Physics Letters B **738**, 305 (2014).

[39] S. Borsányi, Z. Fodor, S. D. Katz, S. Krieg, C. Ratti, and K. K. Szabó, Phys. Rev. Lett. **113**, 052301 (2014).

[40] S. Borsányi, Z. Fodor, S. D. Katz, S. Krieg, C. Ratti, and K. K. Szabó, Phys. Rev. Lett. **111**, 062005 (2013).

[41] J. Noronha-Hostler, R. Bellwied, J. Gunther, P. Parotto, A. Pasztor, I. P. Vazquez, and C. Ratti, ... arXiv:160702527 (2016).

[42] L. Adamczyk, *et al.*, Phys. Rev. Lett. **113**, 092301 (2014).

[43] M. Harrison, T. Ludlam, and S. Ozaki, Nuclear Instruments and Methods in Physics Research Section A: Accelerators, Spectrometers, Detectors and Associated Equipment **499**, 235 (2003).

[44] H. Hahn, *et al.*, Nuclear Instruments and Methods in Physics Research Section A: Accelerators, Spectrometers, Detectors and Associated Equipment **499**, 245 (2003).

[45] M. A. Stephanov, Phys. Rev. Lett. **107**, 052301 (2011).

[46] L. Adamczyk, *et al.*, Phys. Rev. C **88**, 014902 (2013).

[47] M. Anderson, *et al.*, Nuclear Instruments and Methods in Physics Research Section A: Accelerators, Spectrometers, Detectors and Associated Equipment **499**, 659 (2003).

[48] H. Bichsel, Nuclear Instruments and Methods in Physics Research Section A: Accelerators, Spectrometers, Detectors and Associated Equipment **562**, 154 (2006).

[49] W. J. Llope, Nuclear Instruments and Methods in Physics Research Section B: Beam Interactions with Materials and Atoms **241**, 306 (2005).

[50] W. J. Llope, *et al.*, Nuclear Instruments and Methods in Physics Research Section A: Accelerators, Spectrometers, Detectors and Associated Equipment **522**, 252 (2004).

[51] P. Fachini and Z. Xu, *Proposal for a large area time of flight system for STAR* (STAR-TOF Collaboration available at http://wjllope. rice . . . , 2003).

[52] M. Bleicher, *et al.*, J. Phys. G: Nucl. Part. Phys. **25**, 1859 (1999).

[53] S. Bass, Progress in Particle and Nuclear Physics **41**, 255 (1998).

[54] J. Xu and (STAR Collaboration), J. Phys.: Conf. Ser. **779**, 012073 (2017).

[55] X. Luo, J. Phys. G: Nucl. Part. Phys. **39**, 025008 (2012).

[56] X. Luo, Phys. Rev. C **91**, 034907 (2015).

[57] X. Luo, J. Xu, B. Mohanty, and N. Xu, J. Phys. G: Nucl. Part. Phys. **40**, 105104 (2013).

[58] S. Collaboration, *et al.*, (2010), 1007.2613 .

[59] X. Luo, arXiv , arXiv:1503.02558 (2015), 1503.02558 .

[60] X. Luo, arXiv **A956**, 75 (2016).

[61] J. Thäder, arXiv , arXiv:1601.00951 (2016), 1601.00951 .

[62] B. Ling and M. A. Stephanov, Phys. Rev. C **93**, 034915 (2016).

[63] M. Kitazawa, Nuclear Physics A **942**, 65 (2015).

[64] C. Adler, A. Denisov, E. Garcia, M. Murray, H. Stroebele, and S. White, Nuclear Instruments and Methods in Physics Research Section A: Accelerators, Spectrometers, Detectors and Associated Equipment **470**, 488 (2001).

[65] C. A. Whitten, Polarized Ion Sources **980**, 390 (2008).

[66] K. H. Ackermann, *et al.*, arXiv **499**, 624 (2003).

[67] H. Bichsel, Nuclear Instruments and Methods in Physics Research Section A: Accelerators, Spectrometers, Detectors and Associated Equipment **562**, 154 (2006).

[68] M. L. Miller, K. Reygers, S. J. Sanders, and P. Steinberg, Annu. Rev. Nucl. Part. Sci. **57**, 205 (2007).

[69] A. Bzdak and V. Koch, Phys. Rev. C **91**, 027901 (2015).

[70] V. Skokov, B. Friman, and K. Redlich, Phys. Rev. C **88**, 034911 (2013).

[71] A. Bzdak and V. Koch, Phys. Rev. C **86**, 044904 (2012).

[72] T. J. Tarnowsky and G. D. Westfall, Physics Letters B **724**, 51 (2013).

[73] J. Xu, S. Yu, F. Liu, and X. Luo, Phys. Rev. C **94**, 024901 (2016).

[74] D. H. Rischke, S. Bernard, and J. A. Maruhn, Nuclear Physics A **595**, 346 (1995).

[75] J. Brachmann, S. Soff, A. Dumitru, H. Stöcker, J. A. Maruhn, W. Greiner, L. V. Bravina, and D. H. Rischke, Phys. Rev. C **61**, 024909 (2000).

[76] H. Stöcker, Nuclear Physics A **750**, 121 (2005).

[77] S. A. Bass, *et al.*, arXiv , 255 (1998), nucl-th/9803035 .

[78] J. Steinheimer, J. Auvinen, H. Petersen, M. Bleicher, and H. Stöcker, Phys. Rev. C **89**, 054913 (2014).

[79] V. P. Konchakovski, W. Cassing, Y. B. Ivanov, and V. D. Toneev, Phys. Rev. C **90**, 014903 (2014).

[80] L. Adamczyk and others, Phys. Rev. Lett. **112**, 162301 (2014).

[81] X. Luo, in *Proceedings of the 9th International Workshop on Critical Point and Onset of Deconfinement (CPOD2014). 17-21 November* (2014) p. 19.

[82] V. D. Kovaltchouk, G. J. Lolos, Z. Papandreou, and K. Wolbaum, Nuclear Instruments and Methods in Physics Research Section A: Accelerators, Spectrometers, Detectors and Associated Equipment **538**, 408 (2005).

[83] V. Balagura, M. Danilov, B. Dolgoshein, S. Klemin, R. Mizuk, P. Pakhlov, E. Popova, V. Rusinov, E. Tarkovsky, and I. Tikhomirov, Nuclear Instruments and Methods in Physics Research Section A: Accelerators, Spectrometers, Detectors and Associated Equipment **564**, 590 (2006).

[84] J. Anderson and For the CMS Hcal Collaboration), J. Phys.: Conf. Ser. **404**, 012019 (2012).

Acknowledgements

At the end of my thesis, I would like to thank many people who give help to my analysis. Without their supports, this valuable work will not be done so smoothly. Please allow me to take this opportunity to express my appreciation to all the people listed or might not listed in the following.

I would like to thank my supervisor, Professor Feng Liu, for introducing me into the heavy-ion physics field. It's such an amazing, fantastic, and cool field which I learn a lot of things from. I deeply appreciate his guiding in my study and offering me the opportunity to perform my research in the Lawrence Berkeley National Lab. I thank Dr. Nu Xu who provide me a very good environment for studying and an excellent group to work with, the RNC group at LBNL. His excellent knowledge on the physics inspire me a lot. I thank Dr. Nu Xu, Prof. Xiaofeng Luo, Dr. Jochen Thaeder, and Dr. Bedangadas Mohanty for their guiding and fruitful discussion on my moments analysis. Special thanks to Prof. Xiaofeng Luo who spent a lot of time teaching me almost everything about higher moments analysis. Without his help and support, this thesis would not happen. I thank Dr. Jochen Thaeder for so many useful discussions on the technique details.

I spend two years on my analysis at LBNL. I learnt a lot from the discussions with the RNC group members. Thanks to Dr. Xin Dong, Dr. Alex Schmah, Dr. Hao Qiu, Dr. Grazyna Odyniec, Dr. Mustafa Mustafa, Dr. Hans Georg Ritter for their help and suggestions during group meetings. Thanks to Guannan Xie, Long Ma, Jinlong Zhang, Peng Sun, Xun Sun, Xiaolong Chen for their help on my work and living. We have a lot of fun together and I would never foget the happy hours on the hot pot and traveling. Thanks to all the other RNC group members.

I would thank the STAR group at CCNU. Thanks to Dr, Kai Xiao, Dr. Lizhu Chen, Shushu Shi for their help at the very beginning stage of my research. Thank Biao Tu and Liang Zhang for their help during my stay at LBNL. Thanks all the other students and group members.

Finally, Thanks to my family's support and they always have faith on me. Their selfless love will encourage me keep forward.

Publications and Presentations

Papers

1. **Cumulants of net-proton, net-kaon, and net-charge multiplicity distributions in Au+Au collisions 7.7, 11.5, 19.6, 27, 39, 62.4, and 200 GeV with the UrQMD model.** **Ji Xu**, Shili Yu, Feng Liu, and Xiaofeng Luo, *Phys. Rev. C*, 94.024901 (2016)

2. **Volume fluctuation and auto-correlation effects in the moment analysis of net-proton multiplicity distributions in heavy-ion collisions.** Xiaofeng Luo, **Ji Xu**, Bedangadas Mohanty, Nu Xu, *J. Phys. G: Nucl. Part. Phys.* 40 (2013) 105104

3. **Collision Energy Dependence of Moments of Net-Kaon Multiplicity Distributions at RHIC** Primary authors: **Ji Xu**, Feng Liu, Xiaofeng Luo, Bedanga Mohanty, Jochen Thaeder, Nu Xu Target Journal: PLB (in preparation)

Conference Proceedings

1. **Energy Dependence of Moments of Net-Proton, Net-Kaon, and Net-Charge Multiplicity Distributions at STAR.** **Ji Xu**, *Journal of Physics: Conference Series* 736 (2016) 012002

2. **Higher Moments of Net-Kaon Multiplicity Distributions at STAR** **Ji Xu**, *Journal of Physics: Conference Series* 799 (2017) 012073

Selected Presentations

1. The XXV international conference on Ultrarelativistic Heavy-Ion Collisions
   Poster: *Energy Dependence of Moments of Net-Kaon Multiplicity Distributions at STAR*

2. The 32nd edition of the Winter Workshop 2016.
   Invited Talk: *Energy Dependence of Moments of Net-Proton, Net-Kaon and Net-Charge Multiplicity Distributions at STAR*

3. 2016 RHIC and AGS Annual Users' Meeting.
   Invited Talk: *Fluctuations and Correlations at the RHIC BES*

4. The 16th International Conference on Strangeness in Quark Matter.
   Parallel Talk: *Higher Moments of Net-Kaon Multiplicity Distributions at STAR*